UNIVERSITY OF CALIFORNIA, MERCED

Exciton Dynamics in II-VI Semiconductor Nanoparticles

by

David P Morgan

A dissertation submitted in partial satisfaction of the
requirements for the degree
Doctor of Philosophy

in

Chemistry and Chemical Biology

In the

Graduate Division

Of the

University of California, Merced

Professor Anne M. Kelley, Chair
Professor David F. Kelley, Advisor
Professor Erik Menke
Professor Michael Scheibner

2019

The dissertation of David P Morgan, titled *Exciton Dynamics in II-VI Semiconductor Nanoparticles*, is hereby approved, and is acceptable in both quality and form for publication on microfilm and electronically.

_____ Date _____
David F. Kelley (advisor)

_____ Date _____
Hrant P. Hratchian

_____ Date _____
Michael Scheibner

_____ Date _____
Anne M. Kelley (chair)

University of California, Merced

Table of Contents

List of Figures

List of Tables

Acknowledgements

Thanks to Professor Dave Kelley for guidance, training, financial support, countless hours of fruitful discussions, and for setting the bar almost unreachably high in seemingly everything that he does. It should be noted that the majority of the new insights and ideas contained in Chapters 3 – 8 in this dissertation were his.

Thanks to Professors Anne Kelley, Hrant Hratchian, and Michael Scheibner for sitting on my PhD advisory committee, for job leads, and for all guidance provided.

Thanks to Dr Gary Beane, Dr Youhong Zheng, Dr Ke Gong, Jamie Grenland, Daniel Neff, Cassandra Nanney, Dr Adam Kell, Dr Rui Tan, Michael Lara & Steven Montoya for comradery, morale, and entertainment.

Curriculum Vitae

Education

PhD: Physical Chemistry
University of California, Merced — *2015 – present*
Thesis: *Exciton Dynamics in II-VI Semiconductor Nanoparticles*
Expected graduation date: August 2019

B.S: University of California, Berkeley — *2009 – 2012*

Professional & Academic Experience

Research Assistant: Quantum dot photophysics — *2015 – present*
University of California, Merced
Advisor: Professor David F Kelley

Teaching Assistant: Chemistry — *2015 – 2017*
University of California, Merced

Production Lead — *2013 – 2015*
EV Container
Supervisor: Dan Morgan

Research Assistant: Analytical atmospheric chemistry — *2011*
University of California, Berkeley
Advisor: Professor Robert Rhew

Research Assistant: Bacterial RNA expression — *2010*
University of California, Berkeley
Advisor: Professor Steve Lindow

Skills & Training

Semiconductor nanoparticle synthesis, purification, and post-synthetic modification
Transient absorption spectroscopy
Time-correlated single photon counting
UV-vis spectroscopy
Photoluminescence spectroscopy
FTIR spectroscopy
ATR spectroscopy
Transmission electron microscopy
Glovebox operation and maintenance
Schlenk line synthesis, operation and maintenance
Air-sensitive technique
Development and troubleshooting of manufacturing equipment and methodology
Ti:sapphire laser operation and maintenance
Home-built spectroscopy setups
Quantum mechanical calculations of semiconductor properties

Publications

Morgan, D. P.; Kelley, D. F. Exciton Localization and Radiative Lifetimes in CdSe Nanoplatelets. *J. Phys. Chem. C.* **2019 in press**

Morgan, D. P.; Kelley, D. F. Mechanism of Hole Trap Passivation In CdSe Quantum Dots by Alkylamines. *J. Phys. Chem. C.* **2018** , *122*, 25661-25667.

Morgan, D. P.; Maddux, C. J. A.; Kelley, D. F. Transient Absorption Spectroscopy of CdSe Nanoplatelets. *J. Phys. Chem. C*. **2018** , *122*, 23772−23779.

Morgan, D.; Kelley, D. F. Spectroscopy of Surface State p-Doped CdSe/CdS Quantum Dots. *J. Phys. Chem. Lett*. **2018** , *9*, 4160−4165.

Morgan, D.; Kelley, D. F. Role of Surface States in Silver-Doped CdSe and CdSe/CdS Quantum Dots. *J. Phys. Chem. C*. **2018** , *122*, 10627−10636.

Morgan, D.; Gong, K.; Kelley, A. M.; Kelley, D. F. Biexciton Dynamics in Alloy Quantum Dots. *J. Phys. Chem. C*, **2017** , *121(33)* 18307-18316.

Abstract of Dissertation

Title: Exciton Dynamics in II-VI Semiconductor Nanoparticles

Name: David P. Morgan

Degree: Doctor of Philosophy

Institution: University of California, Merced

Committee Chair: Anne M. Kelley

Colloidal II-VI quantum dots (QD) possess tunable optoelectronic properties that make them well-suited in applications as luminescent materials. However, their performance is often limited by nonradiative exciton quenching processes typically involving interaction of the exciton with surface states, crystalline defects, or other charge carriers. It is the purpose of this dissertation to identify and understand these decay mechanisms at a fundamental level. Two of the dominant processes, Auger recombination (AR) and hole trapping (HT), are explored from several angles. Biexciton lifetimes of alloyed $Cd_{1-x}Zn_xSe$ go through a minimum at small mole fractions of Cd (x = 0.1 – 0.4), and this behavior is attributed to partial hole localization in Cd-rich regions of the particle. For small x, the biexciton times are nonexponential, whereas the pure materials and alloys with $x \geq \sim 0.5$ show single exponential decays. A model of the alloy valence band potential is used to approximate hole density gradients (taken to be proportional to AR rates) for different alloy compositions, and the model reproduces both the faster and broader distribution of rates in the small Cd concentration regime.

The positive trion excitonic state is selectively prepared in CdSe and CdSeCdS core/shell particles by manipulating the surface chemistry. Comparison of the TA and PL decays shows that the trion lowest exciton bleach magnitude is ~ 1.5x greater than the exciton on account of the differences in fine structure. Stimulated emission is increased because all of the trion fine structure levels have fully allowed transitions to the ground state, while the trion excited state absorbance is weaker since the additional hole decreases the degeneracy of the transitions between the first and second multiexciton states, i.e. valence band state filling. Trion PL is blueshifted ~ 6 nm from the excitonic PL in the core/shells and ~ 0 - 1 nm in the cores, closely matching the sum of the additional e-h stabilization and h-h repulsion terms calculated in the effective mass approximation using first-order perturbation theory.

The effects of Ag doping on the photophysical properties of CdSe and CdSe/CdS quantum dots (QDs) are studied in terms of surface composition. TBP-ligated samples that suffer from hole trapping show a rise then fall of PLQY with increasing $[Ag^+]$, while higher QY particles passivated with TBP and amine or a thin CdS shell decrease upon doping. The initial increase is assigned to the passivation of pre-existing surface hole traps by interaction of interstitial Ag^+ with surface Se^{2-} ions, while the subsequent

decrease is due to the introduction of substitutional Ag^+, which act as a new source of hole traps. Well-passivated samples don't have high energy filled surface states, so the dopants remain in the +1 oxidation state, act only as hole traps, and lower QYs. Both CdSe and CdSeCdS particles ligated with amine but no phosphine have Fermi levels within kT of the VB, giving rise to the positive trion through thermal population of surface states. In this case, some fraction of the Ag^+ is reduced to Ag by the amine, which then shuts off trion Auger recombination by interacting with empty Se(0) orbitals.

Ligation of CdSe QDs with alkylamines raises QYs by decreasing the extent of hole trapping. This cannot be explained by a simple MO theory type interaction between the filled Se^{2-} and the N lone pair of the amine, so a new passivation mechanism is proposed that considers the electrostatics of L-type ligand binding. Electron donation by the amine creates a surface dipole layer that raises the VB and CB levels of the particle having little effect on the surface state energetics, thereby lowering $-\Delta G$ for hole trapping. The mechanism is corroborated with the observed increase in CB electron transfer rates to methylviologen and decreased hole transfer rates to 4-methylbenzenethiol upon treatment with the amine.

Transient absorption (TA) spectra of CdSe nanoplatelets (NPL) are analyzed in terms of the exciton fine structure and population of low-lying lateral excited states. Treatment with an external hole trap decreases the NPL HH bleach, while the analogous spherical particles show no spectral manifestations of hole trapping in TA measurements. The differences are attributed to the strong z-quantum confinement breaking the LH/HH degeneracy as well to the reduced e-h exchange interaction in NPL. Because the $X \rightarrow XX$ triplet-triplet transition proceeds from the LH and is forbidden in the HH band, splitting off the LH results in reduced PA and increased bleach of the NPL lowest exciton band. The weak e-h exchange interaction allows significant population of the bright state and hence more stimulated emission in NPL compared with QD.

The relative bleach magnitudes of the same 4.5 ML nanoplatelets are measured by transient absorption spectroscopy and are found to be much less than those of their spherical counterparts. Analysis of the relative bleach magnitudes (change in optical density at the HH exciton normalized to the absorbance) shows that absorption of a photon bleaches ~ 10-25 % of the GSA, with the relative bleach getting smaller with increasing platelet lateral dimensions. This suggests that the size of the exciton is smaller than the platelet and is independent of the platelet areas. This is an unsurprising result given that the bulk Bohr radii of CdSe excitons is about 5 nm , that the NPL Bohr radii should be significantly less than those seen in bulk due to the nearby layer of organic, low dielectric constant material, and because the platelet dimensions are greater than the Bohr radii. So the lack of significant quantum confinement along x and y causes the excitonic areas to be platelet-size independent. This consideration is taken into account when explaining the reported size independence of the radiative lifetime, which we measure to be about 5 ns for lateral areas between 85 and 320 nm^2. Taking into account the singlet-triplet splitting, the less than unity e-h overlap integral, and the fraction of the platelet area occupied by an exciton allows near-quantitative reproduction of the radiative lifetimes using the integrated extinction coefficients as in the Einstein A&B coefficient treatment of radiative rates.

Ch 1

Introduction

The utility of any optical material depends critically on one central question – what is the fate of the electronic excited state? II-VI semiconductor nanoparticles (quantum dots, or QD) are particularly desirable optical materials because of their large absorption cross-sections, narrow emission linewidths, color tunability, and high photoluminescence quantum yields (PLQY), and to exert any control over these properties entails developing a deep understanding of the photophysics and quantum mechanics governing the material's behavior. As a photoluminescent material, the basic mechanism of operation is that a nanocrystal absorbs a photon, stores the energy for a period of time, then reemits a photon. Depending on the material, the probability of emitting a photon varies considerably, and in order to maximize this probability (the PLQY), the first task is to discover what happens after a QD absorbs light. Many considerations underlie this basic question. For example, to determine the fate of an electronically excited QD, one must start with an accurate description of the electronic excited state. To develop strategies for using organic ligands to electronically passivate the nanocrystal surface and raise PLQYs, one must start with an accurate picture of the QD-ligand interaction. It is apparent from an overview of the scientific literature that many of these systems have yet to be adequately described. Therefore, it is the purpose of this work to take as many steps back as possible and provide the fundamental descriptions of various phenomena relating to electronically excited nanoparticles that are consistent with our own experimental observations as well as those supplied by the scientific community.

Nanoparticles have been made, albeit unknowingly, since as early as the 4th century AD. A Roman artifact called the Lycurgus Cup has been reported to derive its unique optical properties from gold and silver nanoparticles being embedded in the dichroic glass. Techniques for dissolving and precipitating precious metals have been known since early times, and this is most likely the method used to create the materials in the glass.[1] The basic techniques for colloidal synthesis of nanoparticles remain largely unchanged. Nanoparticles can be formed via a variety of arrested precipitation methods, where micro- to millimolar concentrations of dissolved metal salts are precipitated either with a reducing agent (in the case of fully metallic particles) or with a nonmetal (in the case of binary semiconductor particles), and the reaction is quenched before the nanoparticles aggregate into macroscopic chunks of material. This is typically achieved through a combination of reducing the reaction temperature, keeping the precursor concentrations small enough that secondary nucleation and growth is suppressed by a lack of reagents, and through the use of a surfactant to bind the surface and prevent the approach and further reaction of precursors. This is known as a 'bottom-up' approach, where nanomaterials are made from dissolved starting materials. 'Top-down' methods also exist, where bulk materials are broken down or miniaturized while retaining their original crystal structure. Bottom up methods typically yield superior materials since they allow better control over sample homogeneity and crystallinity.[2]

More recently, interest in semiconductor nanoparticles took off in the 1980's. A few seminal pieces of work [3,4] characterized the unique optical properties of QD's and called the community to develop better synthetic techniques to produce higher quality, more monodispersed syntheses. Until that point, understanding of QDs had been stunted by the inability to produce samples of high PL quantum yield and small size

polydispersity. Even with the advent of better techniques, characterization is still hindered by inhomogeneities in the surface structure.

Furthermore, typical scattering techniques for obtaining surface structures rely on the long-range order of bulk crystals and surfaces, so these characterization methods don't yield much information because the particles orient randomly in space relative to their crystallographic axes. Typical growth techniques yield particles of varying sizes, with different sizes of individual surface facets, and with differing degrees of ligation based on the size and microscopic structure of individual facets. Because of the dearth of experimental techniques capable of tackling this problem, many authors try to theoretically characterize the surface structure and energetics [5,6,7]. A few authors have circumvented the issue of polydispersity by developing synthetic techniques for making 'magic-sized clusters' (MSC), or particles that are chemically unique and 100% monodispersed, but the range of available sizes is quite small, so color tunability of the emission and other size-dependent properties of typical QD samples are not available with the better-characterized MSC.[8,9]

The challenges associated with sample inhomogeneity bear directly on the conclusions drawn here. In this collection of studies, insight into the photophysics and quantum mechanical descriptions of various QDs are derived from their radiative kinetics, and the presence of QDs having slightly differing structures makes analysis of the kinetics difficult. The most commonly encountered situation is that some QDs have a crystalline defect or surface trap while others don't, and that the number and/or depths of the traps, and therefore the trapping rates, varies from one particle to the next. [5,6,7] This manifests as nonexponential decays in the PL and transient absorption (TA) kinetics, and the kinetics are therefore typically modeled as multiexponential decays. Any analysis of the radiative kinetics must therefore be corroborated with multiple types measurements. For example, if a multiexponential fit to a PL decay gives two different components, one assigned to a carrier trapping process and the other to radiation, the assigned rates must be consistent with the PLQY measured by comparison of the static PL spectrum with a dye standard of known PLQY. Ambiguities exist even when going through this procedure. For example, an ensemble PLQY of 50% will be observed when 50% of the particles undergo only radiation while the other 50% trap on a timescale that is fast compared to radiation. If trapping rates are much faster than the instrumental resolution, this situation results in single exponential decay kinetics characteristic of a high-quality, highly luminescent sample. Another commonly encountered situation is that trapping rates are slower and none of the decay components reflect the actual radiative lifetime. In this case, it's easier to assign radiative lifetimes by comparison of the static and time-resolved PL. However, multiexponential fits tend not to be unique, so often times a radiative lifetime can be assigned only in samples with a high (> 50%) PLQY. The primary challenge, therefore, is making high quality samples. Until the procedure for making highly luminescent QDs is developed, little can be learned about their radiative kinetics. These considerations outline a general strategy for studying QD photophysics. It is of paramount importance to begin with a highly luminescent sample that is as well-\characterized as possible. Since the thrust of our research group is kinetics rather than

synthesis and characterization, we rely heavily on synthetic procedures published by groups that are geared toward QD synthesis. [10-14]

The work presented here is expected to have a significant impact on the nanoparticle community. Over the last few years, we have identified several gaps in the community's understanding of QD photophysics. A common theme underlies each of these topics explored here; each study identifies or presents a new way of thinking about a particular nonradiative decay channel. Understanding the processes that quench QD photoluminescence is of critical importance for the development of highly luminescent optical materials. Similar studies found in the literature typically present a practical approach toward eliminating nonradiative decay channels in order to create high PLQY particles, while failing to adequately explain or characterize the nature of the nonradiative process that is being shut off. While this approach has yielded practical results, it has its limitations. A passivation strategy such as introducing an organic ligand into the reaction mixture may work quite well for a particular type of QD or under a specific set of conditions. But employing the same ligand under different conditions or with a different type of QD often produces entirely different results. Without a deeper understanding of the ligand-QD interaction, or whatever the system at hand may be, even the best minds are relegated to an empirical, guess-and-check type of approach. Dissatisfaction over this state of affairs is one of the primary motivations of this work, and the insights contained herein should inform future endeavors to create highly luminescent optical materials by rational design.

The dissertation will be organized as follows: The first section provides theoretical background underlying the photophysical phenomena explored in the individual studies; the fundamentals of light absorption and radiation, Auger recombination, charge transfer and carrier trapping, and CdSe angular momentum fine structure are discussed in detail. Following that is a section that describes both the experimental and theoretical aspects of transient absorption (TA) spectroscopy. The body will be broken into chapters based on papers that have been published during the course of this work. It will contain a chapter on each of the following topics: the effects of alloying on Auger dynamics, the effects of silver doping on carrier trapping, the spectroscopic identification of the positive trion, the mechanism by which alkylamines raise the PLQY of CdSe QD, and the spectroscopic manifestations of hole trapping in CdSe nanoparticles and how they change based on the particle morphology. The conclusion will summarize the work that was done and distill some of the key physical insights that were derived from the results.

Ch 1 References

1. Wikipedia. Lycurgus Cup. https://en.wikipedia.org/wiki/Lycurgus_Cup (accessed Jan 1, 2019).
2. Kuno, M. Introductory Nanoscience. Garland Science, Taylor & Francis Group: New York, 2012.
3. Brus, L. Electron-electron and electron-hole interactions in small semiconductor crystallites: The size dependence of the lowest excited electronic state. *J. Chem. Phys*. **1984,** 80, 4403-4409.
4. Brus, L. Electronic Wave Functions in Semiconductor Clusters: Experiment and Theory. *J. Phys. Chem*. **1986,** 90, 2555-2560.
5. Houtepen, A. J.; Hens, Z.; Owen, J. S.; Infante, I. On the Origin of Surface Traps in Colloidal II-VI Semiconductor Nanocrystals. *Chem. Mater*. **2017**, 29, 752−761.
6. Giansante, C.; Infante, I. Surface Traps in Colloidal Quantum Dots: A Combined Experimental and Theoretical Perspective. *J. Phys. Chem. Lett.* **2017,** 8, 5209-5215.
7. Boles, M.; Ling, D.; Hyeon, T.; Talapin, D. The surface science of nanocrystals. *Nature Materials*. **2016**, 15, 141−153.
8. Soloviev, V. N.; Eichhofer, A.; Fenske, D.; Banin, U. Size-Dependent Optical Spectroscopy of a Homologous Series of CdSe Cluster Molecules. *J. Am. Chem. Soc.* **2001**, *123*, 2354–2364.
9. Kasuya, A.; Sivamohan, R.; Barnakov, Y. A.; Dmitruk, I. M.; Nirasawa, T.; Romanyuk, V. R.; Kumar, V.; Mamykin, S. V.; Tohji, K.; Jeyadevan, B.; Shinoda, K.; Kudo, T.; Terasaki, O.; Liu, Z.; Belosludov, R. V.; Sundararajan, V.; Kawazoe, Y. Ultra-stable Nanoparticles of CdSe Revealed from Mass Spectrometry. *Nat. Mater*. **2004**, *3*, 99–102.
10. Pu, C.; Zhou, J.; Lai, R.; Niu, Y.; Nan, W.; Peng, X. Highly Reactive, Flexible Yet Green Se Precursor for Metal Selenide Nanocrystals: Se-Octadecene Suspension (Se-SUS). *Nano Res.* **2013**, *6*, 652−670.
11. Jasieniak, J.; Mulvaney, P. From Cd-Rich to Se-Rich – the Manipulation of CdSe Nanocrystal Surface Stoichiometry. *J. Am. Chem. Soc*. **2007**, *129*, 2841−2848.
12. Nan, W.; Niu, Y.; Qin, H.; Cui, F.; Yang, Y.; Lai, R.; Lin, W.; Peng, X. Crystal Structure Control of Zinc-Blende CdSe/CdS Core/Shell Nanocrystals: Synthesis and Structure-Dependent Optical Properties. *J. Am. Chem. Soc*. **2012**, *134*, 19685−19693
13. Groeneveld, E.; Witteman, L.; Lefferts, M.; Ke, X.; Bals, S.; Van Tendeloo, G.; de Mello Donega, C. Tailoring ZnSe-CdSe Colloidal Quantum Dots via Cation Exchange: From Core/Shell to Alloy Nanocrystals. *ACS Nano.* **2013**, *7*, 7913−7930.
14. Ithurria, S.; Dubertret, B. Quasi 2D Colloidal CdSe Platelets with Thicknesses Controlled at the Atomic Level. *J. Am. Chem. Soc*. **2008**, *130*, 16504.

Ch 2

Theoretical Background

The dissertation presented here draws heavily on concepts from quantum mechanics, solid-state physics, semiconductor band structure, and spectroscopy. Although the individual studies cover a range of material systems and topics in NP photophysics, a handful of themes emerge and are central to understanding the materials' behavior. This section provides a brief theoretical treatment of a few of the most important topics, including time-dependent perturbation theory and the Einstein A & B coefficient treatment of radiative rates, Auger recombination dynamics, Marcus Theory and charge transfer kinetics, and the angular momentum fine structure in quantum-confined excitons in CdSe. This is followed by a treatment of the experimental and theoretical aspects of transient absorption spectroscopy. Comprehensive reviews of these topics can be found elsewhere; the purpose of this section is to provide only the basic conceptual framework for tackling the individual studies of nanoparticle spectroscopy and dynamics found herein.

2.1 Absorption and Emission of Radiation

The performance of semiconductor nanoparticles as optical materials depends on how well they absorb and emit light. Specifically, large absorption cross-sections (ε) and fast radiative rates (k_r) are desirable since they allow radiation to outcompete other processes that quench photoluminescence. Theoretical modeling and measurement of photoluminescence decay rates is therefore an important task if one is to develop SCNP as an optical material. This section addresses some of the theory of light absorption and emission as well as the experimental procedure used throughout this piece of work to measure PL decay rates.

The interaction of matter with an oscillating electromagnetic field can be modeled as a time-dependent perturbation, provided that the incident field is small compared with the field due to the interaction between electrons and nuclei. In the presence of the perturbing field, the wavefunction satisfies the time-dependent Schrodinger equation E2.1.

$$-\frac{h}{2\pi i}\frac{\partial \Psi}{\partial t} = (H^0 + H')\Psi \qquad \text{E2.1}$$

Where H^0 is the unperturbed Hamiltonian and H' is represents the time-dependent potential associated with the radiation-matter interaction. Because H^0 is a Hermitian operator and its eigenfunctions form a complete set, the solutions to the time-dependent Schrodinger can be expanded as a linear combination of these eigenfunctions. The expansion coefficients can be approximated by substituting the expanded form of Ψ back into E2.1, multiplying by an arbitrary eigenfunction of H^0 and making use of the orthonormality relation, then imposing the initial condition that at time t = 0, before the perturbation is present, the entire population is in one eigenstate, then integrating over time. The solution for the coefficients is then given by E2.2.

$$c_m(t') = -\frac{2\pi i}{h} \int_0^{t'} e^{-i(\omega_m - \omega_n)t} \langle \Psi_m | H' | \Psi_n \rangle \, dt \qquad \text{E2.2}$$

The probability of transitioning from the stationary state *n* to state *m* after exposure to a perturbation of duration t' is then $|c_m(t')|^2$. Taking the classical description of an electromagnetic field, H' is given by a spatial term (E_0qx) multiplied by a time-varying oscillatory term sin(ωt), where E_0 is the amplitude of the electric field, q is the charge of a particle perturbed the field, and ω is the angular frequency of the perturbing field. The eigenfunctions are factored into the spatial and time-dependent parts, giving the expression for the coefficients $c_m(t')$ as

$$c_m(t') = \frac{E_0\pi}{hi} \mu_{mn} \left(\frac{e^{i(\omega mn+\omega)t'-1}}{\omega_{mn}+\omega} - \frac{e^{i(\omega mn-\omega)t'-1}}{\omega_{mn}-\omega} \right) \qquad \text{E2.3}$$

Where μ_{mn} is the transition dipole moment $\langle \Psi_m{}^0 | qx | \Psi_n{}^0 \rangle$. During absorption, the absorbing species goes from a lower energy state to a higher energy state and the second term in parentheses dominate. The first term is significant in the reverse case when ω_{mn} is negative, as in the case of stimulated emission.[1]

Equation 2.3 shows that the likelihood (or cross-section) for absorption is the same as that for stimulated emission, but it falls short insofar as it doesn't predict spontaneous emission. Because energy is conserved during the transition, it follows that the physical processes are reversible.[2] Specifically, if absorption of a photon causes a transition from a lower energy state |*n* > to a higher state |*m* >, then the decay of a system from |*m* > to |*n* > will be accompanied by the emission of a photon. It is intuitive that the magnitude of the coupling between two states by a radiation field doesn't depend on which we assign as the initial and final states. This conclusion naturally falls out of the Einstein A & B coefficient treatment of the radiative rate, which yields the expression E2.4 relating radiative rates to the transition dipole moment.[3]

$$k_r = \frac{n\omega^3|\mu|^2}{3\pi\varepsilon_0\hbar c^3} \qquad \text{E2.4}$$

The rate can also be expressed in terms of the integrated cross section of the emissive transition, as shown in E2.5.

$$k_r = \frac{n^2\omega^3}{\pi^2 c^2} \int d\omega \frac{\sigma(\omega)}{\omega} \qquad \text{E2.5}$$

E2.4 and 2.5 are valid for two-level systems where absorption and emission occurs between the same two states. When the degeneracies of the upper and lower states differ from one another, the rates of absorption vs stimulated emission scale like the ratio of the degeneracies. In the case of CdSe QDs, the $1S_{3/2,h}$-$1S_e$ transition consists of a manifold of angular momentum fine structure levels that are not spectrally resolved because of the large inhomogeneous broadening associated with particle size distributions characteristic of QD samples. The light hole (LH) states carry the majority of the oscillator strength and exist about 40-50 meV higher in energy than the heavy hole (HH)

levels,[4] whereas a typical value for the inhomogeneous broadening is ~ 100 meV. The consequences of this is that both the HH and LH states contribute to the absorption, but emission occurs primarily from the HH levels, since only these states are significantly populated after thermal equilibration at room temperature.[4,5,6] The HH levels are further split into the J = ± 2 and ± 1 levels, with J being the projection of the total angular momentum onto the z axis. The only electronic configuration with J = 2 has both spins aligned, so this state is a pure triplet, is the lowest energy angular momentum state, and transitions between this level and the ground state are spin-forbidden. The splitting between the two lowest energy dark and bright states is determined by the exchange interaction, which drops off with increasing particle size. The magnitude of the exchange interaction is about 20-25 meV for typical-sized particles,[7,8,9] leading to roughly 75/25% occupation of the dark/bright states. Because all of the absorption occurs via the bright states, while the majority of the excitonic population, after thermal equilibration, resides in an optically dark state, the radiative lifetime is much longer than one would expect based on the values of the integrated extinction coefficients. The angular momentum fine structure will be covered in greater detail in Ch 2.4.

2.2 Auger Recombination

\

When three or more charge carriers are in close proximity to each other, two of the carriers can annihilate and transfer the excess kinetic energy to the third. This is known as Auger recombination. Auger recombination is commonly encountered in the context of elemental analysis through photoelectron spectroscopy. High energy UV or x-ray radiation is used to eject core electrons from individual atoms, leaving behind a vacancy at high potential. Higher lying electrons can then collapse into the vacant energy level and transfer the kinetic energy to an outer shell electron, and the transition typically supplies enough excess kinetic energy to eject the outer shell electron (the Auger electron). The kinetic energies of the Auger electrons are characteristic of individual atoms in the material, making Auger electron spectroscopy an ideal technique for spatially resolved surface-specific elemental analysis.[10]

A similar situation is encountered in SCNP. Absorption of a photon creates an electron-hole pair that can recombine and transfer the energy to a third charge carrier. This requires that a third carrier be present and that the three are significantly Coulomb coupled In contrast with the atomic case using high-energy excitation, there isn't enough kinetic energy to eject an electron to vacuum, so a bound electron or hole state must exist at an energy E_{bg} above the band edge into which the receiving charge carrier can be excited.[11] The Auger recombination process is illustrated in Figure 2.1.

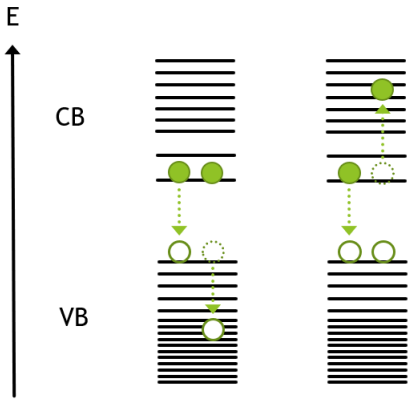

Figure 2.1 CdSe QD energy level diagram and the two Auger recombination pathways available for a biexciton. The diagram on the left (right) has the hole (electron) as the receiving carrier. Two degenerate pathways exist for both e and h excitation.

As with any electrodynamic process, the Auger rate can be calculated using Fermi's Golden Rule [12] as shown below in equation E2.6, where *i* is the initial electronic state, *f* is the final state, C is the Coulomb operator, $\rho(E_f)$ is the density of states at the final state, E_g is the band gap energy, and the delta function comes about from the requirement that energy be conserved during the transition.

$$k_{Auger} = \frac{1}{h} |\langle i \mid \hat{C} \mid f \rangle|^2 \rho(E_f) \delta(E_f - E_i + E_g) \qquad \text{E2.6}$$

In CdSe nanoparticles, the Auger pathway involving excitation of the hole is the dominant process. This can be understood in terms of the difference in rates, specifically because the density of states in the valence band is greater than in the conduction band. This results from the larger effective mass of the hole. The effective mass appears in the denominator of the particle-in-a-sphere energies,[13] hence the larger effective mass of the hole results in a denser manifold of hole states compared with the electron.

Another important consideration in understanding Auger rates is the momentum-forbidden nature of the transitions in bulk and its relaxation due to quantum confinement. In zincblende crystals, the lowest energy VB and CB states are both at the Γ point (k = 0) of the Brillouin zone,[14] while the final receiving state is at a higher energy but within the same band (k > 0). The nonzero change in momentum limits Auger recombination rates since the transition typically must be accompanied by the emission of several phonons, which in turn gives a small Franck-Condon factor in the integral over the vibrational wavefunctions. A cartoon of the states involved and the associated band diagrams is shown in Figure 2.2.

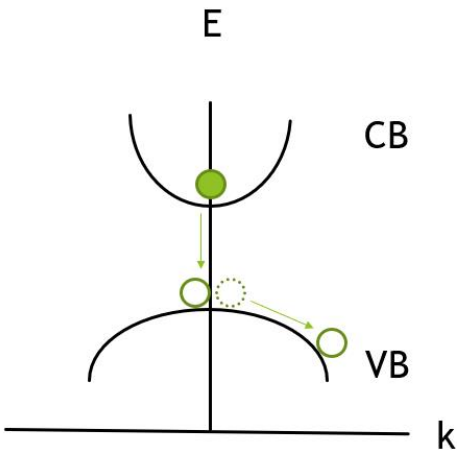

Figure 2.2 Auger recombination in the effective mass approximation showing the initial and final momentum states.

The band edge states are strictly at k = 0 only in the case of infinitely delocalized wavefunctions. An excitonic wavefunction localized to the volume of a nanoparticle is formulated by superimposing a number of k states of differing momenta. More localized wavefunctions have a greater contribution from higher momentum states. Localization therefore leads to greater Auger coupling between the initial and final momentum states, which, together with the reduced Coulomb interaction, explains the observed decrease in Auger rates with increasing particle size.[11]

Estimation of the Auger rates in CdSe nanoparticles is made difficult by the existence of nodes in the momentum wavefunction near the k values associated with the final particle-in-a-sphere states in the transition, which leads to non-physical singularities in the spectrum of rates vs particle size.[15,16] An estimation will be made here by choosing particle sizes that avoid this issue. Using the effective mass approximation expression given in E2.7, the value of k at the band gap energy (k_{bg}) for a 2.5 nm diameter particle is estimated at 5.26 nm^{-}, and k(E_g) for a 3.5 nm particle is 5.02 nm^{-1}.

$$k_{bg} = \sqrt{\frac{8\pi\, m_{eff} E_g}{h^2}} \qquad \text{E2.7}$$

The initial envelope hole wavefunctions are taken as the lowest order spherical Bessel functions [13] and are then Fourier transformed into momentum space, and the momentum wavefunctions are evaluated at the momentum of the final state calculated above. Since the rates are proportional to both the Coulomb coupling (C) and the square of the initial and final wavefunction overlaps in momentum space, we'll estimate the ratio of rates in the 2.5 and 3.5 nm particles as the ratio of the products of these two factors: $(\Psi(k_{bg})_{2.5}C_{2.5} / \Psi(k_{bg})_{3.5}C_{3.5})^2 = 2.2$. This approximation assumes that the final state wavefunction and density of states are the same for the two particle diameters, and that the amount of valence and conduction band mixing is independent of the particle diameter. The measured times are 20 and 48 ps, respectively, as shown in Figure 2.3. This gives a ratio of 2.4, indicating that, in this size regime, this is a very good approximation. Note that the

measured biexciton times are linear in volume, leading to the commonly observed 'volume scaling' of Auger rates.[12]

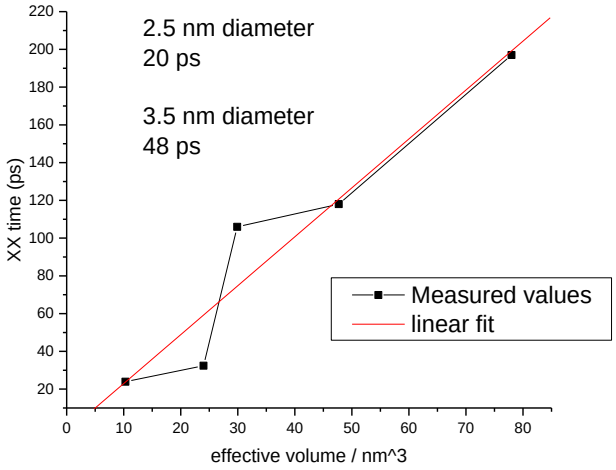

Figure 2.3 Biexciton decay times of CdSe QDs as a function of the excitonic volume.

2.3 Charge Transfer Kinetics

Charge trapping at crystalline defects is the predominant nonradiative decay mechanism that limits QD photoluminescence efficiencies. Trapping is commonly attributed to mid-gap electronic states associated with undercoordinated atoms, impurities, or lattice defects.[17,18,19] In the II-VI nanoparticles, the energy levels of undercoordinated surface chalcogenide ions are typically within a few hundred meV above the valence band edge. Depending on their energies and the redox properties of the system, these states can either be filled or empty, allowing them to either donate an electron to the VB level (hole trapping) or to accept an electron from the CB (electron trapping) after photoexcitation. A third situation arises when empty surface states exist within kT of the VB edge, in which case thermal population of the surface states gives rise to steady state hole populations (surface charging).[20-23] All three processes results in a loss of carrier population and photoluminescence intensity and manifest as a fast decay in the PL kinetics as measured in a time-correlated single photon counting (TCSPC) experiment. Electron and hole trapping are depicted below in Figure 2.4

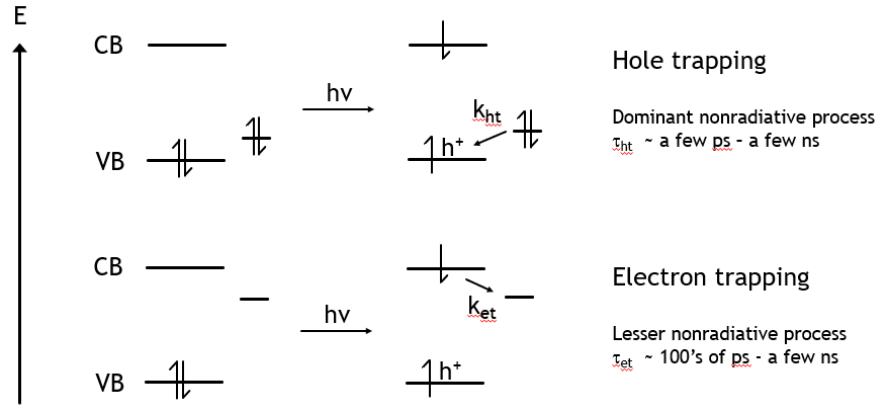

Figure 2.4 Energy level diagrams showing hole trapping (top) and electron trapping (bottom) after photoexcitation.

Hole trapping tends to be the dominant carrier trapping process, with typical trapping times in CdSe QD in the 1's - 100's of ps regime, while electron trapping is usually 1-2 orders of magnitude slower, usually occurring over 100's of ps to a few ns. A convincing explanation for the large deviation between the two rates has proved elusive because of the small density of trap states relative to the bulk material as well as inhomogeneities in the particle shape and surface structure. Several theoretical studies have provided insight into the nature of the defect states, but it's difficult to calculate meaningful results without structural characterization data as a starting point. However, a back-of-the-envelope Marcus theory calculation sometimes suffices to provide estimates of the thermodynamic driving forces, densities of trap states, and electronic coupling matrix elements. The Marcus Theory equation for non-adiabatic electron transfer is shown below in Equation E2.8.[40] The non-adiabatic expression is valid in the limit of weak electronic coupling, and this situation is realized in QD due to the small spatial overlap of the delocalized band edge electron or hole states and the surface-localized trap states.[24]

$$k_0 = \frac{1}{h} |H_{12}|^2 \frac{e^{-(\lambda+\Delta G)^2/4\lambda k_B T}}{\sqrt{4\pi k_B T}} \qquad \text{E2.8}$$

Where k_0 is the rate for a single donor-acceptor pair, H_{12} is the electronic coupling matrix element, ΔG the energy difference between initial and final states, and λ is the reorganization energy. The more likely scenario on a QD is a distribution of surface trap densities and energies. Since the number of defects is small and their occurrence is uncorrelated, the distribution of trap densities follows Poisson statistics, while the trap energies are distributed randomly.[24] The transfer rate of each particle scales with the number of acceptors, so calculation of the intrinsic rate constant requires knowing the surface trap densities. If the average number of acceptors is known, E2.8 can be used, in theory, to back out the electronic coupling elements. However, the electron transfer kinetics would have to be modeled as a multiexponential decay, which doesn't tend to give a robust fit when the number of components is large. This problem is easily solved by adding a small concentration of a molecular acceptor such that the average number of

acceptors is much less than one, giving a distribution where only the n = 1 component has significant amplitude. Of course, this can only be achieved with an externally adsorbed acceptor, so the energetics of the QD surface can only be approximated, and rigorous quantitative analysis of surface trapping therefore remains elusive.

$$k_{obs}(N,n) = \sum_n \frac{N^n e^{-N}}{n!}\, n * k_0 \qquad \text{E2.9}$$

Where N is the average number of acceptors and n is the number on any given particle. Inhomogeneities in the trap state energies can also be accounted for by taking a distribution around each $n*k_0$.

One of the successes of Marcus Theory was in predicting the Marcus-inverted regime, where the rates are seen to decrease with increasing ΔG for driving forces greater than the reorganization energy. The inverted regime isn't seen in QD, however, and the absence is explained by an Auger-assisted transfer mechanism,[25] where excess kinetic energy of the electron can be conserved through excitation of the hole into the manifold of low-energy excited hole levels. It follows that electron transfer rates should depend strongly on the charge state of the particle. Removal of the hole before electron transfer significantly changes the energetics of the system. Since the trapped hole is spatially removed from the electron, the Auger coupling is lost and doesn't enter into the rates. This shouldn't have much of an effect in the Marcus normal region ($-\Delta G < \lambda$), while systems with $-\Delta G > \lambda$ should show a dramatic decrease in the ET rates. The isolated electron state is destabilized relative to the excitonic state by the e-h Coulomb and polarization energies, so $-\Delta G$ should be greater when the hole is trapped. In contrast, the reorganization energy is dominated by solvent and inner-sphere reorganization in the adsorbed acceptor and is therefore largely independent of the QD environment. Typical values of λ range between 200 and 500 meV.[24] Finally, since both the e-h Coulomb interactions and the valence band structure depend sensitively on particle morphology, it follows that very different behavior is expected for 2D nanoplatelets and spherical nanoplatelets.

2.4 Angular Momentum Fine Structure

The band-edge excitonic transition in a CdSe QD can be described loosely as exciting an electron from the filled Se 4p subshell into empty Cd 5s orbitals. This is captured in the unit cell-localized part u(r,k) of the Bloch wavefunction Ψ(r,k) given in equation E2.10. The extent to which charge transfer occurs varies from one unit cell to the next and is expressed in the envelope part φ(r,k) of the Bloch function shown below[4\

$$\Psi(r,k) = u(r,k)\,\varphi(r,k) \qquad \text{E2.10}$$

The Se 4p orbitals are 6-fold degenerate and the Cd 5s orbitals are 2-fold degenerate, resulting in 12 different microstates available for the excitonic transition. These states are labeled according to the combined angular momentum of the Cd 5s electron (the electron) and the Se 4p vacancy (the hole). Spin-orbit coupling splits the states with a hole angular momentum (J_h) equal to 1/2 and the J_h = 3/2 states by 0.42 eV,[26] making the J = 1/2 (the split-off or SO band) well-resolved from the band-edge states. In a spherical particle of cubic lattice symmetry, x-, y-, and z-polarized states are all degenerate. In non-cubic lattice structures such as wurtzite, crystal field splitting lifts the 3-fold translational symmetry, and deviations from spherical symmetry in the particle shape (shape anisotropy), further lifts the degeneracy. Typical zincblende (ZB) CdSe QD are slightly oblate, causing the light hole (LH) band, which is composed of x-, y-, and z-polarized states, to be destabilized by ~ 40 meV with respect to the heavy hole (HH) band, which is entirely xy-polarized. This is well within the inhomogeneous broadening associated with typical particles size distributions (~ 100 meV), making the LH/HH bands unresolved.

The two four-fold degenerate levels resulting from crystal field and shape anisotropy splitting are further split by the electron-hole exchange interaction, which stabilizes states with greater spin angular momenta. Exchange coupling between the electron and hole spins is represented as a direct product (or Kroenecker product) of the Pauli 1/2 and 3/2 spin matrices (σ and j, respectively) in the exchange Hamiltonian H_{exch} in E2.11, where the value of the exchange constant (ε_{exch}) is determined from measured values of the bulk singlet-triplet splitting.[4]

$$H_{exch} = \frac{2}{3}\left(\frac{a_0}{a_X}\right)^3 \varepsilon_{exch}\,\sigma \otimes J \qquad \text{E2.11}$$

Where a_0 is the lattice parameter, a_X is the excitonic radius, and $\otimes$ is the symbol for the direct product. The fine structure states can then be calculated by treating the exchange and shape anisotropy terms in the Hamiltonian as a perturbation to the non-interacting particle-in-a-sphere electron and hole states.[4] This calculation is gone though in detail in Appendix A for the simple case of spherical particles of cubic lattice symmetry. Figure 2.5 outlines all these effects and the resulting fine structure of the lowest energy exciton.

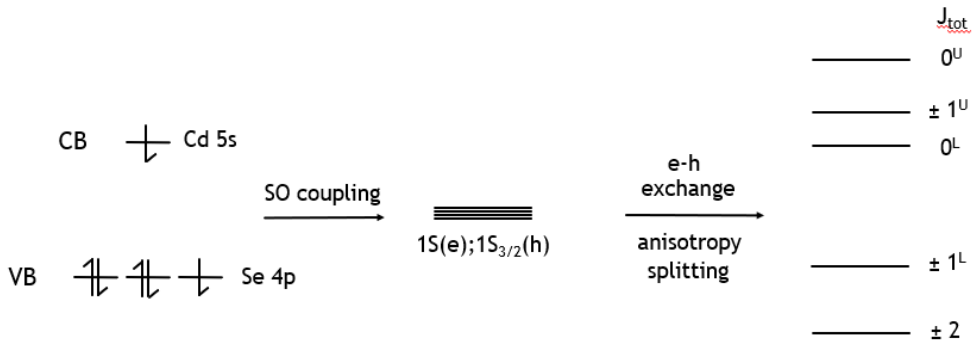

Figure 2.5 Fine structure levels of the lowest energy excitonic state in quantum-confined zincblende QDs [18]

The first optically allowed state (the ± 1^L) sits 15-25 meV higher than the ± 1^L, depending on the particle size, while the upper manifold of states (the LH band) begins about 30 meV higher than the ± 1^L. The net result is that, after thermal equilibration, the majority of the excitonic population is in the dark exciton, and the observed radiative lifetimes are therefore much longer than one would predict based on the extinction coefficients measured in a static absorption experiment.[4,27-29] The oscillator strengths of the transitions from the ground state to each of the fine structure levels and the effect on the observed radiative lifetime is detailed below in Figure 2.6.

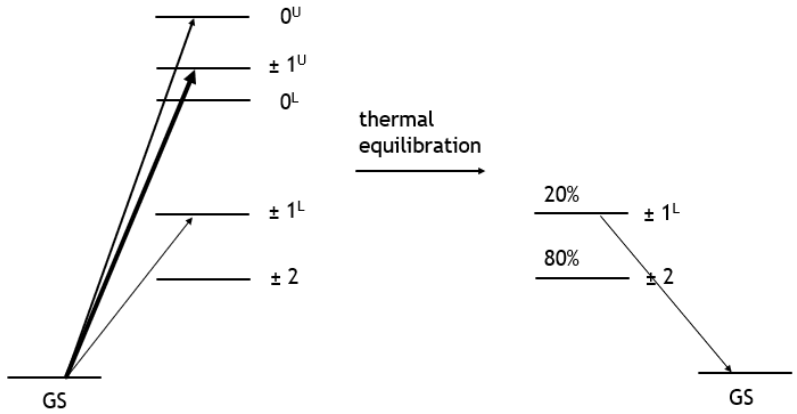

Figure 2.6 Allowed transitions from the QD ground state to the various fine structure levels of the $1S_{3/2}$-1S exciton. The thickness of each arrow signifies the relative oscillator strengths of each transition as calculated in ref 4.

Because the exciton fine structure is determined by crystal size and shape, it follows that particle morphology should play a key role in determining luminescence and excited state absorbance properties. In the case of nanoplatelets, which are strongly confined along one axis and weakly along the other two, the LH/HH splitting is anywhere from 140 to 180 meV. Because the nanoplatelet xy-dimensions have a much smaller effect on the band gap than the z dimension, inhomogeneous broadening is less than that of typical QD samples, and the LH and HH bands are therefore spectrally resolved,

making the band-edge transition entirely xy-polarized.[30,31] Furthermore, the electron-hole exchange interaction is much weaker in nanoplatelets than it is in spherical particles. This has profound effects on the transient absorption spectra and radiative lifetimes. The platelet e-h exchange interaction is small compared with kT (~5 meV),[32] so the Boltzmann populations of the $\pm 1^L$ and ± 2 at room temperature are 45% and 55% . All else being equal, this would result in the platelet radiative rates being faster than QD rates. This is consistent with experimental observations, but many other effects also factor into the comparison between QD and NPL radiative lifetimes, therefore an entire chapter will be devoted to this topic. A simplistic comparison between the angular momentum fine structure of the NPL and QD exciton is shown below in Figure 2.7.

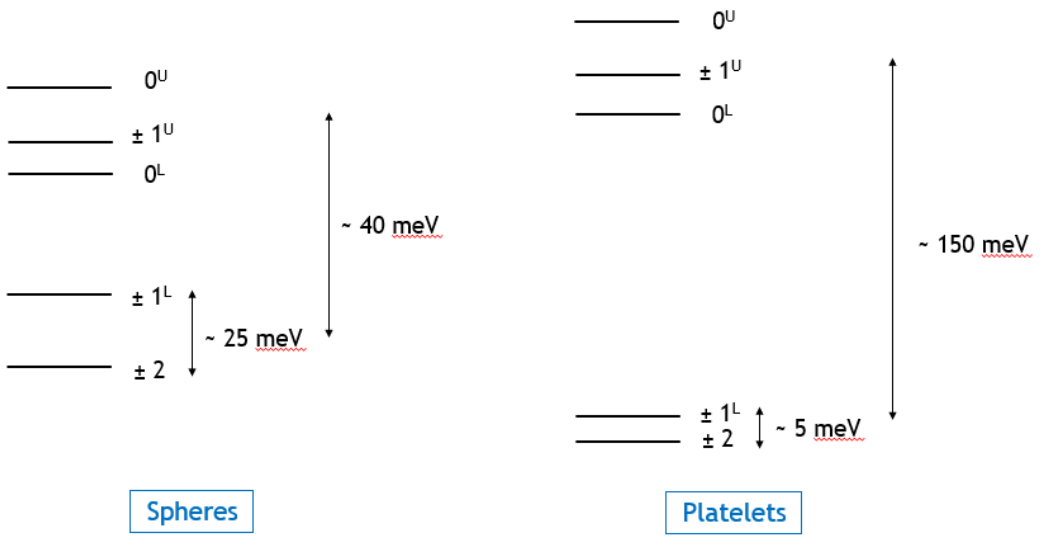

Figure 2.7 Angular momentum fine structure of the band edge exciton in slightly oblate CdSe QDs (left) compared with 2D nanoplatelets (right). Energies are not drawn to scale.

Many of the observed dynamical properties of CdSe nanoparticles derive from the excitonic fine structure. For example, many authors have observed that the transient absorption decay kinetics are unaffected by hole trapping[11,33,34,35]. This is particularly useful in assigning carrier trapping processes, and many of the studies contained herein take advantage of this fact.[33,34,36] . The $1S_{3/2}$-1S bleach magnitude is sensitive only to conduction band populations, whereas the PL intensity decays due to loss of either conduction band or valence population. The TA and PL decay kinetics can therefore be compared to deduce what type of carrier trapping process is resulting in loss of PL efficiency. The insensitivity of CdSe QD TA spectra to valence band populations has been attributed to the large VB degeneracy and the optically inactive nature of the lowest excitonic state.[11,4] While these factors do come into play in the analysis of the bleach magnitudes, merely citing them does not truly explain why hole trapping has no effect on the excited state absorption. An accurate description involves comparing the excited state absorption (ESA) energies and cross-sections of the excitonic state φ_X, where both the electron and hole are present, with the negatively charged particle φ_-, where the hole has been removed and the CB electron remains in the particle. Exciting from the excitonic

state results in a biexciton (φ_{XX}) while exciting a negatively charged particle results in the negative trion (φ_{X-}), a state characterized by two conduction band electrons and one valence band hole. The $\varphi_{-} \rightarrow \varphi_{X-}$ transition is blueshifted relative to the $\varphi_X \rightarrow \varphi_{XX}$ transition by ~ 5 nm,[37] but this is small compared to the width of the ESA transition and the bleach band, so the spectral shift is unresolved and cannot be used as a signature of hole trapping. This leaves the lack of any difference in ESA oscillator strengths to be accounted for. The X → XX and the various trion transition oscillator strengths are calculated in reference 38 and 39 respectively, and the pertinent transitions are shown in Figure 2.8. As previously stated, after thermal relaxation, the CdSe QD excitonic population is distributed mainly between the two lowest fine structure levels. The oscillator strengths from the $\pm 1^L$ and ± 2 to each of the biexcitonic states are weighted by their relative populations then summed. The contribution to the TA spectrum due to stimulating emission from the $\pm 1^L$ to the ground state is then subtracted from the sum of the ESA oscillator strengths, as stimulated emission yields a TA feature at the same energy but with the opposite sign of ESA. It turns out that the sum of all of these oscillator strengths is exactly the same as the oscillator strength of the $\varphi_{-} \rightarrow \varphi_{X-}$ transition, which is a fully allowed doublet → doublet transition. Therefore, removal of a valence band hole has no effect on the transient absorption spectra. Because the angular momentum fine structure varies based on the particle morphology, one wouldn't expect to encounter the exact same situation in the case of nanoplatelets or possibly nanorods. An entire chapter is therefore devoted to exploring the spectroscopic manifestations of hole trapping in CdSe nanoparticles of different morphologies.[34]

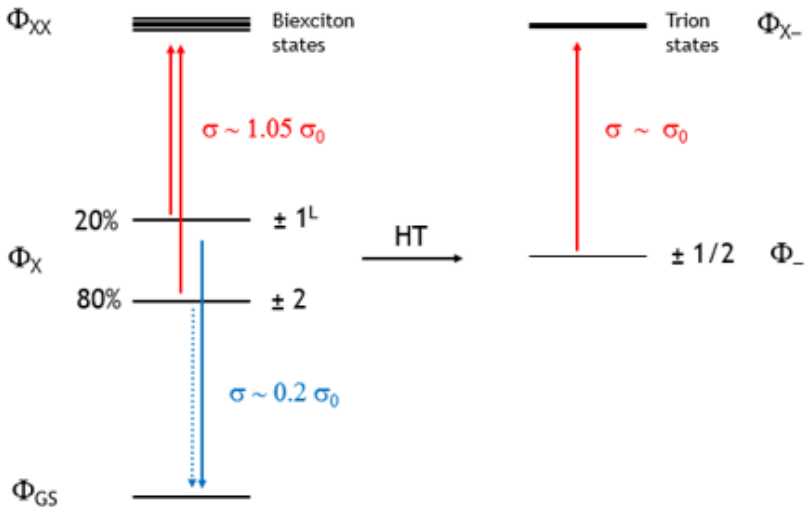

Figure 2.8 Equilibrium populations and oscillator strengths for transitions between the ground (φ_{GS}), single exciton HH (φ_X), and biexciton states (φ_{XX}) and the comparison with the negatively charged particle following hole trapping.

2.5 Transient Absorption Spectroscopy

The majority of the results presented in this work were obtained using the transient absorption (TA) spectrometer described below. A brief description of how the measurements are taken, how the TA spectra are calculated, and the physical processes that give rise to the signal will be detailed here.

A Clark-MXR chirped pulse amplification (CPA) Ti-sapphire laser is used to generate pulses of 775 nm light at a repetition rate of 1 kHz with 140 fs pulse duration. The beam is split along two paths to generate the excitation beam (the pump) and the beam used to measure excited-state absorption spectra (the probe). The 387 nm pump beam is generated by passing the 775 nm beam through a BBO frequency doubling crystal. It then travels along a path containing a corner cube mounted on a translation stage and an optical chopper before arriving at the sample. The position of the translation stage determines the relative arrival time of the pump and the probe, yielding measurements of the excited state absorption spectra as a function of the time after photoexcitation. The pump chopper is synchronized to the cavity dumper and cycles at half the frequency of the excitation beam, blocking every other excitation pulse. This allows measurements to be taken subsequently both in the presence and absence of the excitation beam, 500 times per second. Along the probe path, the 775 nm light is focused onto a sapphire plate to generate a white light continuum with which to collect absorption spectra. The probe is then spatially and temporally overlapped with the pump at the sample. After passing through the sample, the pump is removed from the beam using a dielectric mirror, leaving just the probe behind. The probe is split along two paths using a corner cube, and both probe beams are then sent through opposite sides of an optical chopper that cycles at the frequency of the probe beam. The alignment of the probes and phase of the chopper are set such that when one probe passes, the other one is blocked. This achieves spatial separation of the probe signals in the presence (I_{on}) and absence (I_{off}) of the excitation beam. The two signals are then imaged onto different vertical positions of a CCD, allowing them to be independently read off and used to calculate TA spectra. The layout of the experimental apparatus is shown in Figure 2.9.

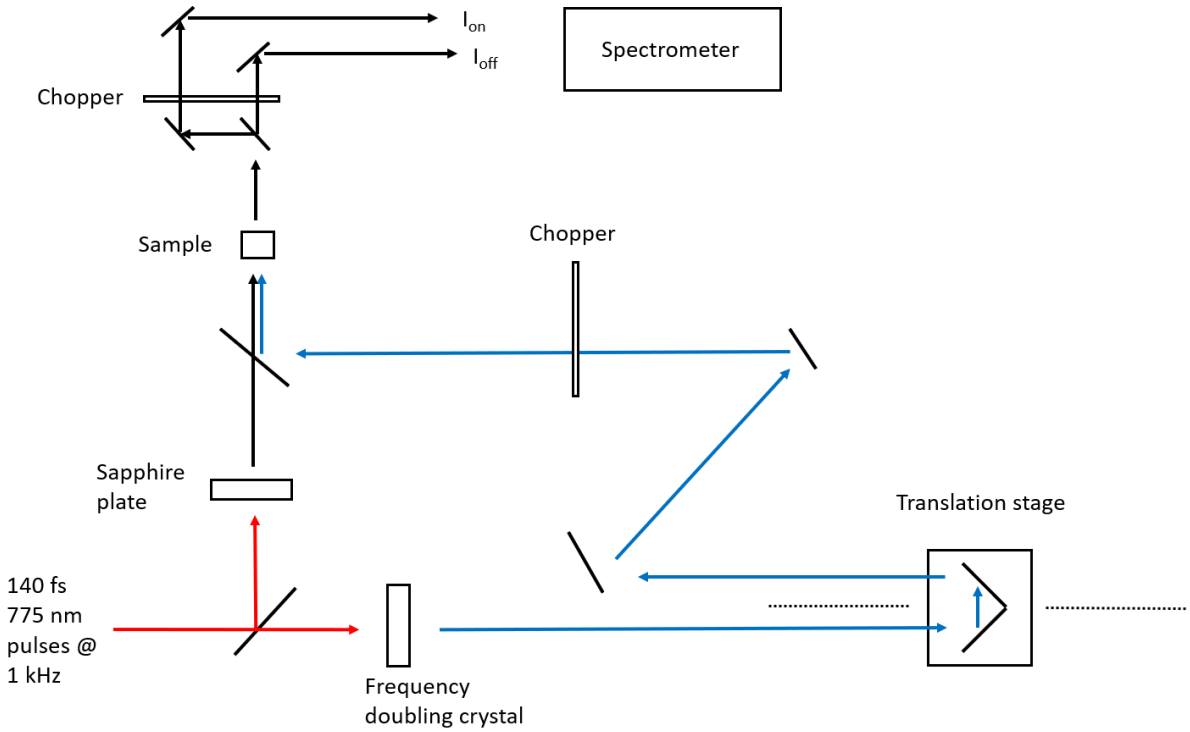

Figure 2.9 Simplified diagram of the ps transient absorption experimental apparatus.

TA spectra are presented as ΔA, or the difference in ground and excited state absorbance, vs wavelength. A is given as the log of the ratio of the incident and transmitted intensities, but taking the difference between the two absorbances allows one to factor out the incident intensity, making it unnecessary to measure against a blank. Instead, ΔA is calculated from the transmitted intensities I_{on} and I_{off}, as shown in Figure 2.10.

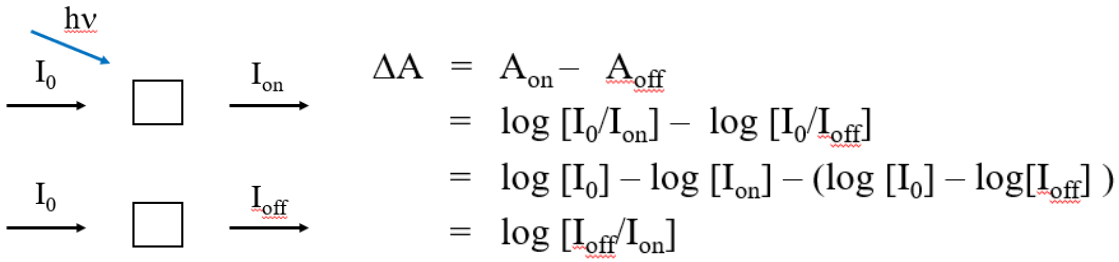

$$\begin{aligned}\Delta A &= A_{on} - A_{off} \\ &= \log [I_0/I_{on}] - \log [I_0/I_{off}] \\ &= \log [I_0] - \log [I_{on}] - (\log [I_0] - \log[I_{off}]) \\ &= \log [I_{off}/I_{on}]\end{aligned}$$

Figure 2.10 Left: illustration of the transmitted intensities I_{on} and I_{off}. Right: calculation of ΔA from the transmitted intensities

According to the above expression for ΔA, if the transmitted intensity after photoexcitation is greater than in the ground state, ΔA is negative. Absorption of a photon by a semiconductor nanoparticle excites a valence band electron into the conduction band. Absorption of a second photon is partially blocked since the conduction band already has an electron in it, ie the transition degeneracy, and therefore the

extinction coefficient, is reduced. This is known as state filling and manifests as a reduction in the excited state absorption seen in the TA spectra. Transitions from higher energy valence band levels to the lowest conduction band state are similarly bleached. Absorption of a second photon in the probe beam is known as photoinduced absorption (PA) or excited state absorption (ESA) and appears as a positive feature in the spectra. The PA bands in a TA spectrum are redshifted by the presence of the first exciton due to the Stark effect, where the interaction of the nascent exciton is shifted to lower energies because of the interaction with the electric field of the existing electron-hole pair. The magnitude of the shift is known as ΔXX, the biexciton binding energy, and can be extracted from fitting the spectra to a model that accounts for ground state bleaching, stimulated emission, and the Stark-shifted photoinduced absorption.[11] To do this, one must first fit the static absorption spectra to get the magnitudes, widths, and positions of the transitions observed in the TA spectral window. A representative absorbance spectrum and its fit as well as the observed transitions are shown in Figure 2.11.

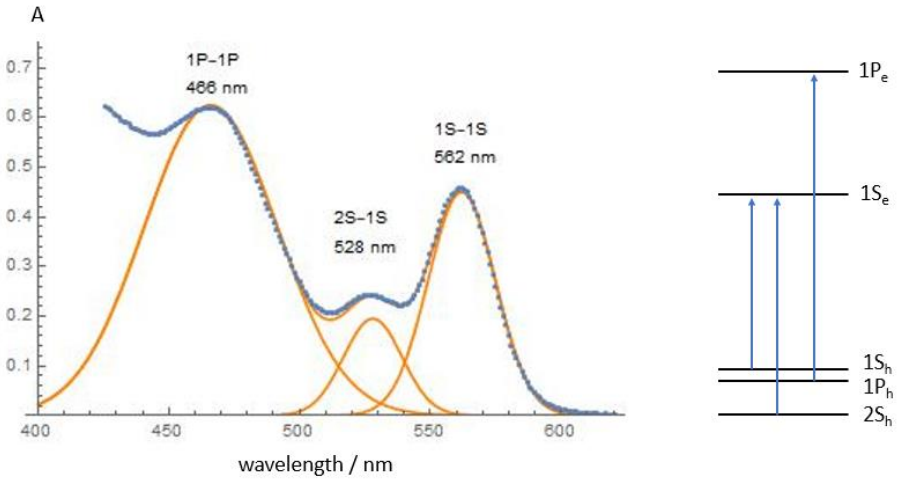

Figure 2.11 Static absorption spectrum of 3.3 nm diameter CdSe nanoparticles (left) and an energy level diagram showing the observed transitions in the uncoupled electron-hole representation.

The TA spectra are modeled by assuming that each transition in the static spectrum is 100% bleached and redshifted by the same amount, and that the PA associated with transitions ending in the $1S_e$ CB level are reduced by half due to state filling. The only adjustable parameter is ΔXX, allowing this value to be assigned from the fit. Figure 2.12 shows this procedure and the fit to the TA spectrum of the same particles shown in 2.11. The fit breaks down at shorter wavelengths due to the presence of other transitions underlying the 1P-1P feature; failing to account for these other transitions in the static fit resulted in an 1P-1P that is too broad and intense.

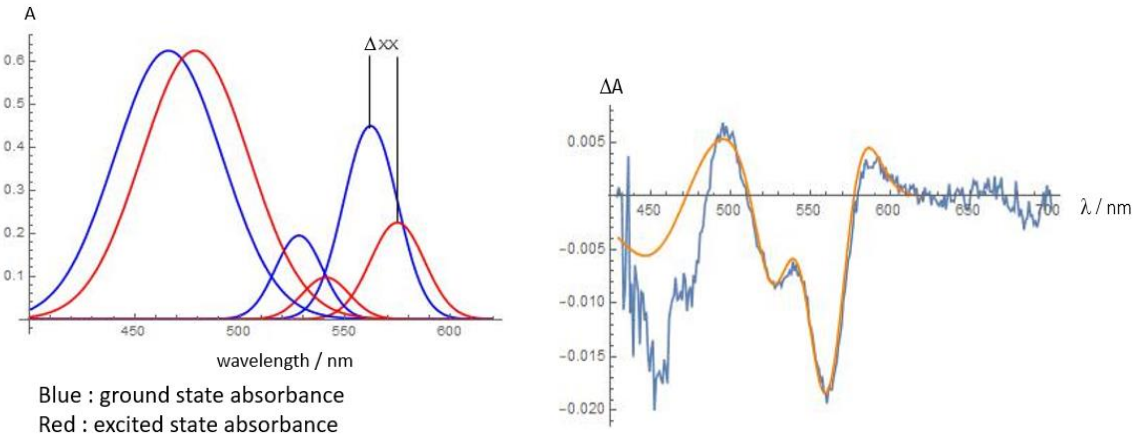

Figure 2.12 Individual ground and excited state transitions modeled as Gaussian lineshapes (left), and the fit of the TA spectrum (right) using the above model

Carrier populations, charge transfer processes, and multiexciton dynamics can all be analyzed through the wavelength-dependent TA kinetics. Regions of the spectra are averaged and plotted as a function of the delay time between pump and probe, allowing for quantitative analysis of the physical processes undergone after photoexcitation.
Figure 2.11 Static absorption spectrum of 3.3 nm diameter CdSe nanoparticles (left) and an energy level diagram showing the observed transitions in the uncoupled electron-hole representation.

Ch 2 References

1. Levine, I. N. *Quantum Chemistry*. 7th ed.; Pearson: London, 2014.
2. Wikipedia. Noether's Theorem. https://en.wikipedia.org/wiki/Noether%27s_theorem (accessed Jan 5, 2019)
3. Kelley, A. M. *Condensed-Phase Molecular Spectroscopy and Photophysics*. John Wiley & Sons, Inc.: Hoboken, NJ, 2013.
4. Efros, A. L.; Rosen, M.; Kuno, M.; Nirmal, M.; Norris, D. J.; Bawendi, M. Band-Edge Exciton in Quantum Dots of Semiconductors With a Degenerate Valence Band: Dark and Bright Exciton States. *Phys. Rev. B: Condens. Matter Mater. Phys*. **1996**, *54*, 4843−4856.
5. Nirmal, M.; Dabbousi, B. O.; Bawendi, M. G.; Macklin, J. J.; Trautman, J. K.; Harris, T. D.; Brus, L. E. Fluorescence Intermittency in Single Cadmium Selenide Nanocrystals. *Nature* **1996**, *383*, 802.
6. Gong, K.; Zeng, Y.; Kelley, D. F. Extinction Coefficients, Oscillator Strengths, and Radiative Lifetimes of CdSe, CdTe, and CdTe/CdSe Nanocrystals. *J. Phys. Chem. C.* **2013**, *117*, 20268−20279.
7. Brovelli, S.; Schaller, R. D.; Crooker, S.A.; García-Santamaría, F.; Chen, Y.; Viswanatha, R; Hollingsworth, J.A.; Htoon, H.; Klimov, V.I. Nano-engineered electron-hole exchange interaction controls exciton dynamics in core-shell semiconductor nanocrystals. *Nat. Comm.* **2011**, *2*, 280.
8. Nirmal, M. et al. Observation of the dark exciton in CdSe quantum dots. *Phys. Rev. Lett*. **1995,** *75*, 3728–3731.
9. Kuno, M., Lee, J. K., Dabbousi, B. O., Mikulec, F. V. & Bawendi, M. G. The band edge luminescence of surface modified CdSe nanocrystallites: probing the luminescing state. *J. Chem. Phys.* **1997**, *106*, 9869–9882.
10. Kolasinski, K. W. *Surface Science: Foundations of Catalysis and Nanoscience*. 2nd ed.; Wiley: New York City, 2012.
11. Klimov, V.I. Spectral and Dynamical Properties of Multiexcitons in Semiconductor Nanocrystals. *Annu. Rev. Phys. Chem.* **2007**, *58*, 635-73.
12. Climente, J. I.; Movilla, J. L.; Planelles, J. Auger Recombination Suppression in Nanocrystals with Asymmetric Electron-Hole Confinement. *small*. **2012**, *8*, 754-759.
13. Kuno, M. *Introductory Nanoscience*. Garland Science, Taylor & Francis Group: New York, 2012.
14. Yu, P. Y.; Cardona, M. *Fundamentals of Semiconductors*. 4th ed.; Springer: New York, 2010.
15. Beane, G. A.; Gong, K.; Kelley, D. F. Auger and Carrier Trapping Dynamics in Core/Shell Quantum Dots Having Sharp and Alloyed Interfaces. *ACS Nano*. **2016,** *10*, 3755-3765.
16. Morgan, D.; Gong, K.; Kelley, A. M.; Kelley, D. F. Biexciton Dynamics in Alloy Quantum Dots. *J. Phys. Chem. C*. **2017**, *121*, 18307-18316
17. Houtepen, A. J.; Hens, Z.; Owen, J. S.; Infante, I. On the Origin of Surface Traps in Colloidal II-VI Semiconductor Nanocrystals. *Chem. Mater*. **2017**, 29, 752−761.

18. Giansante, C.; Infante, I. Surface Traps in Colloidal Quantum Dots: A Combined Experimental and Theoretical Perspective. *J. Phys. Chem. Lett.* **2017,** 8, 5209-5215.
19. Boles, M.; Ling, D.; Hyeon, T.; Talapin, D. The surface science of nanocrystals. *Nature Materials*. **2016**, 15, 141−153.
20. Cai, X.; Martin, J. E.; Shea-Rohwer, L. E.; Gong, K.; Kelley, D. F. Thermal Quenching Mechanisms in II-VI Semiconductor Nanocrystals. *J. Phys. Chem. C*, **2013**, *117(15)* 7902-7913.
21. Gong, K.; Kelley, D. F. Surface Charging and Trion Dynamics in CdSe-Based Core/Shell Quantum Dots. *J. Phys. Chem. C*, **2015**, *119*(17), 9637-9645.
22. Zeng, Y.; Kelley, D. F. Surface Charging in CdSe Quantum Dots: Infrared and Transient Absorption Spectroscopy. *J. Phys. Chem. C*, **2017**, *121*(30), 16657-16664.
23. Morgan, D.; Kelley, D. F. Spectroscopy of Surface-State p-Doped CdSe/CdS Quantum Dots. *J. Phys. Chem. Lett.*, **2018**, *9*(15), 4160-4165.
24. Zhu, H.; Yang, Y.; Wu, K.; Lian, T. Charge Transfer Dynamics from Photoexcited Semiconductor Quantum Dots. *Annu. Rev. Phys. Chem.* **2016**, *67*, 259-281.
25. Zhu, H. et. al. Auger-Assisted Electron Transfer from Photoexcited Semiconductor Quantum Dots. *Nano Lett.* **2014,** *14*, 1263-1269.
26. Norris, D. J.; Efros, A, L.; Rosen, M.; Bawendi, M. G. Size Dependence of Exciton Fine Structure in CdSe Quantum Dots. *Phys. Rev. B.* **1996**, *53*(24), 16347-16354.
27. Nirmal, M.; Norris, D. J.; Kuno, M.; Bawendi, M. G.; Efros, A. L.; Rosen, M. Observation of the "Dark Exciton" in CdSe Quantum Dots. *Phys. Rev. Lett.* **1995**, 75(20), 3728-3731.
28. Gong, K.; Zeng, Y.; Kelley, D. F. Extinction Coefficients, Oscillator Strengths, and Radiative Lifetimes of CdSe, CdTe, and CdTe/CdSe Nanocrystals. *J. Phys. Chem. C*, **2013**, *117*, 20268-20279.
29. Gong, K.; Martin, J. E.; Shea-Rohwer, L. E.; Lu, P.; Kelley, D. F. Radiative Lifetime of Zincblende CdSe/CdS Quantum Dots. *J. Phys. Chem. C*, **2015**, *119*, 2231-2238.
30. Scott, R.; et. al. Directed emission of CdSe nanoplatelets originating from strongly anisotropic 2D electronic structure. *Nat. Nanotech.* **2017**, *12*, 1155
31. Ithurria, S.; Tessier, M. D.; Mahler, B.; Lobo, R. P. S. M.; Dubertret, B.; Efros, A. L. Colloidal nanoplatelets with two-dimensional electronic structure. *Nat. Mat.* **2011**, 936
32. Shornikova, E.; et al. Addressing the exciton fine structure in colloidal nanocrystals: the case of CdSe nanoplatelets. *Nanoscale*. **2018**, *10*, 646-656.
33. Morgan, D. P.; Kelley, D. F. Mechanism of Hole Trap Passivation In CdSe Quantum Dots by Alkylamines. *J. Phys. Chem. C.* **2018**, ASAP.
34. Morgan, D. P.; Maddux, C. J. A.; Kelley, D. F. Transient Absorption Spectroscopy of CdSe Nanoplatelets. *J. Phys. Chem. C.* **2018**, 122, 23772−23.
35. Song, N.; Zhu, H.; Jin, S.; Lian, T. Hole Transfer from Single Quantum Dots. *ACS Nano*. **2011**, *11*, 8750-8759.

36. Morgan, D.; Kelley, D. F. Role of Surface States in Silver-Doped CdSe and CdSe/CdS
Quantum Dots. *J. Phys. Chem. C* **2018** , 122, 10627−1063
37. Morgan, D.; Kelley, D. F. Spectroscopy of Surface State p-Doped CdSe/CdS Quantum Dots. *J. Phys. Chem. Lett.* **2018** , 9, 4160−4165
38. Rodina, A. V.; Efros, A. L. Band-edge biexciton in nanocrystals of semiconductors with a degenerate valence band. *Phys. Rev. B.* **2010**, *82*, 125324
39. Shabaev, A.; Rodina, A. V.; Efros, A. L. Fine structure of the band-edge excitons and trions in CdSe/CdS core/shell nanocrystals. *Phys. Rev. B.* **2012**, 205311.
40. Marcus, R. A. Chemical and electrochemical electron-transfer theory. *Annu. Rev. Phys. Chem*. **1964**, *15*, 155–196

Ch 3

Biexciton Dynamics in Alloyed $Zn_xCd_{1-x}Se$

Abstract

The biexciton Auger dynamics of alloyed $Zn_{1-X}Cd_XSe/ZnS$ and $Zn_{1-X}Cd_XSe/CdS$ core/shell nanoparticles are examined as a function of alloy composition. A series of particles with increasing cadmium mole fractions are prepared by synthesizing ZnSe then performing a cation exchange reaction with cadmium oleate. This is followed by the low temperature deposition of a CdS or ZnS shell to passivate surface traps. The percent composition of cadmium in the cores is determined from the absorption spectrum upon cation exchange, and the excited state dynamics are measured using power-dependent transient absorption spectroscopy. The biexciton lifetimes are controlled by Auger recombination and the results show that the Auger rates of the alloyed particles are less than those of the pure ZnSe or pure CdSe, going through a minimum around 10 – 40% cadmium. This behavior is assigned to partial hole localization in Cd-rich regions in the alloy along with the strong size dependence that is known for Auger processes in nanocrystals. The results can be semiquantitatively understood in terms of effective mass calculations of the hole wavefunctions on random (Cd,Zn)Se lattices of varying average compositions corresponding to alloyed nanocrystals of this size. We show that the hole wavefunction gradients (taken to be related to the Auger rates) also go through a maximum at approximately these alloy compositions.

3.1 Introduction

Biexciton dynamics are of great importance in any application of quantum dots (QDs) involving high rates of excitation, such as solar energy conversion, lasing, and lighting in displays. Biexcitons are also formed as a result of multiple exciton generation, in which absorption of a high-energy photon results in the production of multiple electron-hole pairs. The biexciton dynamics are dominated by Auger processes, which occur over timescales of 1 ps up to 100's of picoseconds in typical QDs. Auger recombination is a 3-body process where an e/h pair recombine and transfer the excess kinetic energy to a third carrier. The initial e/h states are at the Γ point ($k = 0$) of the Brillouin zone, while the receiving carrier is promoted through an intraband transition to the high energy continuum levels ($k \neq 0$), making Auger recombination a momentum-forbidden process. Because of the greater density of states in the valence band, the hole is typically the dominant receiving particle in the II-VI semiconductors. Hole effective masses also tend to be greater than in CB electrons, so hole wavefunctions are typically more localized and therefore have a larger contribution from higher-momentum Fourier components. This facilitates Auger recombination by relaxing the momentum conservation constraint. Localization of the exciton to the particle dimensions allows us to express the electron and hole wavefunctions as a superposition of bulk wavefunctions having a range of momenta, which is simply an Uncertainty Principle consideration. The presence of high-momentum components in the Fourier expansion partially relaxes the momentum selection rule, making the Auger process partially allowed. The extent to which this happens depends on the spatial extent of the wavefunction and hence the particle size. Smaller particles have greater high-

momentum components and hence faster Auger recombination rates. In addition, electron-hole Auger recombination occurs through the Coulomb interaction, the magnitude of which depends on the average electron-hole separation. Thus, there is a larger Coulomb matrix element associated with confining carriers to a smaller volume particle. The result of these factors is the approximate volume scaling of the biexciton lifetimes that is experimentally observed.[1] A more detailed treatment of Auger recombination is given in Ch 2.2.

The size of the electron or hole wavefunction can be affected by factors other than the particle size. We have recently shown that holes can trap at defects at the interface in core/shell QDs.[2] These trapped holes are far more spatially localized than band-edge holes and correspondingly have larger amplitude high-momentum components. The result is that core/shell QDs having holes trapped at the core/shell interface exhibit Auger recombination rates that are several times faster than those lacking interfacial traps. In any ensemble of particles, some subset will have hole-trapping interfacial defects and show a fast component of the biexciton Auger decay. The remainder of the particles give the slow decay characteristic of band edge holes. Thus, ensemble transient absorption measurements typically yield nonexponential biexciton decays. Softening the core-shell interface through thermal annealing decreases the relative amplitude of the fast Auger component while leaving the Auger times unchanged. If the Auger times were directly related to interface sharpness, the decay times would change upon annealing, whereas changes in amplitude reflect a redistribution of the sub-populations with and without interface defects. Furthermore, the change in amplitude ratio is commensurate with the increase in PLQY.

Another way to localize holes is through the introduction of impurities.[3, 4] This occurs at the first stages of alloying a semiconductor QD via cation exchange. We have recently examined the extent of exciton-phonon coupling (EPC) in $Zn_{1-x}Cd_xSe$, x = 0 – 1.[4] The QD exciton couples to the phonons through a Fröhlich mechanism.[20] That is, if the nascent electron and hole have different spatial extents then there is an electric field associated with the electron-hole pair. The electric field displaces the atoms of the polar crystal along the optical phonon coordinates. Because of its smaller effective mass, the electron wavefunction typically has a slightly larger spatial extent than the hole. In pure, single material QDs this difference is minimal, and pure QDs exhibit relatively small Huang-Rhys parameters. Recent results indicate that QDs of both ZnSe and CdSe pure materials exhibit rather small electron-phonon couplings. The Huang-Rhys parameter is a quantitative measure of EPC, and ZnSe QDs give values on the order of 0.2 to 0.5, which is about a factor of 2 larger than what is obtained for CdSe QDs of similar size.[5] The $Zn_{1-x}Cd_xSe$ alloys show dramatically different behavior. The key to this difference is that these are random, rather than uniform alloys. For small values of x, the Cd atoms can randomly cluster together, resulting in low energy valence band regions in the particle. Holes can localize at these regions, resulting in large electric fields and hence large EPCs. We reported that the alloyed QDs exhibit much larger overtone to fundamental ratios in the Raman spectra than either of the pure materials, indicative of larger coupling of the exciton to the phonons.

These results suggest that other dynamics associated with more localized holes should also be observed in these alloyed QDs. The Auger rate depends on the extent to which the momentum selection rule is relaxed, i.e., the magnitude of the high momentum components

comprising the hole wavefunction. These can be calculated by Fourier transforming the spatial wavefunction and evaluating the resulting wavefunction at the momentum corresponding to the exciton energy.[6-8] The qualitative conclusion is that the high momentum components are due to rapid spatial variation of the wavefunction and therefore increase with the spatial wavefunction gradients. Based on this simple consideration, we expect that hole localization in the alloys will result in faster biexciton Auger times. In this study, we use transient absorption spectroscopy to measure the biexciton decay rates in a series of alloyed $Zn_{1-x}Cd_xSeCdS$ and $Zn_{1-x}Cd_xSeZnS$ core/shell QDs. Hole wavefunctions for random alloys with specified average composition are calculated, and the gradients of the wavefunction are evaluated and compared with experimental results.

3.2 Results & Discussion

3.2.1 Extent of cation exchange by static absorption

Absorption spectra of 3.7 nm alloyed particles at various stages of ion exchange are shown in Figure 1A. The original ZnSe particles show a well-defined absorption maximum at 402 nm. The exciton energy of ZnSe QDs varies with size in a known manner[12] and establishes the ZnSe particle diameter as 3.7 nm. The absorption spectra shift to the red as zinc to cadmium ion exchange occurs, and the extent of ion exchange is determined by the magnitudes of the shift. We also note that due to the difference in lattice parameter, the particle diameters increase from 3.7 to 3.9 nm as ion exchange occurs. The exciton energy (in eV) varies with composition in a nonlinear fashion – there is a finite amount of optical band-bowing in these alloys. For the case of ZnSe and CdSe alloys, the band-bowing parameter is about 0.49 eV and the bandgap energy as function of composition is given by[13]

$$E_g(Zn_{1-x}Cd_xSe) = x\,E_g(CdSe) + (1-x)\,E_g(ZnSe) - 0.49\,x\,(1-x) \qquad \text{E3.1}$$

where $E_g(ZnSe)$ and $E_g(CdSe)$ are the pure ZnSe and CdSe exciton energies. For 3.7 nm particles, these values are taken to be $E_g(ZnSe) = 3.08$ eV and $E_g(CdSe) = 2.14$ eV. These spectra are very similar to those in reference 4, indicating that the ion exchange process reproduces.

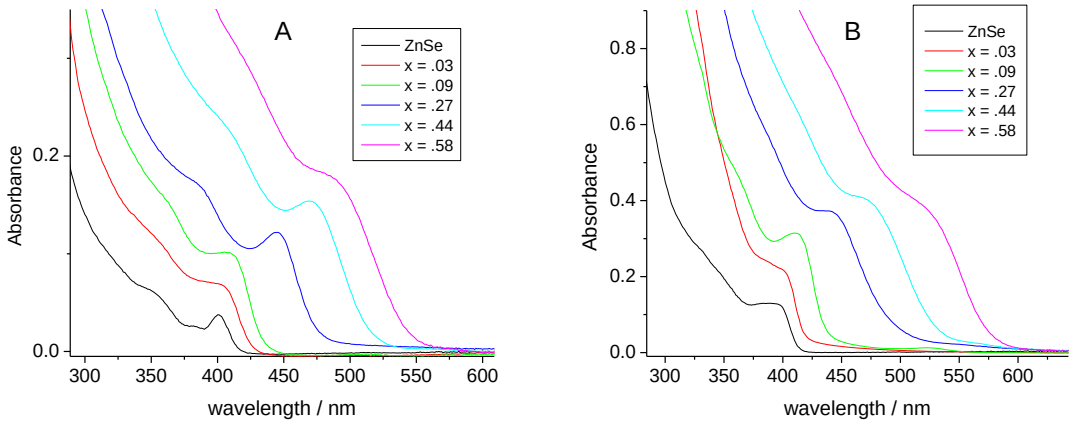

Figure 3.1 (A) Scaled absorption spectra of 3.7 nm $Zn_{1-x}Cd_xSe$ particles. (B) Scaled absorption spectra of 3.7 nm $Zn_{1-x}Cd_xSe$/ZnS core/shell particles. The cadmium mole fractions, x, corresponding to the different spectra are also indicated.

Following alloying by ion exchange, a thin ZnS shell is deposited onto the alloyed core particles. This shell is applied at a very low temperature (140 °C) to avoid having further ion exchange or diffusion change the composition or radial composition profile. Deposition of a thin ZnS shell shifts the spectra slightly to the red as shown in figure 1B. This is particularly true for spectra of the particles having greater concentrations of cadmium. This occurs for a combination of two reasons. Some of the shift is due to penetration of the (primarily electron) wavefunction into the ZnS shell, reducing the amount of quantum confinement. However, for the most exchanged particles (x = 0.58) this shift is close to 30 nm, which is too large to be explained by wavefunction delocalization into the ZnS. We conclude that some of the red shift comes from the reaction of residual cadmium adsorbed on the particles that comes through the purification process. This cadmium reacts with the sulfur atoms from the DDTC, forming a sub-monolayer shell of CdS between the CdSe core and the ZnS shell.

The composition of an alloy QD can be determined from the wavelength of the exciton maximum in absorption spectra using equation 3.1. Figure 3.1 shows that some of the spectra are sufficiently broadened by exchange inhomogeneity that the exciton maxima are not well-defined, which makes determination of the average extent of exchange somewhat uncertain. However, all of the transient absorption spectra have very well-defined bleach maxima. In cases where the static absorption spectra have well-defined maxima, the bleach maxima closely correspond to the same wavelength. To avoid ambiguities resulting from inhomogeneous broadening, the spectral positions of the bleach features in the transient absorption spectra are used to determine the particle compositions. The values of x shown in figure 3.1 were determined in this way.

3.2.1 Alloy biexciton TA kinetics

Throughout the present studies, all transient absorption (TA) kinetics were obtained on particles having a thin shell of either ZnS or CdS. An example of the power-dependent TA results on 3.7 nm ZnSe particles having a 1 monolayer CdS shell are shown in figure 3.2.

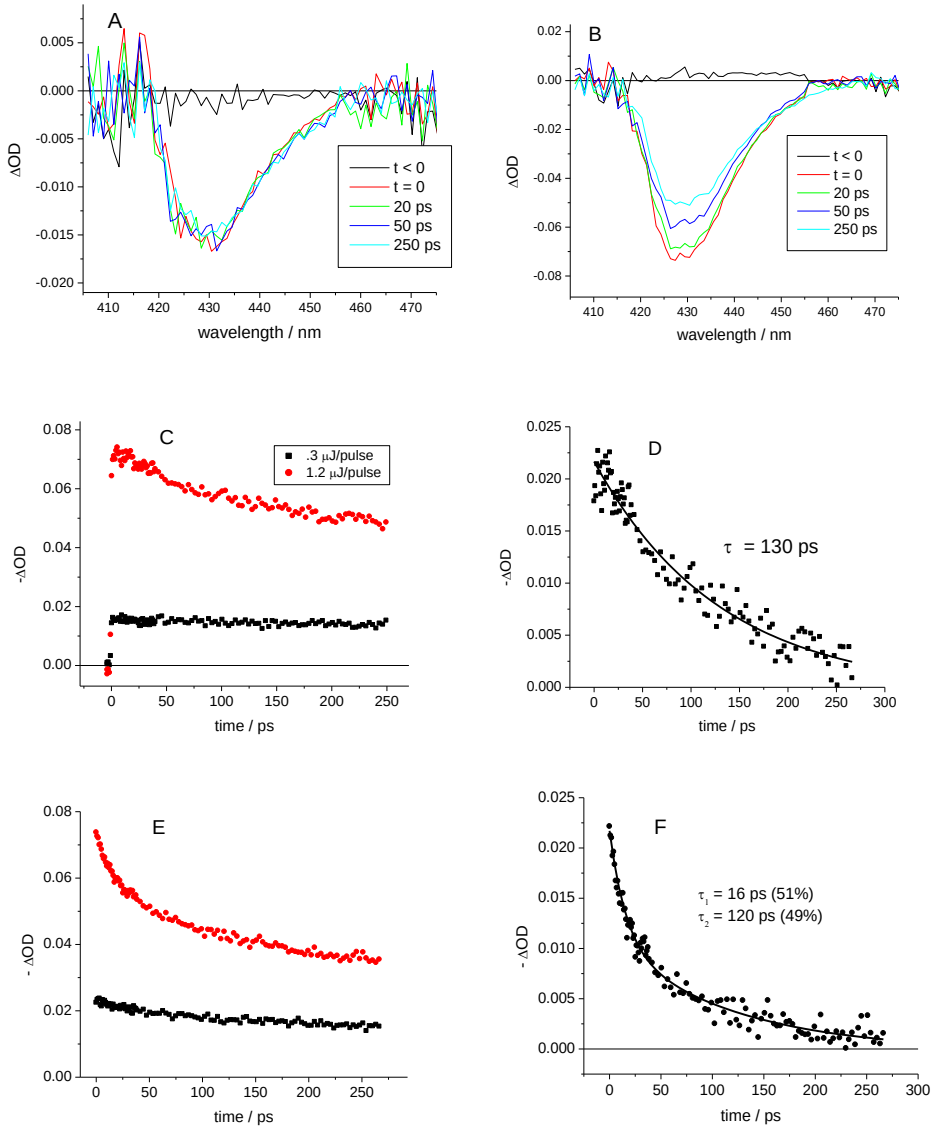

Figure 3.2. Representative TA results for pure 3.7 nm ZnSe/CdS measured at excitation fluences of (A) 0.3 μJ/pulse and (B) 1.2 μJ/pulse. (C) The power dependent 1S-1S exciton bleach kinetics, and (D) the biexciton decay. E and F are analogous to C and D, except with alloyed particles having a composition of $Zn_{0.82}Cd_{0.18}Se$/CdS. Panels D and F also show fitted decay curves having the indicated time constants. Pure CdSe/CdS of this size gives a biexciton decay of about 120 ps.

Figure 3.2A shows that the low power TA spectra bleach exhibit a well-defined maximum at about 430 nm. Figure 2B shows very similar higher power TA spectra, having a larger magnitude bleach and a maximum observed at a similar wavelength. The presence of the CdS shell delocalizes the conduction band electron, reducing the extent of quantum confinement. The shell is quite thin (about 1 monolayer) so this shifts the ZnSe absorption maximum about 30 nm (0.20 eV) to the red. The power-dependent kinetics at the bleach maximum are shown in figure 2C. After growth of the CdS shell, these particles don't show any significant fast component in the low power kinetics, indicating that no fast electron trapping is occurring. Without the passivating shell, a significant fraction of the bleach decays on the timescale characteristic of Auger processes and makes extraction of the biexciton times difficult. This is why the potentially more complicated core-shell particles are studied rather than just the cores.

Biexciton kinetics are obtained from a comparison of the low and high power bleach recovery kinetics. Specifically, the kinetics associated with absorption of two photons can be obtained from the difference between the high and low power results, where the low power results are scaled to match the high power decays at long times. Assigning the difference between the high power and scaled low power decays to the biexciton dynamics assumes that two-photon excitation relaxes to the same states as are produced by one photon absorption, which is a perfectly valid assumption.[14] The biexciton kinetics extracted using this procedure are shown in figure 3D, along with the fit to a 130 ps single exponential decay. This decay time is similar to what is measured for biexciton decays in comparably sized CdSe QDs. Analogous TA results have been obtained for the alloyed QDs, as shown in figure 2E and 2F. In this case, the particle core composition corresponds to x = 0.18 and the particles have a comparable, one monolayer CdS shell. The low power bleach decay kinetics (figure 2E, black symbols) are relatively flat on this time scale, having only a small amplitude decay component of approximately 100 ps. The biexciton kinetics (figure 3F) show a strongly nonexponential decay. These kinetics can be adequately fit to a biexponential decay having 16 ps and 120 ps decay components with approximately equal amplitudes. Due to the limited range of the kinetic scans, there is considerable uncertainty in time constant of the slow component. Comparable results are obtained with particles having a larger (4.5 nm diameter) core and a comparable one monolayer CdS shell. In this case the biexciton Auger times are all about a factor of two larger than obtained from the 3.7 nm particles, as would be expected for volume scaling. A comparison of the biexciton Auger kinetics as a function of composition for the 3.7 and 4.5 nm particles is shown in figure 3. The most remarkable aspect of these results is that the alloyed particles show a fast component of the biexciton decay that is absent in either pure ZnSe or pure CdSe. This component is almost an order of magnitude faster than the pure ZnSe decay and constitutes about 50% of the biexciton decay.

Somewhat more complicated results are obtained for ZnSe and alloyed QDs having a ZnS shell. The ZnS shell does not completely passivate the surface carrier traps and the low power TA results show a significant decay component (about 30% of the total) having a time constant of 10 – 20 ps. Despite this complication, biexciton decays can be obtained from the power dependent TA kinetics using the same procedure as outlined above. The pure materials and alloy results are also shown in figure 3.3. In the case of these 3.7 nm diameter ZnSe/ZnS (the x = 0 case) particles having the ZnS shell, the absorption bleach

is quite far to the blue (about 405 nm) which is close to the blue spectral limit of the TA apparatus, limiting the signal to noise ratio of these kinetics. Despite this difficulty, figure 3.3C shows that close to a single exponential decay is obtained for pure ZnSe/ZnS. The important result from the TA kinetics on the ZnS-coated particles is that the 10 – 40% cadmium alloy particles exhibit a biphasic decay with the short component being much shorter than either of the pure materials.

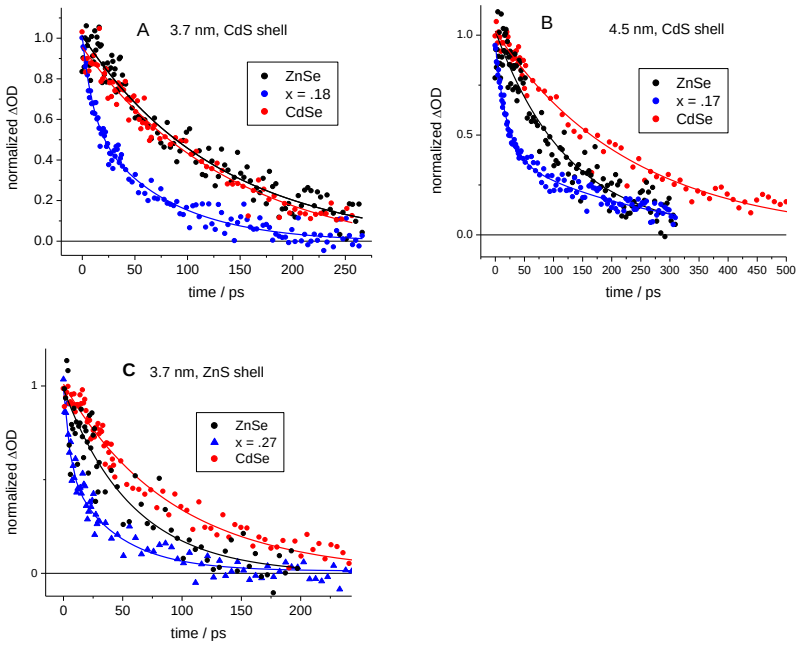

Figure 3.3. Normalized biexciton decays for (A) 3.7 nm and (B) 4.5 nm diameter alloyed particles passivated with a CdS shell, and (C) 3.7 nm particles passivated with ZnS. The pure ZnSe and CdSe decays are fit to single exponentials and the alloyed particles are fit to biexponentials.

The results in figure 3.3 show that in all cases the biexciton decays of the pure ZnSe and pure CdSe give close to single exponential decays, with a time constant on the order of 100 ps. The biexciton kinetics of the alloys are more complicated, showing strongly nonexponential decays. This is independent of particle size or whether the particle has a CdS or ZnS shell. The pure ZnSe and CdSe decay times and the fast component of the alloy decays are summarized in Figure 3.4.

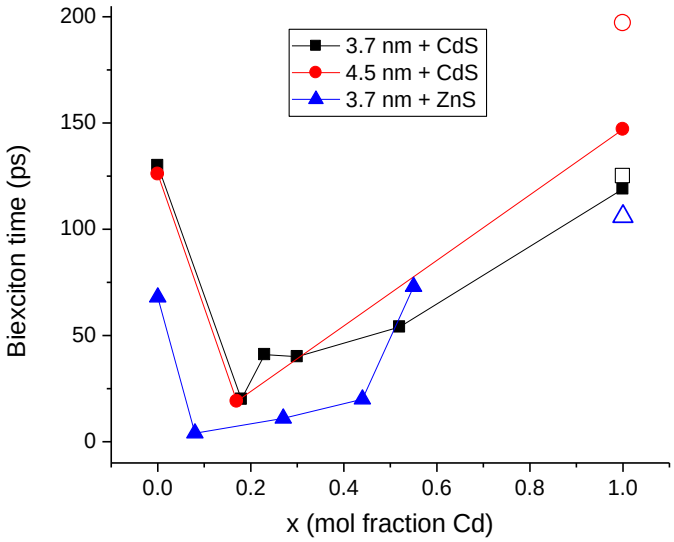

Figure 3.4. Fast decay component times for three different types of alloy QDs as a function of composition. Closed symbols: ZnSe and cation exchanged particles. Open symbols: pure CdSe with a CdS or ZnS shell.

In all cases the fast component decay time goes through a minimum at a composition of about 10% to 40% cadmium. At this minimum, the amplitudes of the fast and slow components are roughly equal. At cadmium fractions greater than 40%, the alloy decays can be fit to a single exponential having a decay time that is significantly faster than the Auger times of pure ZnSe or CdSe, as shown in figure 3.4.The results presented above may be summarized as a few simple observations:

1. The biexciton kinetics of pure ZnSe or CdSe follow single exponential decays with time constants on the order of 100 ps.
2. Biexciton Auger times of the alloyed particles do not change smoothly with composition. The decay times show a distinct minimum at x = 0.1 – 0.4 that is independent of particle size. These kinetics show biphasic decays with slow components that are comparable to, or slightly faster than the pure materials and fast components that are about an order of magnitude faster. The fast and slow components have approximately equal amplitudes.
3. The biexciton kinetics of alloyed particles having compositions greater than 40% cadmium exhibit decays that can be fit to single exponentials having time constants that are longer than the fast components at x = 1.0 – 0.4, but significantly shorter than the decay times of pure ZnSe or CdSe.

The biexciton decay kinetics of pure ZnSe and CdSe QDs are straightforward. To the best of our knowledge, biexciton Auger times in ZnSe QDs have not previously been reported. However, based on the similarity with CdSe (similar effective masses, dielectric constants, etc.), one would not expect that Auger recombination times would be vastly different, and indeed, we see a ZnSe Auger decay time that is comparable, or at most a

factor of two faster. The Auger times obtained following complete ion exchange are consistent with core/shell QDs, obtained from comparably-sized pure zincblende CdSe cores. The biexciton decay rates in these QDs approximately follow volume scaling and previously reported size-dependent CdSe Auger times.[15, 16]

We suggest that the faster and nonexponential decays observed for the alloyed QDs can be understood in terms of a few simple considerations. The key idea is that these are random, rather than uniform alloys. If a small fraction, say 20%, of the zinc atoms are randomly replaced with cadmiums, then there will be regions in each of the particles where the cadmium concentrations are locally higher or lower than the average. Due to the valence band offset and band-bowing effects, the regions of higher cadmium concentrations will have a lower energy valence band. These spatial variations of the valence band energy result in partial localization of the holes, and the extent of hole localization is crucial in determining the biexciton Auger rate. This is because localization of the hole wavefunctions increases the gradient of the hole wavefunction, and large gradients result in large high-momentum components.

The observed trend in Auger times is similar to what is observed for the electron-phonon couplings in alloyed particles, and we suggest this occurs for what is essentially the same reason. In a previous paper, we found that $Zn_{1-x}Cd_xSe$ alloys[4] gave much larger electron phonon couplings (EPCs) than either pure ZnSe[5] or pure CdSe.[17-19] EPC occurs through a Fröhlich mechanism, whereby the optical phonons of a polar crystal are excited by the electric field produced by differential overlap of the electron and hole wavefunctions.[20] Random concentration variations cause spatial variations in both the valence and conduction bands. However, due to the much smaller effective mass of the electron,[21] much less electron localization occurs. The overall result is that the internal electric field is dominated by spatial variations in the valence band potential causing partial hole localization. This greatly increases the spatial differences between the electron and hole wavefunctions and therefore increases the magnitude of the electric field of the exciton, increasing the EPC. The same spatial variations and partial hole localization produce high momentum components of the hole wavefunction, increasing the biexciton Auger rate.

3.2.3 Calculation of hole density gradients as a function of composition

The above qualitative statements can be made more quantitative through hole wavefunction calculations that consider the alloy energetics. The ZnSe and CdSe valence bands are not much different in energy, 6.22 and 6.0 eV below the vacuum level, respectively.[13] However, neither the band gap nor the valence band energy varies linearly with composition, i.e., $Zn_{1-x}Cd_xSe$ alloys exhibit optical band bowing.[13, 22-24] Optical band bowing is typically characterized by a single parameter (as in equation 1) that gives the band gap as a function of composition. Some of this composition dependence is in the conduction band and some in the valence band. Calculations indicate that in the case of $Zn_{1-x}Cd_xSe$ alloys most of the variation is in the conduction band, but a significant amount

is also in the valence band.[13] These calculations indicate that the valance band energy can be characterized by a band-bowing parameter of about 0.14 eV, as depicted in figure 3.5.

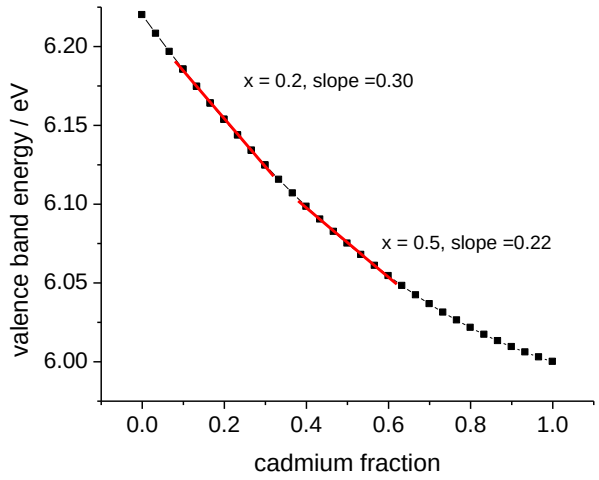

Figure 3.5. Valence band energy as a function of composition for bulk $Zn_{1-x}Cd_xSe$. The CdSe and ZnSe valence band energies are taken to be 6.0 and 6.22 eV, respectively, and the value of the valence band bowing parameter is taken to be 0.14, following ref. 13. The slopes of the curve at x = 0.20 and x = 0.50 are also indicated as red lines.

Because the quantum confinement energy for holes in QDs is rather small, we assume that the same curve can be applied to QDs with an overall shift of the energy axis. The derivative of the valence band energy versus composition curve can be shown to be approximately equal to the difference in valence band potential energy between cadmium and zinc atoms, giving 0.30 eV at 20% Cd and 0.22 eV at 50% Cd. These were the values employed in our calculations of valence band potentials in QDs. We note that these values do not give the correct absolute values of the valence band energies, but they properly capture the change in valence band energy with composition at a particular composition, and that is what matters for determining the spatial extent of the hole wavefunction.

Using these energetics, the alloyed hole wavefunctions can be calculated by either of two approaches. The simplest approach uses a random number generator to assign the positions of the cadmium and zinc atoms and first order perturbation theory to calculate the wavefunction. This calculation is done as follows. We start by constructing a 3.3 nm diameter sphere (r_0 = 1.65 nm) containing about 400 atoms by cutting this out from a face-centered-cubic lattice having the ZnSe lattice parameter. This corresponds to the metal atom positions in the QD. CdSe has a somewhat larger (about 7%) lattice parameter than ZnSe, and the alloy lattice parameter is taken to vary linearly with composition. In the absence of cadmium atoms and neglecting electron-hole interaction, the hole wavefunctions are given by the particle-in-a-sphere wavefunctions, $\Psi_{nlm} = j_l(\alpha_{l,n} r / r_0) Y_l^m(\theta,\varphi)$, where j_l is the *l'th* spherical Bessel function having its *n'th* root at $\alpha_{l,n}$, $Y_l^m(\theta,\varphi)$ is a spherical harmonic and r_0 is the particle radius. The ground

wavefunction is the 1S function, $\Psi_{100} = j_0(\alpha_{0,1} r / r_0) Y_0^0(\theta, \varphi)$. The energies of these states are given by $E_{n,l} = \frac{\hbar^2 \alpha_{l,n}^2}{2 m_{eff} r_0^2}$ where the hole effective mass is taken to be $m_{eff} = 2.9 m_e$, the value found to best reproduce the optical spectra of CdSe in a two-band model.[25]

For a 20% cadmium alloy, 20% of the lattice points are chosen at random and assigned an energy of 0.30 eV and the remaining points are assigned an energy of zero. This gives the discretized alloy potential, *V(x,y,z)*, which is treated as a first-order perturbation that mixes the 1S state with the 2S and 1P states. The final state is given by the first order perturbation expression, where the coupling is calculated numerically over the grid of the 400 lattice points. The calculated hole wavefunctions are then written as the initial 1S wavefunction plus the sum of four additional terms:

$$\Psi = \Psi_{1S} + \frac{\langle \Psi_{1S} | V | \Psi_{1Px} \rangle}{E_{1P} - E_{1S}} \Psi_{1Px} + \frac{\langle \Psi_{1S} | V | \Psi_{1Py} \rangle}{E_{1P} - E_{1S}} \Psi_{1Py} + \frac{\langle \Psi_{1S} | V | \Psi_{1Pz} \rangle}{E_{1P} - E_{1S}} \Psi_{1Pz} + \frac{\langle \Psi_{1S} | V | \Psi_{2S} \rangle}{E_{2S} - E_{1S}} \Psi_{2S} \quad \text{E3.2}$$

The first-order corrected function can be differentiated to give the spatially dependent gradient. Maximum gradients obtained in this way for several 20% and 50% alloys are plotted as a function of composition in figure 3.6.

An alternative and somewhat more realistic approach to this problem is as follows. We begin by constructing a ZnSe zincblende crystal and cutting out a 3.3 nm diameter QD containing 798 atoms ($Zn_{399}Se_{399}$). Approximately 20% or 50% of the zinc atoms are randomly replaced by cadmium using a random number generator. We have calculated twelve different structures with 17-23% Cd and twelve structures with 46-54% Cd. The geometry of each structure is then energetically minimized using the GULP program and the force field described in reference 4. The valence band potential energy is assumed to vary with position as the weighted average of the four nearest cations, thus making the potential energy lower in Cd-rich regions of the structure than in Zn-rich regions. As before, the kinetic energy is taken as that of a hard-walled particle in a sphere with radius equal to the radius of the QD and the hole effective mass is taken to be $m_h = 2.9 m_e$. The hole wavefunctions are calculated by diagonalizing the Hamiltonian in a basis of the particle in a sphere wavefunctions (spherical harmonics up to $l = 4$ multiplied by the spherical Bessel functions for $n = 0$ to 2, a total of 75 basis functions). The gradients are then calculated numerically on a sufficiently small grid such that reduction of the grid volume elements does not change the calculated results. The calculated maximum spatial gradient of the hole wavefunction for ~ 3.3 nm diameter QDs that are approximately 20% Cd, 50% Cd, and pure ZnSe are shown in Figure 3.6.

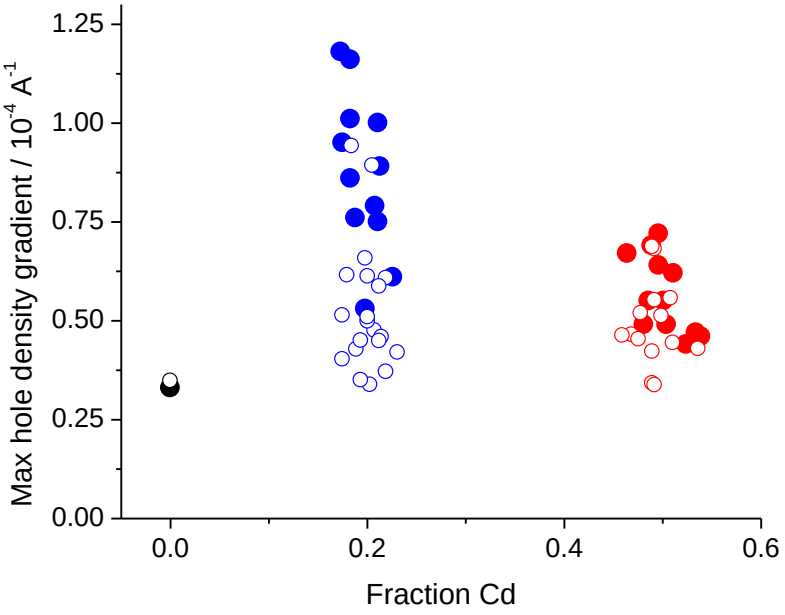

Figure 3.6. Calculated maximum hole density gradients as a function of cadmium mole fraction in 3.3 nm QD random alloys. Points calculated from the perturbation and variational methods are shown as open and solid dots, respectively.

The two calculational approaches show very similar results. A larger gradient indicates more rapidly varying components of the hole wavefunction, which we associate with higher momentum components and a faster Auger recombination rate. Both 20% and 50% alloyed QDs show generally larger maximum gradients than the single-component QDs, and the gradients are generally larger for the 20% Cd structures than for the 50% ones. It is important to note that there is also a rather large spread in maximum gradient among structures having roughly the same composition. This is due to the random (rather than uniform) nature of the alloy and directly manifests as inhomogeneity in the decay rates. We note that the perturbation calculation shows somewhat smaller gradients than the variational calculation. There are two principal differences between the two calculational approaches. First, the variational approach optimizes the local geometry, rather than taking the entire lattice to vary uniformly with composition. In terms of calculating a wavefunction gradient, this is expected to be a small effect. Second, the variational approach uses a larger basis set for expansion of the final wavefunction. The terms having larger values of n and l vary more rapidly with position, thus giving somewhat larger gradients.

The results in Figure 3.6 are consistent with the experimental observation of the alloys having a range of biexciton recombination times, with the fastest times in the alloys about an order of magnitude greater than in either pure CdSe or pure ZnSe. These calculations are also consistent with somewhat faster recombination in 20% compared to 50% alloys.

In addition, we note that the dispersion of gradients for x = 0.2 is considerably larger than with x = 0.5. This is also consistent with our experimental results in which the x = 0.5 – 0.6 decays are fit with a single exponential, whereas the x = 0.10 – 0.40 results in all cases must be fit to a biexponential.

Figures 3.7 and 3.8 show color-coded representations of the hole density in each atom for a pure QDs and for six of the structures with approximately 20% Cd, as calculated by the variational method described above. These plots clearly show the loss of spherical symmetry of the hole function in the alloys because of the random fluctuations in the regions of lowest potential energy.

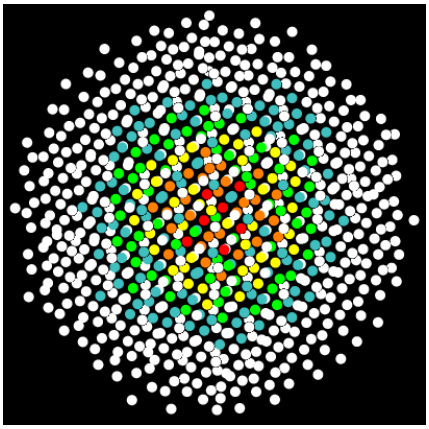

Figure 3.7 Color-coded hole densities on each of the atoms (white, cyan, green, yellow, orange, red representing increasingly high hole density) for a pure CdSe QDs.

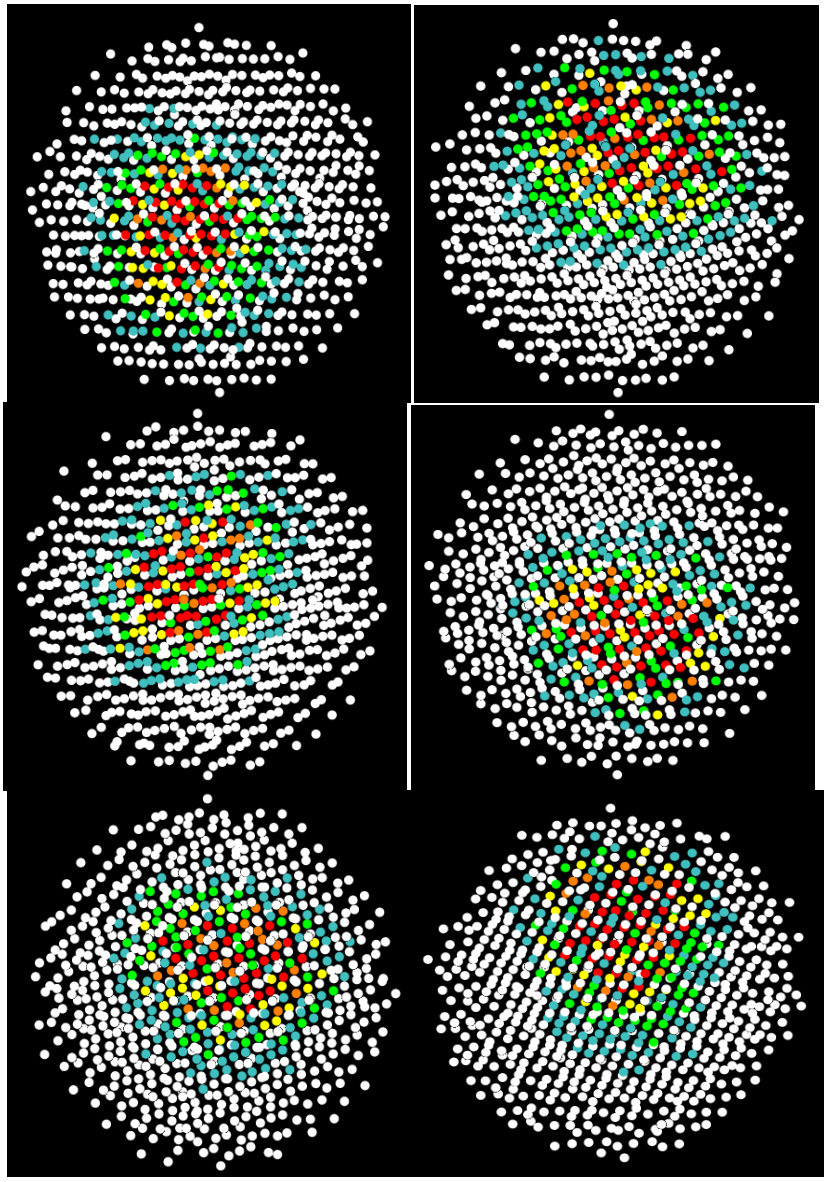

Figure 3.8 Same as Figure 3.7 for six QDs of approximate composition $Cd_{0.2}Zn_{0.8}Se$.

These figures also show that inhomogeneities in the valence band potential cause relatively small distortions in the hole wavefunction. This is consistent with simple calculations of the spatial variations of the valence band potential. For the case of x = 0.20, the variation of the valence band potential from one part of the particle to another is on the order of 20 meV, which seems like a very small energy. However, an interesting perspective results from the comparison of the energies and wavefunctions calculated above with those of a particle in a dipolar electric field. The wavefunction distortions created from valence band inhomogenieties are comparable to those that would be caused by putting the particle in a rather large external electric field, on the order of 10^7 V/m.

The calculation of the electric field that is equivalent to the valence band potential gradient allows us to comment on the magnitude of electric fields associated with charged ligands adsorbed on the particle surface. An equal dipolar component of the internal electric field would be created by adsorbing an uncompensated charge of 0.1 of an electron charge on the surface of the particle.[26] This result suggests that if the charge were uncompensated, adsorption of charged surface ligands (such as an alkylcarboxylate) would dramatically change much of the particle photophysics, especially dynamic quantities such as EPCs and Auger rates. However, this is not observed – Auger rates and measured EPCs are essentially independent of the nature of the surface ligands.[27] The conclusion is that QDs do not have uncompensated charged ligands on the surfaces. When charged ligands are attached to the particles in nonpolar solution, they are almost completely charge compensated by adsorption of counter ions. Thus, relatively small potential variations introduced by compositional variations of alloys can introduce sufficient valence band potential gradients to dramatically affect the QD photophysics.

3.3 Conclusions

The biexciton Auger dynamics of pure ZnSe and CdSe QDs follow single exponential kinetics, with decay times for both on the order of 100 ps for particles ~ 3.7 nm in diameter. $Zn_{(1-x)}Cd_xSe$ alloyed QDs show more complicated decay kinetics, having slow and fast components of approximately equal amplitudes. The slow components have about the same decay times as the pure materials, while the fast components are about an order of magnitude faster. The amplitude and rate of the fast component go through a maximum around alloy compositions $x = 0.15$. This behavior is attributed to random, rather than uniform, alloying in the early stages of the exchange reaction. Random alloying is characterized by large local variations in the composition profiles, and because of the valence band offset and band-bowing effects, the holes are partially localized in the regions of higher cadmium concentration. This partial hole localization facilitates faster Auger kinetics. Both the increase in Auger rates and the biphasic decays at small x are semi-quantitatively reproduced by taking the composition-dependent VB energy as a first-order perturbation to the spherically symmetric Hamiltonian.

Ch 3 References

1. Klimov, V. I.; McGuire, J. A.; Schaller, R. D.; Rupasov, V. I., Scaling of multiexciton lifetimes in semiconductor nanocrystals. *Phys. Rev. B* **2008,** *77*, 195324 - 195324.
2. Beane, G. A.; Gong, K.; Kelley, D. F., Auger and Carrier Trapping Dynamics in Core/Shell Quantum Dots Having Sharp and Alloyed Interfaces. *ACS Nano* **2016,** *10*, 3755-3765.
3. Avidan, A.; Oron, D., Large Blue Shift of the Biexciton State in Tellurium Doped CdSe Colloidal Quantum Dots. *Nano Lett.* **2008,** *8*, 2384-2387.
4. Gong, K.; Kelley, D. F.; Kelley, A. M., Nonuniform Excitonic Charge Distribution Enhances Exciton–Phonon Coupling in ZnSe/CdSe Alloyed Quantum Dots. *J. Phys. Chem. Lett.* **2017,** *8*, 626-630.
5. Gong, K.; Kelley, D. F.; Kelley, A. M., Resonance Raman Spectroscopy and Electron–Phonon Coupling in Zinc Selenide Quantum Dots. *J. Phys. Chem. C* **2016,** *120*, 29533-29539.
6. Cragg, G. E.; Efros, A. L., Suppression of Auger Processes in Confined Structures. *Nano Lett.* **2010,** *10*, 313.
7. Climente, J. I.; Movilla, J. L.; Planelles, J., Auger Recombination Suppression in Nanocrystals with Asymmetric Electron-Hole Confinement. *Small* **2012,** *8*, 754-759.
8. Vaxenburg, R.; Rodina, A.; Shabaev, A.; Lifshitz, E.; Efros, A. L., Nonradiative Auger Recombination in Semiconductor Nanocrystals. *Nano Letters* **2015,** *15*, 2092-2098.
9. Pu, C.; Zhou, J.; Lai, R.; Niu, Y.; Nan, W.; Peng, X., Highly Reactive, Flexible Yet Green Se Precursor for Metal Selenide Nanocrystals: Se-Octadecene Suspension (Se-SUS). *Nano Research* **2013,** *6*, 652-670.
10. Groeneveld, E.; Witteman, L.; Lefferts, M.; Ke, X.; Bals, S.; Tendeloo, G. V.; Donega, C. d. M., Tailoring ZnSe-CdSe Colloidal Quantum Dots via Cation Exchange: From Core/Shell to Alloy Nanocrystals. *ACS Nano* **2013,** *7*, 7913.
11. Nan, W.; Niu, Y.; Qin, H.; Cui, F.; Yang, Y.; Lai, R.; Lin, W.; Peng, X., Crystal Structure Control of Zinc-Blende CdSe/CdS Core/Shell Nanocrystals: Synthesis and Structure-Dependent Optical Properties. *J. Am. Chem. Soc.* **2012,** *134*, 19685−19693.
12. Eilers, J.; van Hest, J.; Meijerink, A.; Donega, C. d. M., Unravelling the Size and Temperature Dependence of Exciton Lifetimes in Colloidal ZnSe Quantum Dots. *J. Phys. Chem. C* **2014,** *118*, 23313-23319.
13. Mourad, D.; Czycholl, G.; Kruse, C.; Klembt, S.; Retzlaff, R.; Hommel, D.; Gartner, M.; Anastasescu, M., Band gap bowing of binary alloys: Experimental results compared to theoretical tight-binding supercell calculations for CdxZn1−xSe. *Phys. Rev. B* **2010,** *82*, 165204.
14. Klimov, V. I.; Mikhailovsky, A. A.; McBranch, D. W.; Leatherdale, C. A.; Bawendi, M. G., Quantization of Multiparticle Auger Rates in Semiconductor Quantum Dots. *Science* **2000,** *287*, 1011-1013.
15. Robel, I.; Gresback, R.; Kortshagen, U.; Schaller, R. D.; Klimov, V. I., Universal Size-Dependent Trend in Auger Recombination in Direct-Gap and Indirect-Gap Semiconductor Nanocrystals. *Phys. Rev. Lett.* **2009,** *102*, 177404-177407.

16. Gong, K.; Kelley, D. F., Surface Charging and Trion Dynamics in CdSe-Based Core/Shell Quantum Dots. *J. Phys. Chem. C* **2015,** *119*, 9637-9645.
17. Lin, C.; Gong, K.; Kelley, D. F.; Kelley, A. M., Size-Dependent Exciton-Phonon Coupling in CdSe Nanocrystals through Resonance Raman Excitation Profile Analysis. *J. Phys. Chem. C* **2015,** *119*, 7491-7498.
18. Lin, C.; Gong, K.; Kelley, D. F.; Kelley, A. M., Electron–Phonon Coupling in CdSe/CdS Core/Shell Quantum Dots. *ACS Nano* **2015,** *9*, 8131-8141.
19. Kelley, A. M.; Dai, Q.; Jiang, Z.-J. B., J. A.; Kelley, D. F., Resonance Raman spectra of wurtzite and zincblende CdSe nanocrystals. *Chem. Phys.* **2013,** *422*, 272-276.
20. Yu, P. Y.; Cardona, M., *Fundamentals of Semiconductors*. third ed.; Springer: Berlin, 2001.
21. Rogach, A. L.; Kornowski, A.; Gao, M.; Eychmuller, A.; Weller, H., Synthesis and Characterization of a Size Series of Extremely Small Thiol-Stabilized CdSe Nanocrystals. *J. Phys. Chem. B* **1999,** *103*, 3065 - 3069.
22. West, A. R., *Basic Solid State Chemistry*. Wiley Chichester, 1988.
23. Mourad, D.; Czycholl, G., Theory of band gap bowing of disordered substitutional II–VI and III–V semiconductor alloys. *The European Physical Journal B* **2012,** *85*, 153.
24. Mourad, D.; Czycholl, G., Multiband tight-binding theory of disordered A x B1- x C semiconductor quantum dots. *The European Physical Journal B* **2010,** *78*, 497-507.
25. Lin, C.; Kelley, D. F.; Rico, M.; Kelley, A. M., The "Surface Optical" Phonon in CdSe Nanocrystals. *ACS Nano* **2014,** *9*, 3928-3938.
26. Bottcher, C. J. F., *Theory of Electric Polarization*. Elsevier: Amsterdam, 1973; Vol. 1.
27. Baker, J. A.; Kelley, D. F.; Kelley, A. M., Resonance Raman and photoluminescence excitation profiles and excited-state dynamics in CdSe nanocrystals. *J. Chem. Phys.* **2013,** *139*, 024702.

Ch. 4

The Role of Surface States in Silver-Doped CdSe and CdSe/CdS Quantum Dots

Abstract

The effects of Ag doping of CdSe and CdSe/CdS quantum dots (QDs) have been studied as a function of the surface composition. Throughout these studies, static and time-resolved luminescence and transient absorption measurements are used to determine the nature and rates of radiationless decay mechanisms and how these vary with the concentration of Ag dopants. In TBP-ligated CdSe, the PLQY varies non-monotonically with dopant concentration, increasing at low concentrations of Ag^+ then decreasing with further addition. The initial increase is assigned to the passivation of pre-existing surface hole traps by interaction of interstitial Ag^+ with surface Se^{2-} ions, while the subsequent decrease is due to the introduction of substitutional Ag^+, which act as a new source of hole traps. Ligation of the particle surface with alkyl amines largely passivates the surface hole traps and eliminates the initial increase in PL QY upon doping. CdSe/CdS QDs ligated with oleylamine (and no phosphines) exhibit extensive thermal population of empty surface orbitals by valence band electrons. Photoexcitation of these surface charged particles results in what is essentially a positive trion, which can undergo rapid Auger decay. The presence of oleylamine reduces much of the Ag^+ to Ag^0, and the addition of Ag^0 dopants passivates these empty surface states and eliminates the surface charging and hence positive trion formation.

4. 1 Introduction

The intentional introduction of impurities into semiconductor nanocrystals has been a long-desired goal, with the intent of altering and controlling important optical and electrical properties of the particles.[1] An impurity having one more valence electron than the atom it replaces can be ionized, donating the extra electron to the conduction band (n-type doping). Similarly, an impurity with one fewer valence electron can accept an electron from the valence band, leaving a valence band hole (p-type doping). These electrons or holes can be charge carriers or can participate in radiative or nonradiative charge recombination. There is considerable literature on doping II-VI semiconductor quantum dots (QDs), with the most common dopants being Mn and Cu. Mn is isovalent with Zn or Cd and gives dopant-centered yellow photoluminescence (PL).[2] Copper is typically added as Cu^+ and these ions go in substitutionally for Zn or Cd.[3] For example, it has long been known that silver and copper dopants in ZnS give impurity-centered blue and green luminescence, respectively, and have been extensively used in displays.[4]

Whether impurity atoms can be introduced into the host crystal lattice depends on the thermodynamics of the host-guest interaction and in some cases the kinetics of doped crystal growth.[2] In particular, inclusion into the host crystal must be thermodynamically favorable and the impurity absorption and crystal growth kinetics must facilitate incorporation of the impurity into the growing crystals. In some cases, the impurity atoms

readily diffuse into the host crystal and continued addition results in a complete exchange of the original lattice.[5, 6] This ion exchange process is often most facile at elevated temperatures and can have significant consequences on the nanoparticle photophysics.[7,39,44] Silver can also readily exchange for cadmium in room temperature CdSe, forming Ag_2Se.[5] It is therefore very easy to form silver-doped CdSe QDs by low-temperature ion exchange.

Several previous studies have examined the spectroscopic and photophysical effects of doping silver into CdSe QDs. In an important early paper, the PL quantum yield (QY) was reported to increase with silver-doping up to about two atoms per QD, while higher doping concentrations resulted in a decrease of the QY.[7] These results were interpreted in terms of a model in which the initial silvers went in interstitially and behaved as n-type dopants, whereas subsequent silvers went in substitutionally and behaved as p-type dopants. Subsequent EXAFS results also indicate that the initial silvers are in interstitial lattice sites.[8] EPR studies performed on undoped and Ag-doped CdSe QDs showed long-lived EPR signals that were interpreted in terms of internal selenium atom vacancies.[9] These studies concluded that the presence of Ag dopants can affect the Fermi level of the particle and thereby alter the magnetic and optical properties. More recently, experimental photoluminescence and magneto-photoluminescence studies have recently been performed and interpreted with the aid of time dependent density functional theory (TD-DFT) calculations.[3] The results are interpreted in terms of Ag^+ substituting for Cd in the CdSe lattice. Previous CdSe doping studies have largely ignored the interactions of the Ag dopants with surface states. However, a 3.1 nm CdSe QD has approximately half of the interstitial lattice holes within one unit cell of the surface, and one may therefore expect that surface states will play a significant role in the spectroscopy and photophysics of both pure and doped QDs.

Due to the small particle volume, the discrete nature of the energy levels and the small density of states at the band edge, introducing a single charge into a QD can have large effects on the spectroscopy and dynamics. Addition of an electron into the conduction band has consequences for both the static and dynamic spectra. Photogeneration of the lowest exciton involves a transition to the non-degenerate $1S_e$ conduction band level. The presence of a single electron in this state will result in the transition being bleached by a factor of one-half. Furthermore, one expects that the photoluminescence will be at least partially quenched by a negative trion Auger decay taking place on a timescale comparable to or faster than radiation.[10-12] Introducing a single hole into the valence band has a much smaller effect on the static absorption spectrum, which remains largely unchanged due to the degeneracy of the GS $\rightarrow$ X and $h^+ \rightarrow h^+X$ transitions, as described in Section 2.5. However, the photoluminescence will be quenched by a fast positive trion Auger decay.[13, 14] Addition of a single positive or negative charge can also change the redox state of surface orbitals. Orbitals in energetic proximity of the valence band are predominantly of selenium character and can be either empty or full. Full 3p or 4p orbitals of reduced surface sulfurs or seleniums can donate electrons to fill a valence band hole and thereby act as hole traps. Filling these orbitals to a very high energy from a sacrificial reducing agent in solution results in n-type photodoping.[11, 15] In this case, photoexcitation results in an electron-hole pair, and the hole can be filled by electron donation from a reducing agent in solution. This also leaves an electron in the conduction band – the particle is n-type.

Alternatively, ejection of a hot hole can also leave the QD negatively charged, with the extra electron in a surface state.[16, 17]

The nonradiative processes occurring after photoexcitation are controlled by the energies, densities, and oxidation states of mid-gap surface states. The nature of these states depends on ligation, surface stoichiometry,[18,19] exposure to atmosphere, and the redox properties of the reaction mixture. Surface orbitals near the valence or conduction bands have primarily chalcogenide or metal character, respectively. The extent to which these orbitals are filled defines the Fermi level. If the density of surface states is high and the Fermi level is more than a few kT above the valence band, then hole trapping results from the filled surface chalcogenide nonbonding orbitals ("dangling bonds") and often dominates the nonradiative processes. Hole traps can be diminished by either removal of the surface atom, direct passivation through an MO-theory type interaction between the trap state and a ligand,[19-22] or by shifting the band level relative to the trap state by using charge donating/accepting ligands to modify the electrostatic potentials.[45] Alternatively, if the Fermi level is within a few kT of the valence band, then valence band electrons can be thermally promoted to these surface orbitals. This leaves a hole in the valence band and the particle is essentially p-type. We have recently shown that p-type doping of CdSe nanoparticles can be achieved by adding excess Se to the particle surface, leading to a decrease in the luminescence quantum yields.[14, 23] Photoexcitation produces an electron-hole pair that couples to the steady state valence band hole and forms a positive trion. The trion can undergo fast Auger recombination, making it almost nonluminescent. The Auger process produces a hot hole which can undergo subsequent photochemistry.[16, 24] We refer to the excitation of valence band electrons to surface states as "surface charging" and find that it can take place in CdSe, CdSe/ZnSe and CdSe/CdS core/shell QDs.[16] The temperature dependence of this luminescence quenching is consistent with thermal promotion of valence band electrons to mid-gap states associated with unligated Se atoms.[23]

Filling states above the valence band edge raises the Fermi level and changes these dynamics. Initially, raising the Fermi level to more than a few kT above the valence band shuts off the surface charging and subsequent nonradiative Auger relaxation. Further raising the Fermi level can fill empty surface states, replacing surface charging/electron trapping with hole trapping. Appropriate species in solution with the QD can adsorb as surface ligands and interact with surface orbitals. Lewis acids and bases can interact with filled and empty surface states, lowering the energy of the bonding orbital and removing it from the band gap. In some cases, the ligands can also act as reducing or oxidizing agents, moving the Fermi level up or down. These are important considerations in describing the dynamics of silver-doped CdSe and CdSe/CdS core/shell nanoparticles. Addition of Ag^+ to a QD introduces an electron acceptor which can lower the Fermi level. In contrast, addition of Ag^0 introduces an electron donor, which can raise the Fermi level. As a result of these two contrasting effects, careful consideration of the Ag^+/Ag^0 redox state is necessary to interpret the results of any Ag doping experiment.

In this paper we examine the extent to which Ag dopants in different redox states can interact with surface states. We show that an Ag dopant of the appropriate oxidation state can affect the overall photoluminescence properties by either oxidizing or reducing surface states. Furthermore, because the particle stoichiometry and the nature of the surface ligands dictate both the presence and oxidation state of mid-gap surface states, it follows

that the effects of the dopant on particle quantum yields should change depending on the surface composition and ligation. We elucidate these effects with a combination of static and time-resolved PL spectroscopy and transient absorption (TA) spectroscopy.

4.2 Results and Discussion

4.2.1 CdSe QDs.

Absorption and PL spectra of zincblende Cd-rich CdSe as a function of dopant concentration are shown in Figure 4.1. These spectra correspond to QDs in which the doping solutions have an excess of tributylphosphine (TBP) and no alkylamine.

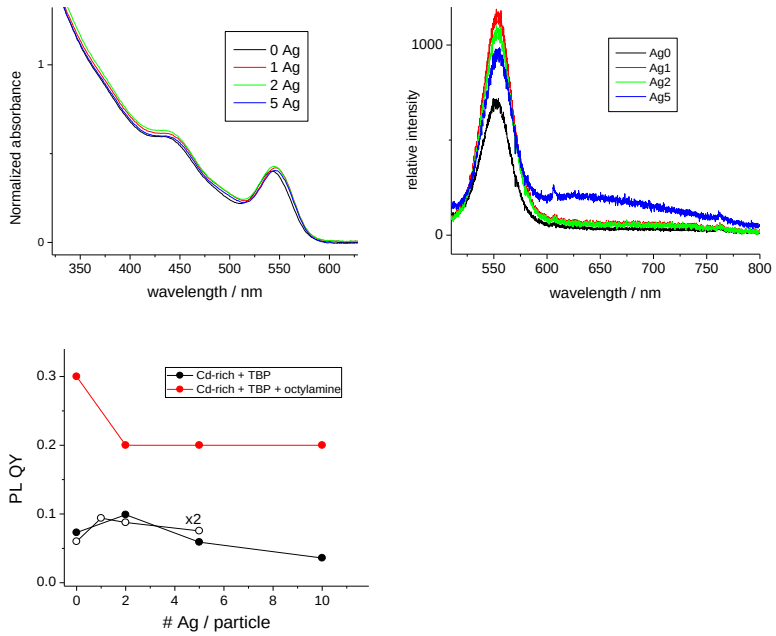

Figure 4.1. UV-vis absorption spectra (left) and PL spectra (center) of 3.1 ± 0.1 nm diameter ZB CdSe ligated with TBP at varying dopant concentrations. The photoluminescence spectra were excited at 450 nm. Right: PL quantum yields of the same particles as a function of dopant concentration and surface ligands. The solid and open black circles correspond to two different doping trials using the same particles.

At the low dopant concentrations used here, no effects are seen in the static absorption spectra or the wavelength maximum of the PL spectra. However, the PL QYs are sensitive to the dopant concentration, going through a maximum between 1 and 2 Ag per particle

depending on the batch, then decreasing as the dopant concentration gets larger. This is the same behavior as reported in [7]. The experiment was repeated with octylamine present in the reaction mixture, and the results of both summarized in Figure 4.1. We note that although there is some batch-to-batch variability in the QYs, the general trend is quite reproducible. The dopant concentration-dependent QYs can be understood when considered with the corresponding time-resolved PL and bleach recovery kinetics shown in Figure 4.2.

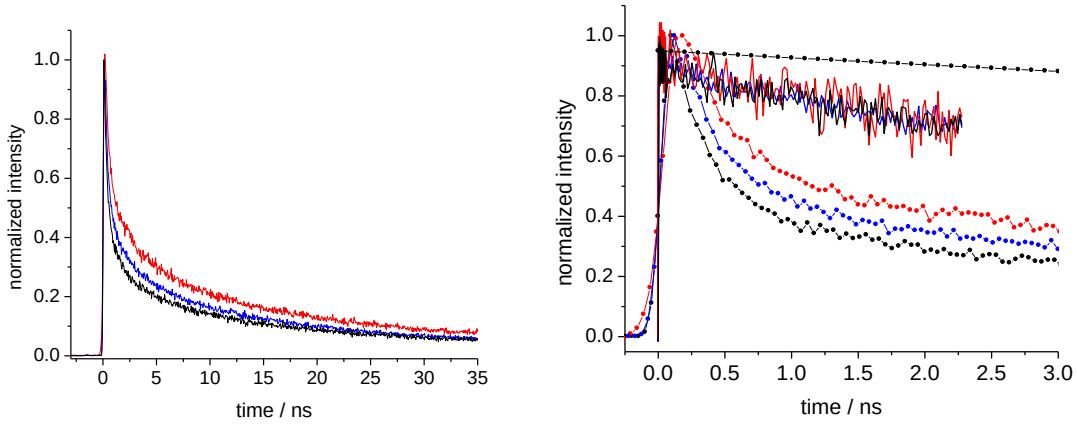

Figure 4.2. Normalized PL decay kinetics (left) and a comparison of short-time PL and TA kinetics (right); black: 0 Ag, red: 1 Ag, blue: 5 Ag per particle. Also shown is a dotted curve corresponding to a 40 ns (radiative lifetime) decay. The TA decays can be fit with an approximately 8 ns decay time.

The PL results show large amplitude decay components that are much faster than the radiative lifetime, which is about 40 ns for 3.1 nm particles.[30] This indicates that the exciton dynamics are dominated by nonradiative recombination processes. It is important to note that the comparison of PL and TA kinetics can be used to establish the assignment of this nonradiative process. This is because the TA and PL kinetics measure different aspects of the QD excited state. The PL decay measures the time-dependent exciton (conduction band electron and valence band hole) population. Loss of either carrier quenches the PL. In contrast, in the absence of multiple holes, the TA kinetics exclusively measure the state filling of the conduction band.[31] This occurs because the transitions available to the singly excited particle are degenerate with and have the same oscillator strength with an additional hole present. Ch 2.4 offers a more in-depth explanation of the phenomenon.

As a result, depletion of the conduction band electron population results in decays of both the PL and TA signals. In contrast, depletion of valence band holes (hole trapping) does not affect the conduction band population but does decreases the PL signal. Thus, if the exciton population is depleted by hole trapping, the PL will decrease at the rate of hole trapping, but no bleach recovery will be seen in the TA kinetics. The temporal resolution

of the PL decays is relatively slow, about 150 ps, whereas the temporal resolution of the TA measurements is much greater, about 1 ps. Despite this difference, comparison of these kinetics in Figure 4.2 shows that within the first nanosecond, the PL decay is much more rapid than the bleach recovery and that the dominant nonradiative process on this timescale is hole trapping. Figure 4.2 also shows that the difference between the TA and PL decay curves decreases upon introducing 1-2 Ag^+ ions per particle, then increases again at 5 Ag^+, tracking the non-monotonic trend in quantum yields. The conclusion is that the addition of small concentrations of Ag^+ diminishes the amount of hole trapping, while higher concentrations increase the amount of hole trapping.

Comparing the PL and TA kinetics along with static QY measurements gives further insights into the faster timescale (< 100 ps) dynamics. Fitting the 0Ag PL decay to a triexponential gives 0.33 ns (60%), 4.1 ns (23%), and 35 ns (15%) components. Assuming a 40 ns radiative lifetime,[30] this PL decay gives a calculated QY of 16%, whereas static measurements show that the actual QY is 3.0%. The ratio of these two values indicates that about 19% (i.e., 3/16) of the particles are seen in the PL decay measurement and the remaining 81% of the particles are dark. We conclude that the 81% of the QDs undergo a nonradiative decay which is faster than the 150 ps time resolution of the single-photon counting apparatus. Little or no fast component is seen in the TA measurements, indicating that virtually no fast electron trapping or Auger processes are occurring. From this comparison, we conclude that hole trapping also dominates the < 100 ps exciton dynamics. The bleach recovery kinetics are all the same within experimental error and can be fit to an 8.1 ± 0.2 ns single exponential. The process responsible for this rate of conduction band depletion is unassigned but may be due to electron trapping at surface states and/or recombination of the conduction band electron with the trapped hole.

The above results show that in the absence of an alkylamine, much of the population undergoes fast hole trapping, resulting in low overall QYs. The hole traps are surface-bound electron donors having nonbonding electrons above the valence band edge. In the present case, the hole traps are assigned to reduced seleniums (in the form of Se^{2-}, SeH^- or H_2Se) adsorbed on the QD surface. This assignment is in analogy to the surface sulfur hole traps assigned for the case of CdSe/CdS QDs.[19] We suggest that the addition of Ag^+ removes these traps through association with the surface-bound electron donors through a partial charge transfer mechanism. The reaction $2Ag^+ + Se^{2-} \rightarrow Ag_2Se$ can also be thought of as a charge transfer occurring with the surface selenium, $2Ag^+ + Se^{2-} \rightarrow 2Ag^0 + Se^0$. The filled selenium p-orbitals that are significantly above the valence band edge are the hole traps, and the electrons in these orbitals are both stabilized by and partially transferred to the Ag^+ dopants. Otherwise stated, hole trap passivation occurs to the extent that the silver ions are sufficiently close to the surface that they can interact with the surface seleniums. The product of the charge transfer is a partially ionic surface-bound Ag_2Se, and it is the formation of this species that makes the reaction energetically favorable. Following reaction, the oxidized selenium can no longer be oxidized by a VB hole, and the hole trap is passivated. In this mechanism, the filled, nonbonding selenium 4p orbitals form bonding orbitals with the silver dopant and are lowered in energy below the valence band. As such, the Fermi level of the QD is lowered and pinned at the energy of the Ag^+/Ag^0 redox couple, where the Ag^0 is associated with a surface selenium. This mechanism is outlined in Figure 4.3.

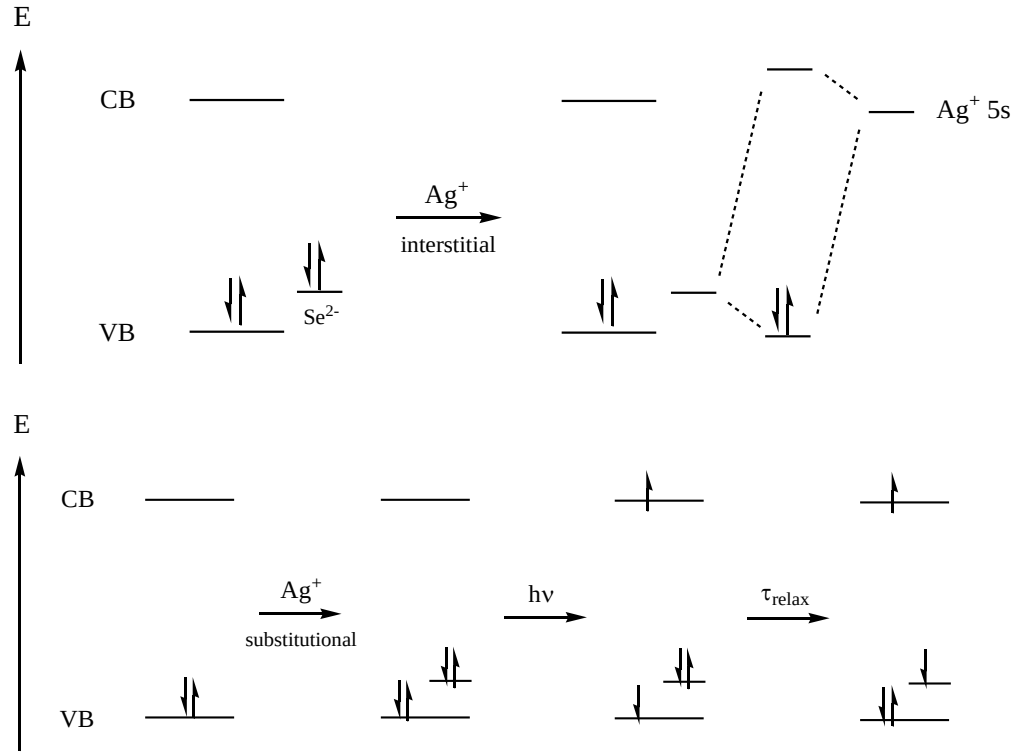

Figure 4.3. Differences in the photophysics between interstitial and substitutional doping. In low QY particles dominated by hole trapping, initial dopants go in interstitially (top) and passivate surface Se^{2-} ions. In the absence of a high density of reduced surface chalcogenide ions, the dopants go in substitutionally (bottom), which lowers the QY and gives rise to a mid-gap luminescence band Stokes-shifted by ~ 0.3 eV, as described in reference 3.

The present results indicate that the initial Ag dopants interact with surface traps but bear little further insight regarding the location of the subsequent Ag dopants. However, several studies bear on the question of dopant locations.[3, 7-9] EXAFS results suggest that the initial Ag dopant atoms go into the CdSe QD lattice interstitially, and that these interstitial sites are not on the surface.[8] However, computational studies suggest that an interstitial Ag^+ in the interior of the particle has the empty silver 5s-orbital in proximity with the conduction band and has no mid-gap states.[3] The reduction of interstitial Ag^+ ions to form Ag^0 would not be energetically favorable if the electron donor is a mid-gap hole trap. We therefore suggest that the silver dopants that passivate the hole traps correspond to the previously assigned interstitial dopant Ag ions[7] and are in close enough proximity to the surface to interact with the surface seleniums. These Ag^0 atoms could be actually on the QD surface or near the surface but in the crystal lattice, as suggested in reference 8.

Once all of the reduced selenium surface hole traps have been oxidized by the charge transfer and association reaction, further dopants that are introduced as Ag^+ remain as the

+1 ion. Previous studies have suggested that these Ag^+ dopants go in substitutionally.[3] Computational and experimental studies indicate the substitutional Ag^+ d-orbitals interact with the nearest neighbor selenium 4p-orbitals to form localized molecular orbitals. The higher energy, mostly selenium 4p molecular orbital is filled and significantly above the valence band edge. Thus, valence band holes can be localized in these orbitals, which manifests in the PL decay as increased hole trapping at greater dopant concentrations. We suggest that this is why further addition of Ag^+ results in a decrease in the QY. It follows that the further red-shifted luminescence seen in Figure 4.1 appears only after the QY maximum is reached. The initial dopants go in interstitially and can passivate surface Se^{2-} ions, and there are no mid-gap states associated with them. Further addition of Ag^+ results in a decrease in the quantum yields and is accompanied by the appearance of a broad PL band that is Stokes shifted by ~ 0.3 eV, indicating that these dopants must go in substitutionally. The two types of doping, interstitial and substitutional, and the different exciton dynamics which they give rise to are depicted in Figure 4.3.

Very different results are observed when a primary alkylamine is added to the solution used for introduction of the Ag^+ dopant. The presence of the amine dramatically raises the QY by eliminating most of the surface hole traps. An analogous effect has been reported in the case CdSe/CdS core/shell QDs.[19] These studies assert that in the case of CdSe/CdS, hole traps are present from surface adsorbed H_2S and the addition of the amine diminishes the extent of hole trapping by displacement or binding of the adsorbed H_2S. This type of passivation mechanism can presumably occur with surface-bound H_2Se as well. However, the direct binding mechanism is ubiquitous in QD studies, but there is a lack of direct evidence that this actually occurs. An alternative hole trap passivation mechanism (discussed in detail in Ch. 7) involves electron donation from the amine shifting the valence and conduction band levels to higher energies relative to the surface Se^{2-} trap states.[33, 34] If the Se^{2-} states are no longer above the valence band edge, then they can't act as hole traps, and interaction with interstitial Ag^+ will not raise the QY. All dopants, then, go in as substitutional Ag^+ and increase the hole trapping rate. Either or both mechanisms could explain the doping dynamics in the presence of an amine, and neither have been disproved.

4.2.3 CdSe/CdS core/shell QDs.

Accurate measurement of radiative lifetimes and assignments of nonradiative processes in CdSe and other semiconductor nanoparticles is often difficult due to inhomogeneities in the sample and low ensemble quantum yields. These factors complicate the analysis of the nonradiative processes seen in doped CdSe QDs. An approach that avoids these difficulties is to start with particles having a very high ensemble QY, introduce a known nonradiative pathway, and then examine the effect of the dopant on the dynamics. For this purpose, CdSe/CdS core/shell particles with varying shell thicknesses, surface ligands and dopant concentrations have been synthesized. In the initially synthesized particles, the surfaces were ligated with a combination of oleylamine and TBP and were therefore well passivated. The absorption and PL spectra of these QDs having a 2 ML CdS shell are shown in figure 4.4.

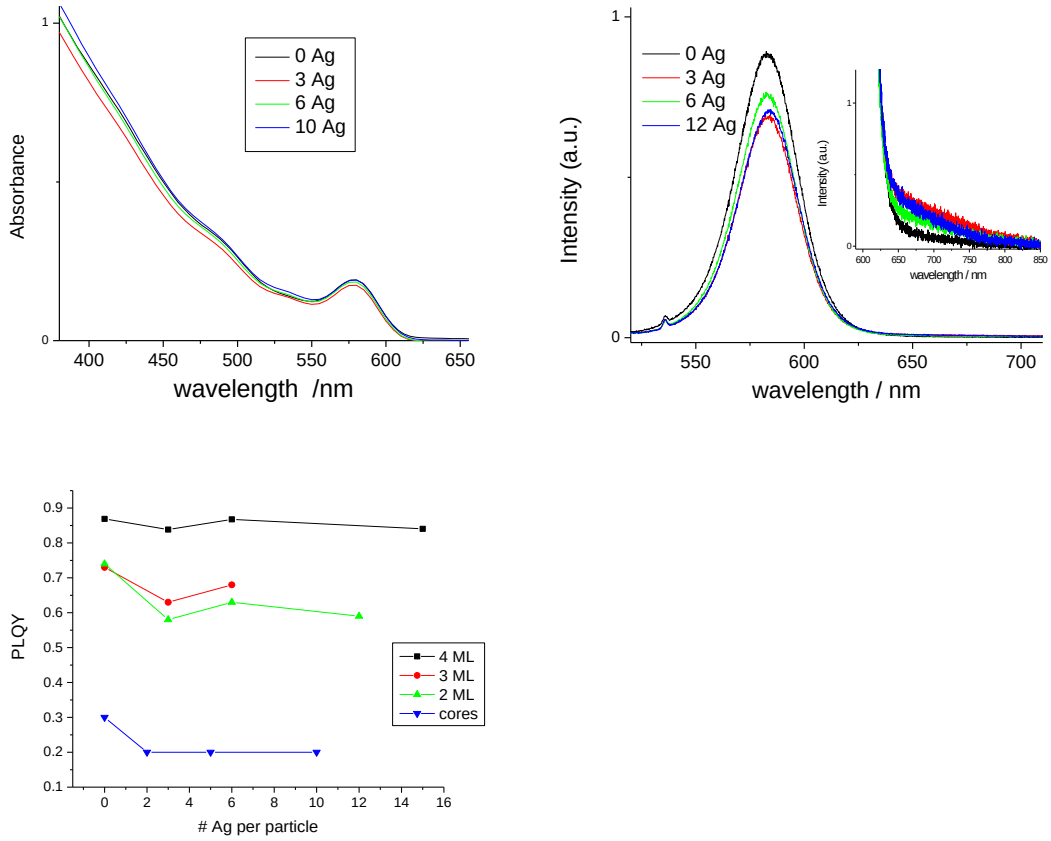

Figure 4.4. Absorption (left panel) and PL (center panel) spectra of CdSe/CdS QDs at varying dopant concentrations. The particles have a 2-ML thick shell and are treated with TBP and oleylamine. The inset shows an expanded scale of the far red region of the spectrum. Also shown (right panel) are ensemble QYs of CdSe and CdSe/CdSe core/shell particles.

As in the case of the CdSe QDs, addition of Ag^+ has little or no effect on the absorption spectrum. Prior to the addition of Ag^+, the overall PL QY was about 73%. The effects of Ag doping on the PL spectra and QY are weaker than in the case of the CdSe core particles, as is seen in the comparison of figures 1 and 3. The PL spectra of the doped CdSe/CdS QDs show a small decrease in the exciton luminescence and a weak feature in the 650 – 800 nm region. The PL QYs for these and other particles having different shell thicknesses are also summarized in figure 4.3. Addition of Ag significantly affects the cores and thin-shelled particles but has no effect on the 4ML core/shell particles. This supports the idea that the dopants interact primarily with surface states. When the surface is sufficiently decoupled from the core, PL quenching processes such as electron and hole trapping and surface charging are significantly diminished, and the dopant has little effect. This especially true if the dopants primarily reside in the shell, which constitutes a significant fraction of the QD volume.

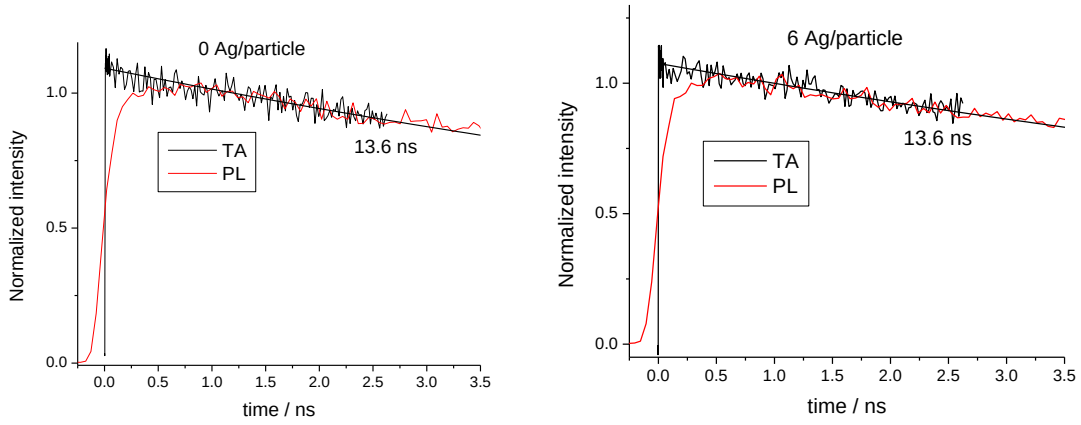

Figure 4.5. PL and TA kinetics of doped (right) and undoped (left) 2-ML CdSeCdS. Also shown in each plot is a 13.6 ns calculated decay curve.

The time-resolved PL and TA results for the 2-monolayer CdSe/CdS sample are shown in Figure 4.5. Comparison of the TA with the PL decays shows closely matching kinetics for both the 0Ag and 6Ag results. Furthermore, the decay times do not change with silver doping. However, 4.3 shows a small but significant static PL QY drop, from 74% to 63%, upon doping with 6 Ag. The doped particles have lower ensemble quantum yields and exhibit weak sub-band gap luminescence presumably because of some radiative but mainly nonradiative recombination of a conduction band electron with a dopant-localized hole. The conclusion is that a relatively small fraction of the Ag doped core/shell QDs exhibit fast (< 150 ps) hole localization at the dopant sites followed by slow (> 100 ns) radiative recombination with a conduction band electron. In the majority of the QDs, the Ag dopant has little effect on the overall exciton dynamics. These results raise an obvious question: with 6 Ag dopants per QD, why do only 15% show rapid hole trapping? This result suggests that a large fraction of the Ag^+ has been reduced to Ag^0 in the presence of the excess amine. Many literature reports support this idea. Although the silver dopant is added in the form of Ag^+, we note that oleylamine[35] can act as a reducing agent to form Ag^0. Oleylamine is known to act as a reducing agent for a variety of metals and semiconductor precursors.[36, 37] It has also been reported that Ag^+ is reduced to elemental silver by oleylamine to form silver nanoparticles at modest temperature (≈ 100 °C) in hydrocarbon solvents.[38] We also find that this reduction reaction proceeds rapidly upon addition of octylamine to a room temperature solution of $AgNO_3$. This is consistent with the observation that in the presence of primary alkyl amines, Ag-doped CdSe nanocrystals[7] and Ag_2E, E = S, Se, Te nanocrystals[35] will spontaneously precipitate metallic (reduced) silver. Furthermore, we note that the reduction potential of Ag^+ is 0.80 V versus SHE, while the oxidation potential of aliphatic amines is just above 1.0 V versus SHE, making the reduction energetically favorable.[39] Thus, in a solution containing oleylamine, we expect that silver may be present as both Ag^0 and Ag^+, and conclude that in the presence of oleylamine acting as a reducing agent, there is an equilibrium between oxidized and reduced silver: $Ag^+ + e^- \rightleftarrows Ag^0$. We conclude that the reason that addition of multiple

silver ions per QD to the solution results in only a modest effect on the dynamics is that most of the Ag^+ is reduced to Ag^0 by the oleylamine in the solution. Furthermore, we note that the small concentrations of Ag^+ used in the doping reactions preclude the possibility of the formation of nanoparticles of any appreciable size or quantity. To make hybrid metal/semiconductor nanostructures, the authors in references [40] and [41] use metal concentrations in the range 0.1 to 1 M, whereas our reactions are run at μM concentrations. This strongly suggests that reduced silver present in solution or on the nanoparticle surface is in the form of atoms rather than clusters or small particles.

Surface ligation controls the nature and density of the mid-gap states and the QDs discussed above are ligated with oleylamine and TBP. Oleylamine is used in the shell deposition, so the synthesis of comparable core/shell QDs in which an alkyl amine has been excluded is problematic. However, it is possible to exclude phosphine and we find that its absence from the particle surface alters the PL and TA kinetics. Figure 5 shows the PL decays and quantum yields for 2-monolayer CdSe/CdS particles passivated with oleylamine but no phosphine. In the absence of the phosphine, the TA decays show a large fast component attributed to the positive trion and a slower component attributed to electron trapping at surface S(0) atoms. These kinetics are shown in Figure 4.6

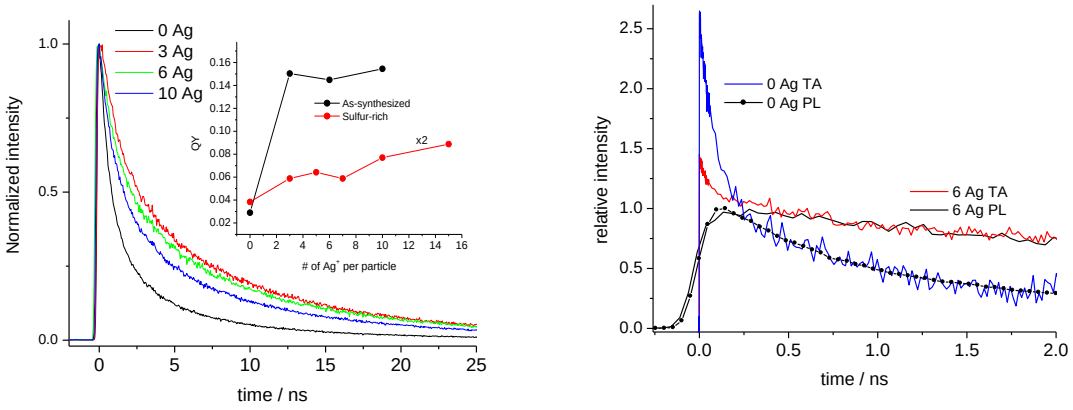

Figure 4.6. Time resolved spectroscopy of Ag-doped CdSe/CdS 2ML with no phosphine present. Left: PL decays as a function of dopant concentration, as indicated. The inset shows the static QYs. Right: short-time comparison of the PL and TA decays with 0 and 6 Ag dopants per QD. The TA and PL decay curves are scaled to match at times > 1 ns.

Two aspects of the comparison are notable. First, there is a close match in the slower (> 250 ps) decay components, and second, a fast component is seen in the undoped TA kinetics which has a much smaller amplitude than in the PL. We first consider both of these aspects of the kinetics for the undoped QDs. The match of the slow (0.25 – 2.0 ns timescale) TA and PL components indicates that the nonradiative process responsible for this decay component is depleting the conduction band. Thus, the slow component of the exciton lifetime is limited by electron, rather than hole trapping. This is in contrast to TPB-ligated QDs discussed above, and we will return to this observation.

The TA kinetics show a large-amplitude 80 ps decay component, coinciding with what is expected for the positive trion Auger process for this core size and shell thickness.[14] It

is important to note that the 80 ps TA decay component has a very small amplitude in the PL decay. This difference in relative amplitude is partially due to the lower time resolution of the PL experiment. However, the amplitude of the 80 ps TA decay component is sufficiently large and the 150 ps resolution of the PL kinetics is sufficiently close to the 80 ps decay time that a significant amount of the fast component is expected to be present in PL kinetics. Furthermore, we have repeated this experiment with a PL time resolution of 45 ps, and even with time resolution capable of fully resolving this component, only a relatively small fast component is observed.

The presence of a larger amplitude fast component in the bleach recovery compared to the PL decay kinetics indicates that this decay corresponds to a process that cannot be assigned to quenching of the exciton – if it were due to an exciton quenching process, the relative amplitudes would be the same in the TA and PL kinetics. Rather, this result indicates that the fast component must correspond to the quenching of an electronic state that is different than the exciton. We assign this state to the surface charged trion. The reason for its larger amplitude in the TA bleach recovery kinetics is related to the fact that the trion has two valence band holes. The exciton has a single valence band hole and only gives conduction band state filling, as previously discussed. The trion has state filling of the both valence and conduction bands, which is the main reason why the trion shows a larger bleach. We also note that the exciton and trion can have different oscillator strengths and therefore different amounts of stimulated emission,[42] which can affect the TA spectrum and kinetics. The details of the positive trion spectroscopy will be discussed in greater detail in Ch 5. The important point here is extensive surface charging is seen in thin-shelled CdSeCdS in the absence of TBP, and adding Ag^+ in oleylamine diminishes the effect.

Uncertainties in the trion versus exciton oscillator strengths hinder quantitative analysis of the fraction of surface charged QDs. Despite this caveat, a semiquantitative analysis of the PL and TA decays along with the static QYs gives a consistent description of the dynamics. The PL kinetics of the undoped QDs can be fit to a biphasic decay having 0.90 ns (75%) and 6.7 ns (25%) components. Fits to the PL and TA decay curves and the associated fitting parameters and their uncertainties are shown in figures S2 and S3. Taking the radiative lifetime for this core diameter and shell thickness to be 26 ns[43] gives a QY for the particles seen in the PL decay of 9.0%. In comparison, the observed QY for these undoped QDs is 3.0%. This comparison indicates that only 33% of the QDs are seen in the PL decay. Otherwise stated, 67% of these QDs are dark, having a nonradiative decay that is much faster than the 150 ps resolution of the time-correlated photon-counting apparatus. This is consistent with the 0 Ag TA kinetics (figure 5) showing that the amplitude of the fast TA component is about 53% of the total. This suggests that the trion 1S bleach magnitude is about ~ 25% greater than in the exciton, but a few more experiments would be needed to validate this result.

The extent of long-time and especially short-time (trion) quenching is diminished by doping, i.e., the decays become considerably longer and the QYs increase with the addition of the Ag dopants. The kinetic parameters obtained from fitting the PL decay curves are collected in table 4.1.

Table 4.1. PL decay kinetics and QY parameters

Ag/particle	A1	τ_1 (ns)	A2	τ_2 (ns)	QY * (calc)	QY (meas)	Bright fraction
0	0.75	0.8	0.25	6.7	9.0	3.0	0.33
3	0.56	1.9	0.44	11.0	22.7	15	0.66
6	0.55	1.9	0.45	11.4	20.3	14	0.69
10	0.62	1.5	0.35	10.5	17.4	16	0.92

*Assuming a radiative lifetime of 26 ns.[43]

The large fraction of particles that exhibit surface charging in the absence of Ag dopants suggests that the shell synthesis reaction with DDTC/amine in the absence of TOP generates excess sulfur and deposits elemental sulfur on the QD surface. The elemental sulfur acts as an electron acceptor, resulting in surface charging. The same surface sulfur states can also accept conduction band electrons and quench excitons through electron trapping. The dopant concentration-dependent results show that addition of Ag dopants changes the dynamics in several ways. Most dramatically, it diminishes the extent of surface charging. The fraction of bright particles increases from 33% to 92% upon addition of the Ag dopants. Diminished surface charging indicates that the addition of silver passivates the oxidized (elemental) sulfur on the surfaces. Ag^+ would not be expected to react with elemental sulfur, but Ag^0 can give up an electron to reduce the surface sulfur. As discussed above, the excess oleylamine reduces much of the added Ag^+ to Ag^0. We therefore propose that it is the reaction of Ag^0 with the elemental surface sulfurs that eliminates the surface charged particles.

Figure 4.6 and Table 4.1 show that addition of Ag also increases the longer timescale nonradiative decay times. This observation is consistent with the assignment that electron trapping controls the longer-lived PL decay dynamics. As in the case of the CdSe QDs, comparison of the PL and TA decay kinetics can establish whether it is electron or hole trapping that is the dominant decay pathway. Figure 4.6 shows a match between the long-time PL and TA decays, indicating that the depletion of conduction band electrons matches the exciton depletion, i.e., the exciton lifetime is limited by electron trapping. The conclusion is that the silver dopants fill sulfur surface states that are responsible for both surface charging and electron trapping. This mechanism is shown in Figure 4.7. We also note that at the highest Ag concentrations a somewhat faster PL decay is observed, just as in the case of the CdSe (core-only) QDs, see Figure 4.2. We suggest that this occurs for the same reason, specifically, that substitutional Ag^+ dopants act as hole traps.

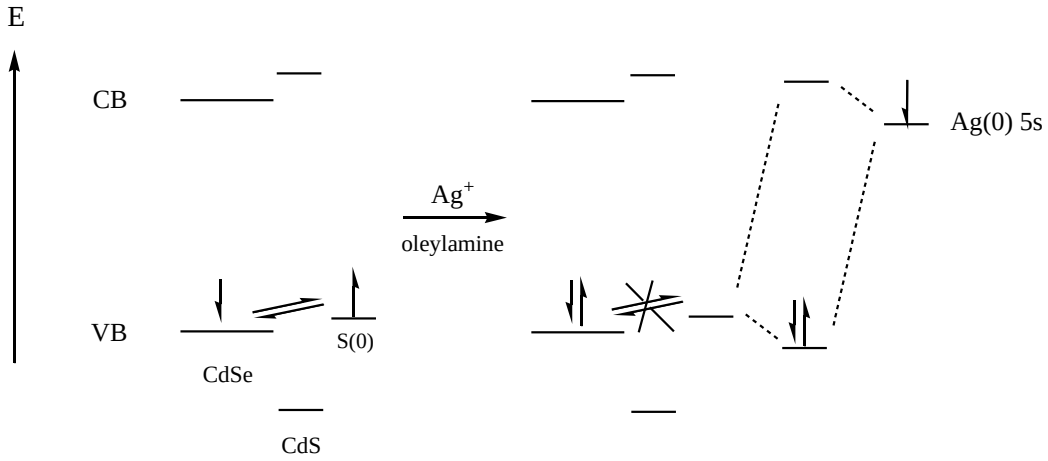

Figure 4.7. The effect of Ag on oleylamine-passivated CdSe/CdS QDs. Before addition of Ag, mid-gap states can be thermally populated from the valence band and act as electron traps. In the presence of oleylamine, most of the Ag^+ is reduced to Ag^0, which reacts with surface elemental sulfur atoms.

The above proposed mechanism suggests that increasing the density of elemental sulfur surface atoms will increase the Ag concentration needed for passivation. The figure 5 inset shows that this is the case. The QY for the as-synthesized particle levels out after the addition of about 3 Ag dopants. In contrast, when a sub-monolayer amount of elemental sulfur is added to the particle surface, the maximum in QY as a function of dopant concentration is pushed toward higher concentrations, i.e., the QY of the sulfur-rich particles continues to increase to at least 15 Ag dopants per QD. This comparison indicates that as the surface density of unligated elemental sulfur is increased, more dopant ions are required to attain higher quantum yields.

Later studies [45] provided more insight into the differences in dynamics when doping with vs without amines in the reaction mixture. Amines are L-type ligands, meaning that they donate electron density to the particle upon ligation. The interaction creates a surface dipole that shifts the band energies ~ 200 meV up in energy, whereas the surface trap states exist outside of the dipole layer and are relatively unaffected. This is why the particles treated with just TBP (left on Figure 4.8) undergo hole trapping while the TBP + amine-treated particles (Figure 4.8 right) undergo surface charging and electron trapping. The silver redox level is fortunately placed, where Ag+ can oxidize a hole trapping state and Ag(0) can reduce an electron trapping state.

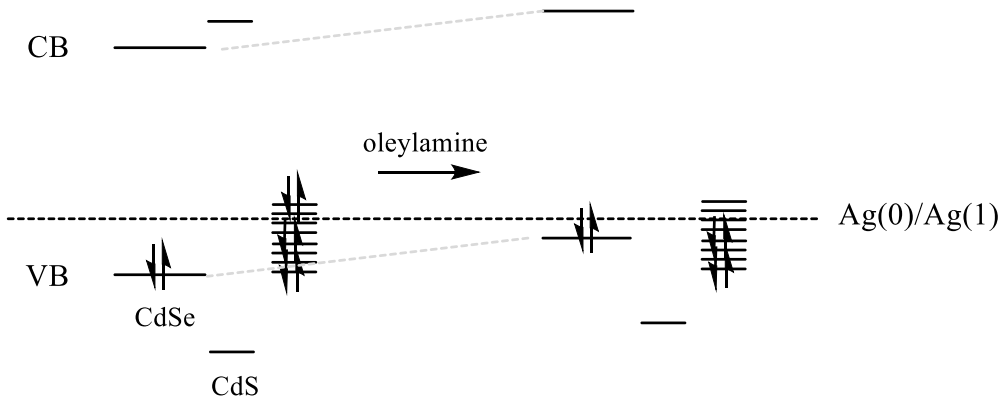

Figure 4.8 Band edge and trap state energies relative to the Ag/Ag^+ redox level before and after adding amine.

4.3 Conclusions

This study examines the effect of silver doping on the carrier dynamics of CdSe and CdSe/CdS core/shell nanoparticles and finds that the behavior of the dopant depends critically on the nanoparticle surface composition and the Ag oxidation state. Hole traps are associated with nonbonding electrons in reduced chalcogenide surface orbitals. In TBP-ligated CdSe, the initially added Ag^+ undergoes a partial charge transfer interaction with these orbitals to passivate hole traps. Further addition of Ag^+ introduces a weakly luminescent mid-gap state and decreases the band-edge PL quantum yields. Hole traps can also be passivated by amines, and with both TBP and amines present, addition of Ag^+ results only in the production of the luminescent mid-gap states and a loss of overall QY. Oxidized surface chalcogenides can accept valence band electrons, leaving a valence band hole. Subsequent photoexcitation of this surface charged state produces a positive trion (two holes and one electron) that can undergo a rapid nonradiative Auger process. Ag^+ can be reduced to Ag^0 when alkylamines are in the solution, and the reduced dopant can passivate elemental chalcogenide atoms present on the nanoparticle surface. This surface reaction can largely shut off the surface charging quenching mechanism. To the extent that the oxidized surface chalcogenides can quench the exciton by electron trapping, the presence of Ag^0 also diminishes this quenching.

Ch. 4 References

1. Norris, D. J.; Efros, A. L.; Erwin, S. C., Doped Nanocrystals. *Science* **2008,** *319*, 1776-1779.
2. Erwin, S. C.; Zu, L.; Haftel, M. I.; Efros, A. L.; Kennedy, T. A.; Norris, D. J., Doping semiconductor nanocrystals. *Nature* **2005,** *436*, 91 - 94.
3. Nelson, H. D.; Hinterding, S. O. M.; Fainblat, R.; Creutz, S. E.; Li, X.; Gamelin, D. R., Mid-Gap States and Normal vs Inverted Bonding in Luminescent Cu+- and Ag+-Doped CdSe Nanocrystals. *J. Am. Chem. Soc.* **2017,** *139*, 6411-6421.
4. Yen, W. M.; Shionoya, S.; Yamamoto, H., Eds., *Fundamentals of Phosphors, 2nd ed.* CRC Press: Boca Raton, FL, 2007.
5. Beberwyck, B. J.; Surendranath, Y.; Alivisatos, A. P., Cation Exchange: A Versatile Tool for Nanomaterials Synthesis. *J. Phys. Chem. C* **2013,** *117*, 19759−19770.
6. Li, H.; Zanella, M.; Genovese, A.; Povia, M.; Falqui, A.; Giannini, C.; Manna, L., Sequential Cation Exchange in Nanocrystals: Preservation of Crystal Phase and Formation of Metastable Phases. *Nano Lett.* **2011,** *11*, 4964-4970.
7. Sahu, A.; Kang, M. S.; Kompch, A.; Notthoff, C.; Wills, A. W.; Deng, D.; Winterer, M.; Frisbie, C. D.; Norris, D. J., Electronic Impurity Doping in CdSe Nanocrystals. *Nano Lett.* **2012,** *12*, 2587-2594.
8. Kompch, A.; Sahu, A.; Notthoff, C.; Ott, F.; Norris, D. J.; Winterer, M., Localization of Ag Dopant Atoms in CdSe Nanocrystals by Reverse Monte Carlo Analysis of EXAFS Spectra. *J. Phys. Chem. C* **2015,** *119*, 18762-18772.
9. Almeida, A. J.; Sahu, A.; Riedinger, A.; Norris, D. J.; Brandt, M. S.; Stutzmann, M.; Pereira, R. N., Charge Trapping Defects in CdSe Nanocrystal Quantum Dots. *J. Phys. Chem. C* **2016**, ASAP.
10. Cohn, A. W.; Rinehart, J. D.; Schimpf, A. M.; Weaver, A. L.; Gamelin, D. R., Size Dependence of Negative Trion Auger Recombination in Photodoped CdSe Nanocrystals. *Nano Lett.* **2014,** *14*, 353-358.
11. Tsui, E. Y.; Carroll, G. M.; Miller, B.; Marchioro, A.; Gamelin, D. R., Extremely Slow Spontaneous Electron Trapping in Photodoped n-Type CdSe Nanocrystals. *Chem. Mater.* **2017,** *29*, 3754-3762.
12. Jha, P. P.; Guyot-Sionnest, P., Trion Decay in Colloidal Quantum Dots. *ACS Nano* **2009,** *3*, 1011-1015.
13. Park, Y.-S.; Bae, W. K.; Pietryga, J. M.; Klimov, V. I., Auger Recombination of Biexcitons and Negative and Positive Trions in Individual Quantum Dots. *ACS Nano* **2014,** *8*, 7288–7296.
14. Gong, K.; Kelley, D. F., Surface Charging and Trion Dynamics in CdSe-Based Core/Shell Quantum Dots. *J. Phys. Chem. C* **2015,** *119*, 9637-9645.
15. Rinehart, J. D.; Schimpf, A. M.; Weaver, A. L.; Cohn, A. W.; Gamelin, D. R., Photochemical Electronic Doping of Colloidal CdSe Nanocrystals. *J. Am. Chem. Soc.* **2013,** *135*, 18782-18785.
16. Zeng, Y.; Kelley, D. F., Excited Hole Photochemistry of CdSe/CdS Quantum Dots. *J. Phys. Chem. C* **2016,** *120*, 17853-17862.

17. Zeng, Y.; Kelley, D. F., Two-Photon Photochemistry of CdSe Quantum Dots. *ACS Nano* **2015,** *9*, 10471 - 10481.
18. Jasieniak, J.; Mulvaney, P., From Cd-Rich to Se-Rich - the Manipulation of CdSe Nanocrystal Surface Stoichiometry. *J. Am. Chem. Soc.* **2007,** *129*, 2841-2848.
19. Pu, C.; Peng, X., To Battle Surface Traps on CdSe/CdS Core/Shell Nanocrystals: Shell Isolation versus Surface Treatment. *J. Am. Chem. Soc.* **2016,** *138*, 8134-8142.
20. Kim, W.; Lim, S. J.; Jung, S.; Shin, S. K., Binary Amine-Phosphine Passivation of Surface Traps on CdSe Nanocrystals. *J. Phys. Chem. C* **2010,** *114*, 1539-1546.
21. Busby, E.; Anderson, N. C.; Owen, J. S.; Sfeir, M. Y., Effect of Surface Stoichiometry on Blinking and Hole Trapping Dynamics in CdSe Nanocrystals. *J. Phys. Chem. C* **2015,** *119*, 27797−27803.
22. Anderson, N. C.; Hendricks, M. P.; Choi, J. J.; Owen, J. S., Ligand Exchange and the Stoichiometry of Metal Chalcogenide Nanocrystals: Spectroscopic Observation of Facile Metal-Carboxylate Displacement and Binding. *J. Am. Chem. Soc.* **2013,** *135*, 18536−18548.
23. Cai, X.; Martin, J. E.; Shea-Rohwer, L. E.; Gong, K.; Kelley, D. F., Thermal Quenching Mechanisms in II-VI Semiconductor Nanocrystals. *J. Phys. Chem. C* **2013,** *117*, 7902 - 7913.
24. Zeng, Y.; Kelley, D. F., Surface Charging in CdSe Quantum Dots: Infrared and Transient Absorption Spectroscopy. *J. Phys. Chem. C* **2017,** *121*, 16657-16664.
25. Nan, W.; Niu, Y.; Qin, H.; Cui, F.; Yang, Y.; Lai, R.; Lin, W.; Peng, X., Crystal Structure Control of Zinc-Blende CdSe/CdS Core/Shell Nanocrystals: Synthesis and Structure-Dependent Optical Properties. *J. Am. Chem. Soc.* **2012,** *134*, 19685−19693.
26. Pu, C.; Zhou, J.; Lai, R.; Niu, Y.; Nan, W.; Peng, X., Highly Reactive, Flexible Yet Green Se Precursor for Metal Selenide Nanocrystals: Se-Octadecene Suspension (Se-SUS). *Nano Research* **2013,** *6*, 652-670.
27. Jasieniak, J.; Smith, L.; van Embden, J.; Mulvaney, P.; Califano, M., Re-examination of the Size-Dependent Absorption Properties of CdSe Quantum Dots. *J. Phys. Chem. C* **2009,** *113*, 19468 - 19474.
28. Yu, W. W.; Qu, L.; Guo, W.; Peng, X., Experimental Determination of the Extinction Coefficient of CdTe, CdSe, and CdS Nanocrystals. *Chem. Mater.* **2003,** *15*, 2854 - 2860.
29. Li, J. J.; Wang, Y. A.; Guo, W.; Keay, J. C.; Mishima, T. D.; Johnson, M. B.; Peng, X., Large-Scale Synthesis of Nearly Monodisperse CdSe/CdS Core/Shell Nanocrystals Using Air-Stable Reagents via Successive Ion Layer Adsorption and Reaction. *J. Am. Chem. Soc.* **2003,** *125*, 12567 - 12575.
30. Gong, K.; Zeng, Y.; Kelley, D. F., Extinction Coefficients, Oscillator Strengths, and Radiative Lifetimes of CdSe, CdTe, and CdTe/CdSe Nanocrystals. *J. Phys. Chem. C* **2013,** *117*, 20268-20279.
31. Klimov, V. I., Spectral and Dynamical Properties of Multiexcitons in Semiconductor Nanocrystals. *Annu. Rev. Phys. Chem.* **2007,** *58*, 635-73.
32. Efros, A. L.; Rosen, M.; Kuno, M.; Nirmal, M.; Norris, D. J.; Bawendi, M., Band-Edge Exciton in Quantum Dots of Semiconductors With a Degenerate Valence Band: Dark and Bright Exciton States. *Phys. Rev. B* **1996,** *54*, 4843 - 4856.

33. Jasieniak, J.; Califano, M.; Watkins, S. E., Size-Dependent Valence and Conduction Band-Edge Energies of Semiconductor Nanocrystals. *ACS Nano* **2011,** *5*, 5888–5902.
34. Bloom, B. P.; Zhao, L.-B.; Wang, Y.; Waldeck, D. H.; Liu, R.; Zhang, P.; Beratan, D. N., Ligand-Induced Changes in the Characteristic Size-Dependent Electronic Energies of CdSe Nanocrystals. *J. Phys. Chem. C* **2013,** *117*, 22401-22411.
35. Sahu, A.; Qi, L.; Kang, M. S.; Deng, D.; Norris, D. J., Facile Synthesis of Silver Chalcogenide (Ag2E; E = Se, S, Te) Semiconductor Nanocrystals. *J. Am. Chem. Soc.* **2011,** *133*, 6509-6512.
36. Mourdikoudis, S.; Liz-Marzán, L. M., Oleylamine in Nanoparticle Synthesis. *Chem. Materials* **2013,** *25*, 1465-1476.
37. Xu, Z.; Shen, C.; Hou, Y.; Gao, H.; Sun, S., Oleylamine as Both Reducing Agent and Stabilizer in a Facile Synthesis of Magnetite Nanoparticles. *Chem. Materials* **2009,** *21*, 1778-1780.
38. Chen, M.; Feng, Y.-G.; Wang, X.; Li, T.-C.; Zhang, J.-Y.; Qian, D.-J., Silver Nanoparticles Capped by Oleylamine: Formation, Growth, and Self-Organization. *Langmuir* **2007,** *23*, 5296-5304.
39. Roth, H. G.; Romero, N. A.; Nicewicz, D. A., Experimental and Calculated Electrochemical Potentials of Common Organic Molecules for Applications to Single-Electron Redox Chemistry. *Synlett* **2016,** *27*, 714-723.
40. Balakrishnan, S.; Kamat, P. V., Au−CsPbBr3 Hybrid Architecture: Anchoring Gold Nanoparticles on Cubic Perovskite Nanocrystals. *ACS Energy Lett.* **2017,** *2*, 88-93.
41. Ye, S.; Yu, M.; Yan, W.; Song, J.; Qu, J., Enhanced Photoluminescence of CsPbBr3@Ag Hybrid Perovskite Quantum Dots. . *J. Mater. Chem. C* **2017,** *5*, 8187-8193.
42. Shabaev, A.; Rodina, A. V.; Efros, A. L., Fine Structure of the Band-Edge Excitons and Trions in CdSe/CdS Core/Shell Nanocrystals. *Phys. Rev. B* **2012,** *86*, 205311-205325.
43. Gong, K.; Martin, J. E.; Shea-Rohwer, L. E.; Lu, P.; Kelley, D. F., Radiative Lifetimes of Zincblende CdSe/CdS Quantum Dots. *J. Phys. Chem. C* **2015,** *119*, 2231-2238.
44. Morgan, D.; Gong, K.; Kelley, A.; Kelley, D., Biexciton Dynamics in Alloy Quantum Dots. J. Phys. Chem. C. **2017**, 121 (33), 18307–1831645.
45. Morgan, D. P.; Kelley, D. F. Mechanism of Hole Trap Passivation In CdSe Quantum Dots by Alkylamines. *J. Phys. Chem. C.* **2018**, *122* (44), 25661–25667

Ch 5

Spectroscopic Identification of the Positive Trion In Surface p-Doped CdSe and CdSe/CdS Quantum Dots

Abstract

A combination of transient absorption (TA) and time-resolved photoluminescence (PL) spectroscopy has been used to provide direct spectroscopic evidence for the recently reported phenomenon of thermal "surface charging" in II-VI quantum dots (QDs). In these studies, zincblende CdSe cores are synthesized by standard methods and a thin CdS shell deposited by the decomposition of $Cd(DDTC)_2$, resulting in core/shell QDs with a chalcogenide-rich surface. Following ligand exchange with oleylamine, these QDs have empty low-lying surface states that can be thermally populated from the valence band. At room temperature, the surface charging equilibrium results in some fraction of the particles having a hole in the valence band, i.e., the surface acceptor states make the particle p-type. Photoexcitation of the surface charged state results in a positive trion which then undergoes a fast Auger recombination. Both PL and TA (bleach recovery) kinetics of the CdSe/CdS QDs show a 70 ps decay component, which is assigned to Auger recombination. Passivation of the empty nonbonding surface orbitals by ligation with a trialkylphosphine significantly raises the PLQY and completely eliminates the fast decay component. The comparison of the TA and PL kinetics shows that the relative amplitude of the 70 ps component is a factor of about 1.5 greater in the TA than in the PL. They also show that the fast component in the PL spectrum is shifted several nanometers to the blue of the exciton luminescence. The above observations can be understood in terms of the trion versus exciton spectroscopy and strongly support the assignment of the 70 ps transient to the decay of a positive trion formed from the surface charged state.

5.1 Introduction

The well-established picture of the ground state electronic structure in CdSe-based nanoparticles is a filled valence band composed primarily of the Se 4p orbitals, an unfilled conduction band composed primarily of Cd 5s orbitals, and an unspecified number of mid-gap surface states which can be either filled or empty depending on the redox conditions of the synthesis and post-synthetic environment.[1-3] Simple molecular orbital theory considerations place the energies of coordinately unsaturated surface Se 4p and Cd 5s orbitals just above the valence band and below the conduction band edge, respectively. The dynamics of how unpassivated orbitals interact with an exciton depends on which orbitals are full and which are empty, i.e., the Fermi level of the QD. Empty or full orbitals can act as electron or hole traps, respectively, and passivation can be accomplished through appropriate surface binding organic ligands.[4-7] These ligands remove the surface states from the band gap, making them unavailable as electron or hole traps. Surface cadmium atoms are typically passivated by Lewis bases, and electron trapping does not usually limit the exciton lifetime or photoluminescence (PL) quantum yield (QY).[8] If the Fermi level is well above the valence band edge, then low-lying filled selenium 4p orbitals can donate an electron to fill a valence band hole. This quenches the exciton, and hole trapping at surface states is often the dominant nonradiative process.

How the Fermi level affects the electronic processes in these QDs is depicted in Figure 5.1. If the QD surfaces are primarily chalcogenide-terminated, then charge neutrality requires that the excess surface chalcogenides be in elemental form. This is the case when the CdS shell of a CdSe/CdS QD is grown from cadmium diethyldithiocarbamate, $Cd(DDTC)_2$, as is done here. The $Cd(DDTC)_2$, sulfur to cadmium ratio is 4, and the excess sulfur likely yields particles that are sulfur-rich at the surface. The same result can be accomplished by the reaction of QDs with the elemental chalcogenide.[9] The presence of an excess of adsorbed elemental sulfur on the QD surface establishes the Fermi level at a low energy. This situation is stable because at room temperature there are no other species in solution having facile mechanisms to reduce the QD surfaces.

Particles having a significant density of unpassivated sulfur 3p surface states and a Fermi level just above (within a few kT) the valence band are examined in this chapter. In this case, a valence band electron can be thermally promoted to empty surface states, leaving a hole in the valence band. The net effect is that the presence of the electron-accepting surface states results in a steady-state population of p-doped or "surface charged" QD. We note that if the Fermi level is low and the density of empty surface states is high then a large fraction of the QDs can be surface charged.

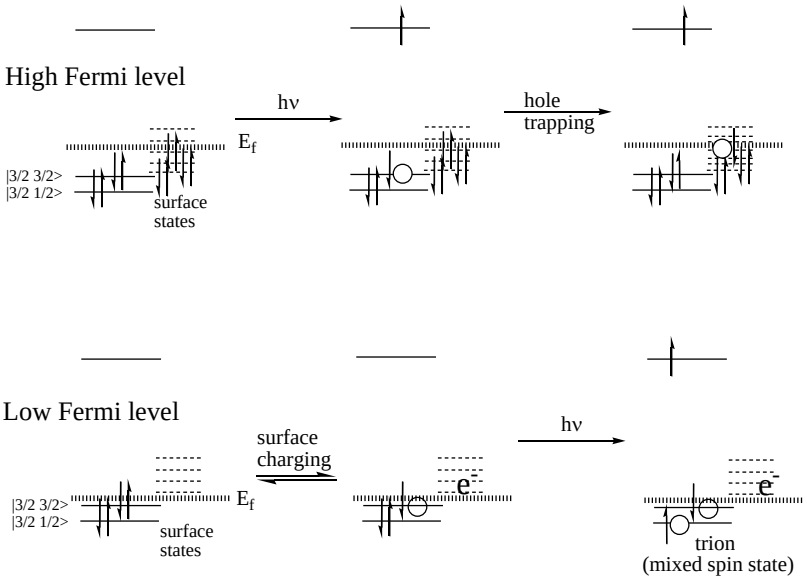

Figure 5.1. Valence band electronic processes of QDs with unpassivated surface states and a high (top) and low (bottom) Fermi level. Holes are indicated with open circles. The surface electron is taken to be decoupled from the interior electrons.

Photoexcitation of a surface charged QD produces a conduction band electron and two holes in the valence band; it is essentially a positive trion. The trion can undergo Auger recombination, where an electron and hole recombine and transfer the energy to the other hole.[10-12] This process is fast compared to radiation, and the surface charged QDs are

essentially nonluminescent. This thermally induced surface charging mechanism was first proposed to explain the ligand-dependent thermal quenching dynamics seen in CdSe, CdSe/ZnSe and CdTe QDs.[13] In that study it was shown that trialkylphosphines, which are known to bind to empty surface chalcogenides,[14] effectively passivate chalcogenide-rich QD surfaces. A later study showed that the presence of Ag(0) also serves to passivate empty surface chalcogenide orbitals and shuts off the trion Auger recombination.[15]

A later paper corroborates this assignment by comparing measured trion Auger times with those of the biexciton.[16] Both the positive trion and the biexciton have two valence band holes. But the biexciton has two conduction band electrons compared to just one for the trion. Thus, the Auger pathway degeneracy for a biexciton is 8; either electron can recombine with either hole. In contrast, the Auger pathway degeneracy for the positive trion is 2; the single electron can recombine with either hole.[10, 11] In the case of II-VI QDs, it has been shown that the dominant biexciton Auger pathway involves formation of a hot hole, rather than a hot electron.[17] This is explained in detail in Ch 2.2. Briefly, the greater hole effective mass yields more localized hole wavefunctions and a greater density of hole continuum states, both of which facilitate Auger recombination. Neglecting hot electron formation, the conclusion is that Auger recombination for the biexciton is predicted to be a factor of 2 faster than for the trion, and consideration of the minor electron excitation channel changes this value only slightly. This was experimentally shown to be the case for the surface charged trion.[16] The surface charging mechanism has also been proposed to understand the one-photon hot hole photochemistry observed for CdSe and CdSe/CdS QDs in polar solvents.[18,19] In these studies the hot hole produced by trion Auger recombination oxidizes an alkylamine ligand. The charged ligand can then dissociate from the QD in polar solution. As in the thermal quenching studies,[13] this process is shut off if a trialkylphosphine is present in the solution.

In the above studies, the presence of surface charging and the trion state formed upon photoexcitation is inferred from the luminescence quenching, the transient absorption bleach recovery rates and the hot hole photochemistry. However, what has been lacking is spectroscopic characterization of the surface charged or trion states. Below, we present a comparison of the ligand-dependent TA and PL kinetics of CdSe and CdSe/CdS QDs that provides direct spectroscopic evidence of the positive trion and distinguishes it from the uncharged excitonic state.

5.2 Results and Discussion

5.2.1 Trion luminescence quenching

The absorption spectra of 3.0 nm CdSe and CdSe/CdS QDs of the same 3.0 nm cores and a 2 monolayer (0.6 nm) CdS shell are shown in Figure 5.2. The PL spectra of the core/shell QDs ligated with either oleylamine (OAm) or oleylamine and tributylphosphine (TBP) are also shown.

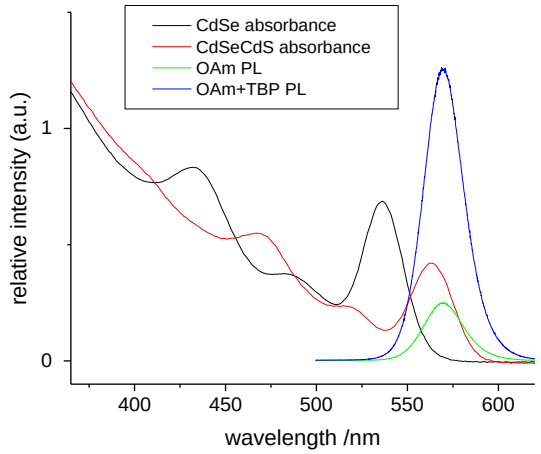

Figure 5.2 Absorbance spectra of 3.0 nm CdSe particles before and after deposition of a 2-ML CdS shell. The photoluminescence spectra of the core/shell particles treated with either oleylamine or TBP+oleylamine are also plotted. The relative intensities of the PL spectra reflect their QYs which are 73% (TBP+oleylamine) and 14.8% (oleylamine).

When ligated with OAm and TPB the PLQY is high, 73%. This is consistent with the slow, 16.9 ns single exponential PL decay, as shown in figure 5.3A. This decay time, along with the observed 73% QY, corresponds to a 23.1 ns radiative lifetime, which is about what is expected for this size core/shell QD.[20] Figure 5.3A also shows that the TA decay matches the PL decay over the limited time of the TA experiment. These results indicate that these well-passivated QDs exhibit only very slow nonradiative processes.

Very different results are obtained in the absence of TBP, where the QY drops by about a factor of 5, to 14.8%. Accordingly, the presence or absence of TBP also results in dramatic differences in the TA and PL kinetics, as shown in figure 2B.

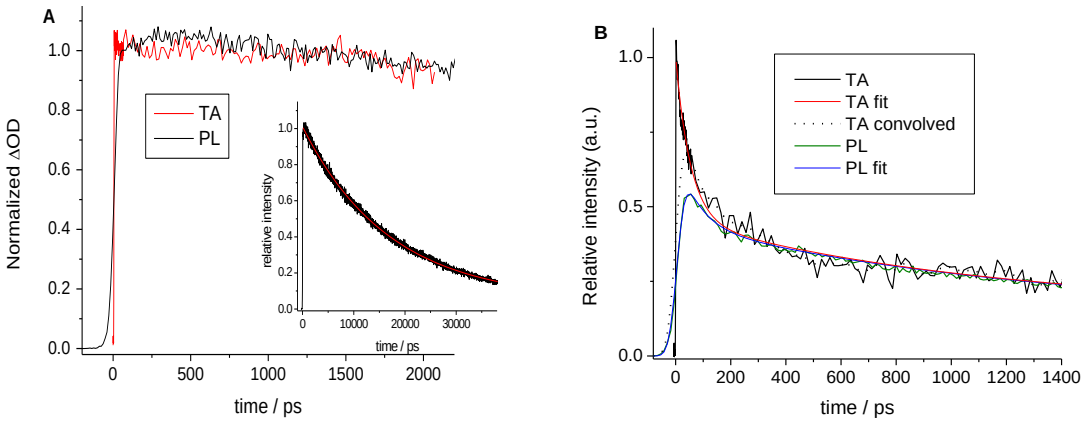

Figure 5.3. Transient absorption (TA) bleach recovery and PL kinetics, along with fit curves of 2ML CdSe/CdS particles (A) treated with TBP and oleylamine, and (B) treated only with oleylamine. The inset in A shows longer-time PL decay and a 16.9 ns single exponential decay. Also shown in B is the TA decay convolved with the PL instrument response and fit curves corresponding to 70 ps, 980 ps and 11 ns decay components having relative amplitudes of 55%, 22% and 23% for the TA kinetics and 38%, 31% and 31% for the PL kinetics, respectively.

5.2.2 Trion fine structure & bleach magnitudes

The TA and PL kinetics both show a fast (70 ps) component having a much larger amplitude in the TA, than in the PL. Some discrepancy in the relative amplitudes is expected due to the difference in temporal resolution of the measurements. The instrument response function (IRF) of the TA measurements is about 1 ps and that of the PL measurements is approximately 55-60 ps, as shown in Figure 5.4. Thus, the temporal response of the PL measurements is significantly less than the observed 70 ps decay, allowing the fast component to be resolved. Consistent with the 70 ps decay component and the 55 ps IRF, Figure 5.3 B also shows that much of the amplitude difference persists after convolving the TA kinetics with the slower PL instrument response. A more quantitative comparison is facilitated by comparing the fitting parameters obtained when fitting each curve with its respective temporal instrument response function. This fitting shows that the fraction of the 70 ps component is about a factor 1.5 larger in the TA than in the PL kinetics. This is a crucially important result that can be interpreted in terms of the exciton spectroscopy, into which we briefly digress. The PL kinetics measure the time-dependent exciton (conduction band electron and valence band hole) population, and removal of either carrier quenches the PL. In contrast, the TA bleach recovery signal is insensitive to the presence of the hole, and the exciton TA bleach is solely attributed to conduction band state filling (see Ch 2.4 for a more detailed explanation).[10] Trapping of the conduction band electron therefore eliminates the TA bleach, while trapping of the hole has no effect on it. Because of these considerations, electron trapping will cause the TA and PL decays to have identical kinetics, and hole trapping will cause the PL to decay while

leaving the TA bleach unaffected. As long as the only excited states are simple excitons, there is no radiationless decay mechanism that will cause a larger relative amplitude decay of the TA bleach. The results in Figure 5.3 show that the fast component in the TA bleach is indeed larger than in the PL decay, and the experiment was repeated several times to ensure that the result is robust. From the above considerations we conclude that if the fast and slow components corresponded to different subensembles of the QDs in the $1S_{3/2}1S$ state having different electron trapping rates, then the relative amplitudes of the fast and slow components would be the same in the TA and PL decays. Alternatively, if the fast and slow components corresponded to different hole trapping rates then the PL kinetics would have a larger amplitude decays than the TA signal. Neither electron or hole trapping of an exciton state can result in the observed larger fast component in the TA kinetics. The conclusion is that the fast and slow components correspond to depopulation of different electronic states. We assign the slow decay to depopulation of the lowest exciton and the fast decay to depopulation of the positive trion, formed upon photoexcitation of the surface charged state.

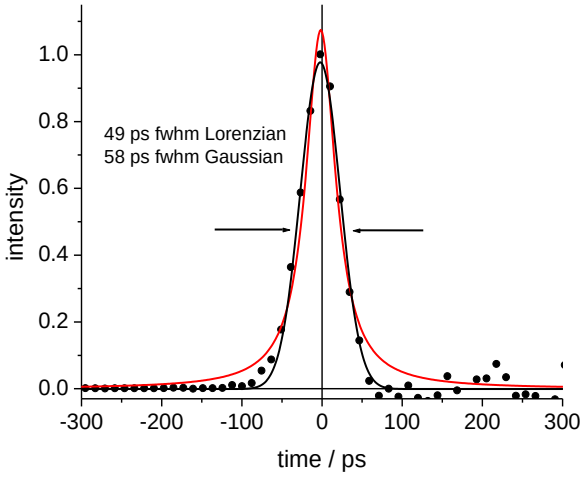

Figure 5.4. Temporal instrument response function (IRF) for the time-correlated photon counting apparatus obtained by differentiating the rise-time of an organic dye. Also shown are the fits to a Gaussian and a Lorentzian profile and the associated FWHM.

The fast decay component in the TA kinetics is reproducibly about 1.5 times the relative amplitude of the component seen in the PL. We attribute this difference primarily to trion valence band state filling. The presence of valence band state filling in the trion and its absence in the exciton can be understood in terms of the differences in the valence band fine structure. The ground state to exciton transition has an oscillator strength which we denote as $f_{gs \rightarrow X}$. The relaxed exciton has the hole primarily in the optically inactive |3/2, 3/2> state,[21] which has two results. First, PL from the relaxed exciton is not allowed and occurs only from thermal population of excited fine-structure levels. This also means that there is very little stimulated emission contribution to the TA signal. Second, because of conduction band state filling, the exciton to biexciton oscillator strength is one-half that

from the ground state; to a good approximation, $f_{X \rightarrow XX} = \frac{1}{2} f_{gs \rightarrow X}$. The conclusion is that conduction band state filling dominates the single exciton TA signal and that absorption of a single photon results in a bleach of ½ of the lowest exciton absorption.

The spectroscopy of the surface-charged QD and the positive trion is more complicated.[23] The initial transition from the surface-charged state to the trion has an oscillator strength that is comparable to the ground state to exciton transition, $f_{sc \rightarrow T} \approx f_{gs \rightarrow X}$. These are approximately equal because the initial hole in the surface charged state is in the optically inactive |3/2, 3/2> level, and the allowed |3/2, 1/2> level remains almost fully populated. This is why p-doping has little or no effect on the static absorption spectrum. In contrast, reports show that chemical and photochemical n-doping reduces the intensity of the lowest exciton transitions.[15, 24, 25] The hole states of the trion, however, are mixed by the exchange interaction and the particle anisotropy. The anisotropy associated with the presence of a charge on the surface is a large effect,[26] with the result being that all of these trion fine structure levels have allowed transitions to the surface charged state.[23] This causes several important differences between the exciton and trion spectroscopy. Probably the largest difference between the exciton and trion in the TA bleach comes from state filling considerations. Like the exciton, the trion has a conduction band electron which results in state filling. The trion also has two valence band holes, both of which are in states having allowed transitions to the conduction band. The net effect is that the trion to excited trion ($T \rightarrow T^*$) transition oscillator strength is less than that of the exciton to biexciton ($X \rightarrow XX$). This absorption diminishes the observed magnitude of the bleach in the TA signal. Due to the diminished $T \rightarrow T^*$ absorption, the trion has a larger bleach; we call this valence band state filling. Valence band state filling is the primary reason that the magnitude of the trion bleach is larger than that of the exciton.

We note that the trion radiative lifetime should be shorter than that of the exciton, and the trion to surface charged state transition should contribute a stimulated emission component to the TA spectrum. This has the effect of increasing the apparent amplitude of the bleach. The shorter radiative lifetime of the trion will also result in an increased relative trion component seen in the PL decays. These considerations affect the ratio of PL and TA bleach fast components in opposite ways. As a result, a quantitative analysis of the fast to slow component ratios in the PL and TA decays is rather complicated and will not be attempted here. We also note that because of the increased trion to surface-charged state oscillator strength, the actual fraction of the QDs that are surface charged is less than the fraction of fast component in the PL decay kinetics. We can therefore estimate that the fraction of particles that are surface charged is typically less than 30%.

The 70 ps decay time also bears on the assignment to a trion. The biexciton lifetime for 3.0 nm CdSe cores has been previously reported to be 25 ps.[16, 27-29] Deposition of a thin shell results in some delocalization of the electron, which decreases the overlap integral between the electron and hole and lengthens the biexciton Auger time to 32 ps, as shown in reference 16. These two biexciton times are confirmed in the present study and are shown in Figure 5.5. The conclusion is that the 70 ps component in the TA kinetics is about twice the biexciton time and is therefore consistent with the assignment to the Auger decay of a positive trion.

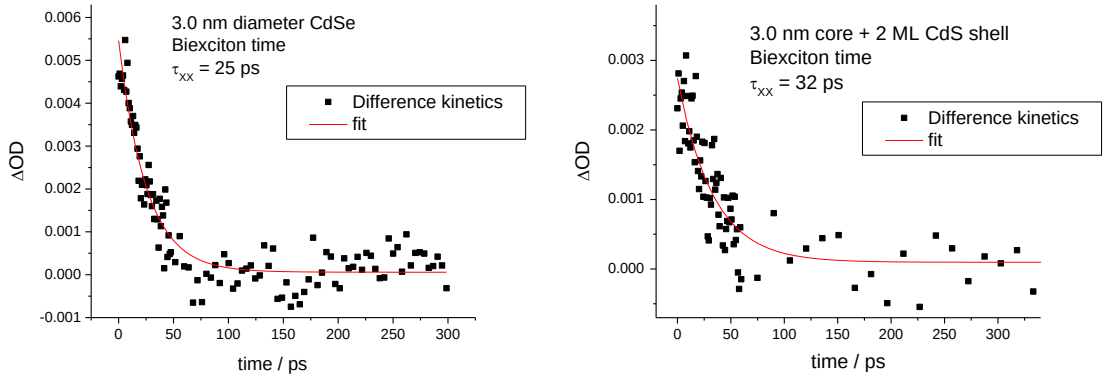

Figure 5.5. Biexciton times of 3.0 nm CdSe (left) and 3.0 nm CdSe w/2ML CdS (right) along with the single exponential fits. Decay times are extracted by normalizing the single exciton decays to the high-power decays at long times then subtracting.

5.2.3 Trion PL energies from spectral reconstruction of PL decays

Additional support for the assignment comes from the wavelength dependence of the PL decay. The particles treated with TBP and OAm show no fast decay component and essentially no detectable wavelength dependence, as shown in figure 5.6C. However, PL decay kinetics for the OAm-ligated particles show a significant wavelength dependence which decays with a time constant of 70 ps, as shown in figure 3. This is consistent with the assignment of the 70 ps component to the trion decay. Specifically, in these CdSe/CdS core/shell QDs, the holes are confined to the CdSe core, while the electron is delocalized over the entire core/shell particle. Thus, the electrostatic hole-hole repulsion is expected to be greater than the electron-hole attraction and the net effect is to raise the energy of the trion with respect to that of the exciton.[30, 31] Figure 5.5 shows that this is the case; the amplitude of the 70 ps component is larger at further blue wavelengths, indicating that the trion emission is to the blue of the exciton.

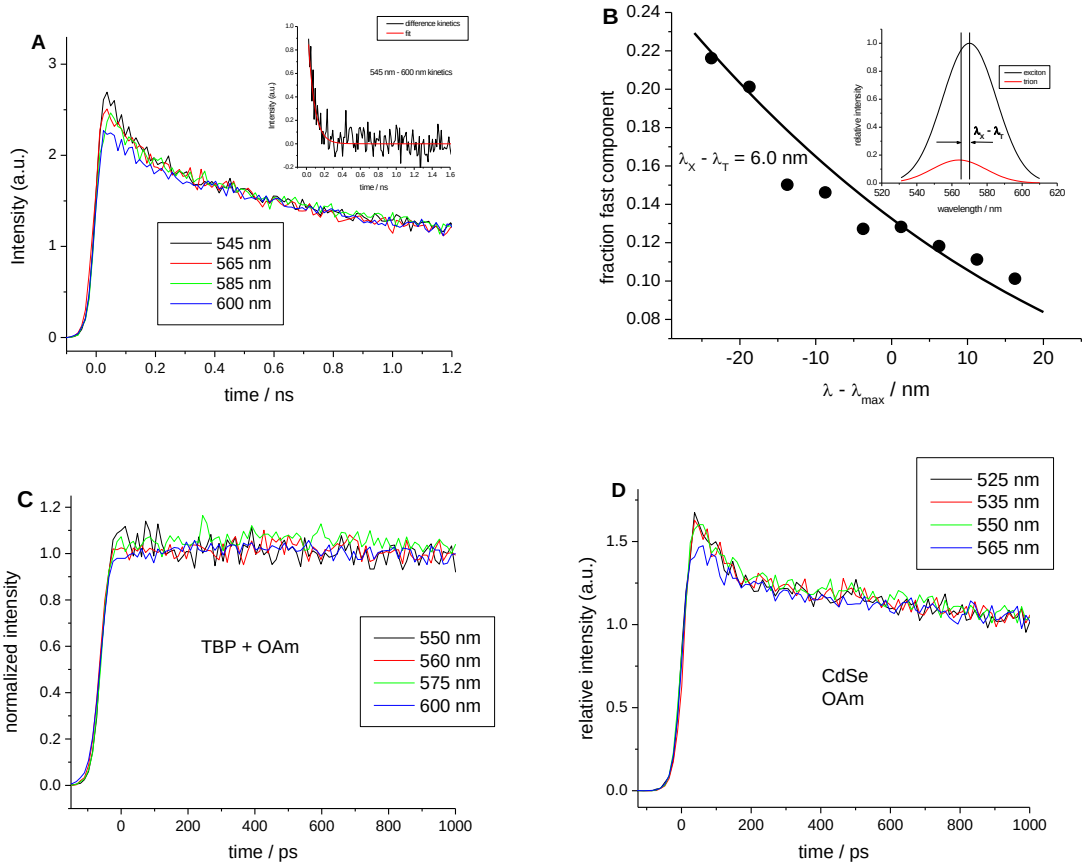

Figure 5.6. (A) Wavelength-dependent PL kinetics for CdSe/CdS QDs ligated with OAm normalized to the long-time decay component. The inset shows the 545 – 600 nm difference kinetics and a fit to a 70 ps decay. (B) Wavelength-dependent fraction of the decay corresponding to the fast component and a fit corresponding to the trion-exciton shift of 6.0 nm. The inset depicts the exciton-trion blue shift. (C) Same as (A) except that the particles are treated with both TBP and oleylamine. (D) Same as (A) but with CdSe without the CdS shell.

A quantitative estimate of the exciton to trion spectral shift can be obtained by fitting the exciton PL spectrum to a Gaussian and assuming that the trion PL spectrum is a Gaussian of the same width but blueshifted by a specified amount, as shown in the inset of Figure 5.5B. The wavelength-dependent fraction of the trion component can then be calculated and compared to the t = 0 experimental values obtained from Figure 5.5A. Taking the exciton-trion shift to be 6.0 nm, this comparison is shown in Figure 5.5B. The slope of the calculated curve in figure 2B is very sensitive to the assumed exciton-trion shift, and using this model, the uncertainty of the shift is about 1 nm. This value can be compared to the shift calculated from the electron-hole and hole-hole Coulomb interactions. Calculating the carrier wavefunctions using the effective mass approximation and methods previously published[32] and treating the Coulomb interaction as a first-order

perturbation gives a net blue shift of 26 meV, or 7.5 nm. This is in excellent agreement with the observed value of 6.0 nm.

Finally, we also note that in the case of CdSe QDs (having no shell) the electron is only slightly more delocalized than hole. In this case the electron-hole and hole-hole interactions are nearly the same and the electrostatic model predicts very little exciton-trion shift. The PL QYs of chalcogenide-rich CdSe QDs in the absence of phosphines are low (< 10%) which makes the interpretation of the relative amplitudes of fast and slow PL decay components problematic. However, with that caveat, we note that the PL kinetics do show a ~ 50 ps decay component that can be assigned to the surface charged trion, figure 5.5D. The relative amplitude of this fast component has only a slight wavelength dependence, indicating that it has very little shift from the exciton PL, as predicted by the electrostatic model.

6.3 Conclusions

CdSe and CdSe/CdS QDs are prepared in the positive trion excitonic state through thermal population of empty surface chalcogenide orbitals from the valence band. While having no effect on the linear absorption spectra, the additional hole results in fast Auger recombination upon photoexcitation, rendering the particles essentially dark. The trion is identified through the decay time, which is twice that of the biexciton time, and from the increased magnitude of the lowest exciton bleach measured by TA. Comparison of the amplitudes in the PL and TA kinetics shows that the trion absorbance is bleached by about 1.5 times that of the uncharged exciton, which is attributed to valence band state filling since transitions from both of the trion hole states to the conduction band are allowed. If the surface charge isn't completely neutralized, its presence is expected to mix the trion spin states, making all of the transitions at least partially allowed, and the increased bleach is assigned to a combination of these two effects. The CdSe/CdS trion PL is blueshifted by 6 nm compared with the excitonic PL, and the observed shift is consistent with the difference in e-e and e-h Coulomb energies calculated in the effective mass approximation using perturbation theory. Without the CdS shell, the e and h have the same spatial extent, hence the e-e and e-h Coulomb interactions are equal, and no blueshift of the trion PL is observed.

Ch 5 References

1. Nelson, H. D.; Hinterding, S. O. M.; Fainblat, R.; Creutz, S. E.; Li, X.; Gamelin, D. R., Mid-Gap States and Normal vs Inverted Bonding in Luminescent Cu+- and Ag+-Doped CdSe Nanocrystals. *J. Am. Chem. Soc.* **2017,** *139*, (18), 6411-6421.
2. Nelson, H. D.; Li, X.; Gamelin, D. R., Computational Studies of the Electronic Structures of Copper-Doped CdSe Nanocrystals: Oxidation States, Jahn–Teller Distortions, Vibronic Bandshapes, and Singlet–Triplet Splittings. *J. Phys. Chem. C* **2016,** *120*, (10), 5714-5723.
3. Norris, D. J., Electronic Structure in Semiconductor Nanocrystals: Optical Experiment. In *Nanocrystal Quantum Dots*, 2'd ed.; Klimov, V. I., Ed. CRC Press: 2010.
4. Houtepen, A. J.; Hens, Z.; Owen, J. S.; Infante, I., On the Origin of Surface Traps in Colloidal II–VI Semiconductor Nanocrystals. *Chem. Materials* **2017,** *29*, (2), 752-761.
5. Pu, C.; Peng, X., To Battle Surface Traps on CdSe/CdS Core/Shell Nanocrystals: Shell Isolation versus Surface Treatment. *J. Am. Chem. Soc.* **2016,** *138*, (26), 8134-8142.
6. Busby, E.; Anderson, N. C.; Owen, J. S.; Sfeir, M. Y., Effect of Surface Stoichiometry on Blinking and Hole Trapping Dynamics in CdSe Nanocrystals. *J. Phys. Chem. C* **2015,** *119*, 27797−27803.
7. Giansante, C.; Infante, I., Surface Traps in Colloidal Quantum Dots: A Combined Experimental and Theoretical Perspective. *J. Phys. Chem. Lett.* **2017,** *8*, (20), 5209-5215.
8. Anderson, N. C.; Hendricks, M. P.; Choi, J. J.; Owen, J. S., Ligand Exchange and the Stoichiometry of Metal Chalcogenide Nanocrystals: Spectroscopic Observation of Facile Metal-Carboxylate Displacement and Binding. *J. Am. Chem. Soc.* **2013,** *135*, 18536−18548.
9. Jasieniak, J.; Mulvaney, P., From Cd-Rich to Se-Rich - the Manipulation of CdSe Nanocrystal Surface Stoichiometry. *J. Am. Chem. Soc.* **2007,** *129*, 2841-2848.
10. Klimov, V. I., Spectral and Dynamical Properties of Multiexcitons in Semiconductor Nanocrystals. *Annu. Rev. Phys. Chem.* **2007,** *58*, 635-73.
11. Klimov, V. I., Multicarrier Interactions in Semiconductor Nanocrystals in Relation to the Phenomena of Auger Recombination and Carrier Multiplication. *Annu. Rev. Condens. Matter Phys.* **2014,** *5*, 285-316.
12. Wang, L.-W.; Califano, M.; Zunger, A.; Franceschetti, A., Pseudopotential Theory of Auger Processes in CdSe Quantum Dots. *Phys. Rev. Lett.* **2003,** *91*, 56404 - 56407.
13. Cai, X.; Martin, J. E.; Shea-Rohwer, L. E.; Gong, K.; Kelley, D. F., Thermal Quenching Mechanisms in II-VI Semiconductor Nanocrystals. *J. Phys. Chem. C* **2013,** *117*, 7902 - 7913.
14. Kim, W.; Lim, S. J.; Jung, S.; Shin, S. K., Binary Amine-Phosphine Passivation of Surface Traps on CdSe Nanocrystals. *J. Phys. Chem. C* **2010,** *114*, 1539-1546.
15. Shim, M.; Guyot-Sionnest, P., n-type Colloidal Semiconductor Nanocrystals. *Nature* **2000,** *407*, 981-983.
16. Gong, K.; Kelley, D. F., Surface Charging and Trion Dynamics in CdSe-Based Core/Shell Quantum Dots. *J. Phys. Chem. C* **2015,** *119*, 9637-9645.

17. Park, Y.-S.; Bae, W. K.; Pietryga, J. M.; Klimov, V. I., Auger Recombination of Biexcitons and Negative and Positive Trions in Individual Quantum Dots. *ACS Nano* **2014,** *8*, 7288–7296.
18. Zeng, Y.; Kelley, D. F., Excited Hole Photochemistry of CdSe/CdS Quantum Dots. *J. Phys. Chem. C* **2016,** *120*, (31), 17853-17862.
19. Zeng, Y.; Kelley, D. F., Surface Charging in CdSe Quantum Dots: Infrared and Transient Absorption Spectroscopy. *J. Phys. Chem. C* **2017,** *121*, 16657-16664.
20. Gong, K.; Martin, J. E.; Shea-Rohwer, L. E.; Lu, P.; Kelley, D. F., Radiative Lifetimes of Zincblende CdSe/CdS Quantum Dots. *J. Phys. Chem. C* **2015,** *119*, 2231-2238.
21. Efros, A. L.; Rosen, M.; Kuno, M.; Nirmal, M.; Norris, D. J.; Bawendi, M., Band-Edge Exciton in Quantum Dots of Semiconductors With a Degenerate Valence Band: Dark and Bright Exciton States. *Phys. Rev. B* **1996,** *54*, 4843 - 4856.
22. Moreels, I.; Raino, G.; Gomes, R.; Hens, Z.; Stoferle, T.; Mahrt, R. F., Band-Edge Exciton Fine Structure of Small, Nearly Spherical Colloidal CdSe/ZnS Quantum Dots. *ACS Nano* **2011,** *5*, 8033 - 8039.
23. Shabaev, A.; Rodina, A. V.; Efros, A. L., Fine Structure of the Band-Edge Excitons and Trions in CdSe/CdS Core/Shell Nanocrystals. *Phys. Rev. B* **2012,** *86*, 205311-205325.
24. Tsui, E. Y.; Carroll, G. M.; Miller, B.; Marchioro, A.; Gamelin, D. R., Extremely Slow Spontaneous Electron Trapping in Photodoped n-Type CdSe Nanocrystals. *Chem. Mater.* **2017,** *29*, 3754-3762.
25. Shim, M.; Shilov, S. V.; Braiman, M. S.; Guyot-Sionnest, P., Long-Lived Delocalized Electron States in Quantum Dots: A Step-Scan Fourier Transform Infrared Study. *J. Phys. Chem. B* **2000,** *104*, 1494.
26. Sercel, P. C.; Shabaev, A.; Efros, A. L., Photoluminescence Enhancement through Symmetry Breaking Induced by Defects in Nanocrystals. *Nano Lett.* **2017,** *17*, (8), 4820-4830.
27. Robel, I.; Gresback, R.; Kortshagen, U.; Schaller, R. D.; Klimov, V. I., Universal Size-Dependent Trend in Auger Recombination in Direct-Gap and Indirect-Gap Semiconductor Nanocrystals. *Phys. Rev. Lett.* **2009,** *102*, 177404-177407.
28. Klimov, V. I.; McGuire, J. A.; Schaller, R. D.; Rupasov, V. I., Scaling of Multiexciton Lifetimes in Semiconductor Nanocrystals. *Phys. Rev. B* **2008,** *77*, 195324 - 195324.
29. Pandey, A.; Guyot-Sionnest, P., Multicarrier Recombination in Colloidal Quantum Dots. *J. Chem. Phys.* **2007,** *127*, 111104 - 111107.
30. Franceschetti, A.; Zunger, A., Optical Transitions in Charged CdSe Quantum Dots. *Phys. Rev. B* **2000,** *62*, R16287.
31. Troparevsky, M. C.; Franceschetti, A., Radiative Recombination of Charged Excitons and Multiexcitons in CdSe Quantum Dots. *Appl. Phys. Lett.* **2005,** *87*, 263115-263117.
32. Cai, X.; Mirafzal, H.; Nguyen, K.; Leppert, V.; Kelley, D. F., The Spectroscopy of CdTe/CdSe type-II Nanostructures: Morphology, Lattice Mismatch and Band-Bowing Effects. *J. Phys. Chem. C* **2012,** *116*, 8118 - 8127.

33. Pu, C.; Zhou, J.; Lai, R.; Niu, Y.; Nan, W.; Peng, X., Highly Reactive, Flexible Yet Green Se Precursor for Metal Selenide Nanocrystals: Se-Octadecene Suspension (Se-SUS). *Nano Research* **2013,** *6*, 652-670.
34. Nan, W.; Niu, Y.; Qin, H.; Cui, F.; Yang, Y.; Lai, R.; Lin, W.; Peng, X., Crystal Structure Control of Zinc-Blende CdSe/CdS Core/Shell Nanocrystals: Synthesis and Structure-Dependent Optical Properties. *J. Am. Chem. Soc.* **2012,** *134*, 19685−19693.
35. Jasieniak, J.; Smith, L.; van Embden, J.; Mulvaney, P.; Califano, M., Re-examination of the Size-Dependent Absorption Properties of CdSe Quantum Dots. *J. Phys. Chem. C* **2009,** *113*, 19468 - 19474.
36. van Embden, J.; Jasieniak, J.; Mulvaney, P., Mapping the Optical Properties of CdSe/CdS Heterostructure Nanocrystals: The Effects of Core Size and Shell Thickness. *J. Am. Chem. Soc.* **2009,** *131*, 14299 - 14309.
37. Gong, K.; Kelley, D. F., Lattice Strain Limit for Uniform Shell Deposition in Zincblende CdSe/CdS Quantum Dots. *J. Phys. Chem. Lett.* **2015,** *6*, 1559-1562.

Ch 6

Spectroscopic Manifestations of Hole Trapping in CdSe Nanoplatelets

Abstract

Transient absorption (TA) spectra of 4.5-monolayer thick CdSe nanoplatelets are analyzed in terms of the heavy hole electronic structure. The nanoplatelets are treated with 4-methylbenzenethiol (MBT), a hole acceptor, and the spectra and kinetics with and without MBT are compared in order to assess the role of valence band populations in the TA spectra. Analogous TA spectra are obtained for spherical CdSe quantum dots, showing that the presence of a valence band hole produces qualitatively different behavior in the spherical *vs.* 2D nanoparticle cases. In quantum dots, the exciton to biexciton transition is fully allowed and has close to the same energy and oscillator strength as the negatively charged particle to negative trion transition, which leads to the absence of any hole dynamics being seen in TA measurements. In the case of the platelets, the large shape anisotropy splitting lifts the light/heavy hole degeneracy, causing the exciton to biexciton transition from the lowest hole level to be forbidden. The larger spatial extent of the excitonic wavefunctions also reduces the exchange interaction, leading to significant population of the bright exciton state. As a result, stimulated emission significantly contributes to the amplitude of the heavy hole bleach band, and the amplitude of the photoinduced absorption of the heavy hole transition is sensitive to both conduction band and valence band state filling.

6.1 Introduction

Transient absorption (TA) spectroscopy is commonly used to study the excited states of both molecules and nanostructures. The simplest case is the low power limit, where all of the molecules or nanostructures absorb either zero or one photon. Transient absorption spectra are typically displayed as difference spectra, $A(\lambda,t) - A_0(\lambda)$, where $A_0(\lambda)$ is the static absorption spectrum. Displayed this way, only the species that have absorbed a single photon contribute to the low power spectrum. Generally, three factors contribute to TA spectra: loss of ground state absorption, excited state absorption, and stimulated emission. In the case of quantum dots (QDs) at wavelengths close to the lowest exciton ($1S_{3/2} \rightarrow 1S_e$) absorption maximum, these contributions correspond to loss of the ground state to exciton absorption ($gs \rightarrow X$), photoinduced absorption by the exciton to produce a biexciton (PA, $X \rightarrow XX$) and exciton to ground state stimulated emission (SE, $X \rightarrow gs$). The relative contributions of each of these transitions determine the magnitudes of the different features in the TA spectrum. The QD exciton has several low energy angular momentum fine structure states, and accounting for these states is critical in analyzing their TA spectra. At room temperature and at times longer than a few picoseconds, the exciton has relaxed to a thermal equilibrium of these states. It is the relative populations and oscillator strengths (both $X \rightarrow XX$ and $X \rightarrow gs$) of the fine structure states that determine the wavelength-dependent PA and SE contributions to the overall TA spectrum. Loss of the ground state absorption dominates the TA spectrum of QDs and a "bleach" feature near the lowest energy static absorption maximum is typically observed.

The situation is well understood in the case of spherical CdSe QDs and will be addressed here as a comparison with the two-dimensional CdSe nanoplatelets (NPLs). The CdSe valence band is split into J = 3/2 and J = 1/2 states, resulting in the lowest energy exciton state being optically inactive, the so-called "dark exciton".[1, 2] There are several allowed excitonic states at slightly higher energy (tens of meV) that are populated at room temperature. Thermal population of these states gives rise to the strong photoluminescence that is observed from many types of II-VI QDs, but because much of the population is in the dark levels, the radiative lifetime is typically much longer than one calculates from the integrated extinction coefficients.[3] This has two important implications for the TA spectra of QDs. First, having most of the population in the dark states causes there to be only a minor contribution due to SE. Second, because the lowest conduction band state is nondegenerate (other than the spin degeneracy of 2), absorption of a photon leaves this level half filled. Thus, half of the subsequent valence band to conduction band transitions are not possible. This "state filling" effect reduces the intensity of transitions to the lowest conduction band level by a factor of approximately two.[4] The X → XX transitions are also slightly red shifted from the corresponding gs → X transitions. This is due to the Coulomb interaction between the nascent and existing excitons (Stark shift) often referred to as the biexciton binding energy or simply as the biexciton effect.[4] This shift is typically much smaller than the inhomogeneous width of the gs → X absorption band and has only a small effect on the relaxed TA spectrum. The conclusion is that the intensity of the X → XX transition in the PA spectrum is largely determined by conduction band state filling and is about one-half that of the gs → X transition.

The electronic structure, and in turn, the spectroscopy of NPLs is similar to that of spherical QDs but has important differences. The main difference is that the shape anisotropy of the NPL splits the heavy hole (HH) and light hole (LH) valence band states, removing the orbital angular momentum degeneracy of the hole states. The NPLs also lack much of the quantum confinement along the lateral dimensions compared to typical QDs, causing the electron and hole wavefunctions to have differing spatial extents and hence smaller electron-hole exchange interactions. The result of these two considerations is that the lowest energy (HH) exciton has only two fine structure levels: the lowest energy optically forbidden state and an allowed state at about 5 meV higher energy.[5] This 5 meV splitting is small compared to room temperature thermal energy (26 meV), giving room temperature Boltzmann populations of 55% and 45% for the dark and bright states, respectively. It follows that the NPL TA spectra will have a significant SE component. In addition, the large LH/HH splitting changes which transitions affect the PA spectrum in the region of the lowest energy gs →X bleach. This is because in general, the X → XX transition from the lowest energy excitonic state (the $J_z \pm 2$ state in spherical QDs) involves excitation from the manifold of LH states.[6] In the case of spherical particles, the LH/HH splitting is small (~ 40 meV) compared to the inhomogeneous broadening. As a result, the HH and LH bands are completely spectrally overlapped, and the transitions from the $J_z \pm 2$ state contributes to the PA at the bleach wavelength. In contrast, the NPL LH band is spectrally separated from the HH bleach band, so transitions involving the LH do not enter into low energy TA spectra. As we further discuss below, the result is that the NPL PA intensity depends on the valence band hole population, i.e., the TA spectrum is sensitive to both conduction and valence band state filling.

The two-dimensional NPL morphology also affects the exciton energetics and spectroscopy in other ways. In these very thin platelets, the exciton is partially surrounded by the lower dielectric constant organic medium, resulting in a large Coulomb interaction and Stark shift of the biexciton. This effect goes opposite that of the reduced Coulomb interaction associated with the spatially diffuse electron and hole wavefunctions, making comparison of the Stark shift with the spherical case difficult. In addition, the larger lateral dimensions of the NPL reduces the splitting between excitons of the same Bloch but different envelope functions, i.e., different lateral excited states. Population of these slightly higher energy excited states can play an important role in the NPL TA spectroscopy. In contrast, the next highest envelope state in the spherical QDs presented here is ~ 100 meV higher in energy,[7] so thermal population of these states at room temperature is negligible. With these considerations, we model TA spectra of 4.5 ML CdSe NPLs in terms of ground state depletion, PA and SE. These TA spectra are compared to those taken from identical NPLs treated with 4-methylbenzenethiol, MBT, a known hole acceptor.[8] This modeling uses only the quantum mechanics of the above considerations, the static absorption spectra and known energetic parameters from the literature. The only adjustable parameter in the model is the biexciton interaction energy which is extracted from the modeling procedure.

Previous studies of NPL TA spectroscopy have yielded what at first appear to be inconsistent results. Wu et al.[9] attach an electron acceptor, methyl viologen, to 5 ML NPLs and examine the kinetics of electron transfer and the TA bleach. They find that electron transfer eliminates the observed bleach. From this observation these authors conclude that the bleach is entirely due to conduction band state filling, just as it is in spherical QDs; the presence of the valence band hole does not affect the magnitude of the bleach. In contrast, Kunneman et al.[10] measure TA spectra of 5 ML NPLs and from a combination of light and heavy hole bleach kinetics argue that some fraction of the NPLs have surface defects that act as hole traps. With this assignment, the TA kinetics show that removal of the hole decreases the magnitude of the bleach by about 30%. In this chapter, the static and TA spectroscopy of 4.5 ML (4 selenium and 5 cadmium layers) NPLs are analyzed. One of the goals of the present study is to resolve the above apparent discrepancy and to ascertain the role of valence band population in the NPL TA spectra.

6.2 Results and Discussion

6.2.1 Static absorption spectral fitting

The static absorption spectra of 4.5 monolayer NPL are shown in Figure 6.1 along with the corresponding TEM image. The TEM indicates that these NPL have lateral dimensions of 7.0 ± 0.5 nm x 26 ± 3 nm. The lowest energy (HH and LH) region of the static spectrum is fit to a sum of four Gaussians in 6.1, and the fitting parameters are given below in Table 6.1.

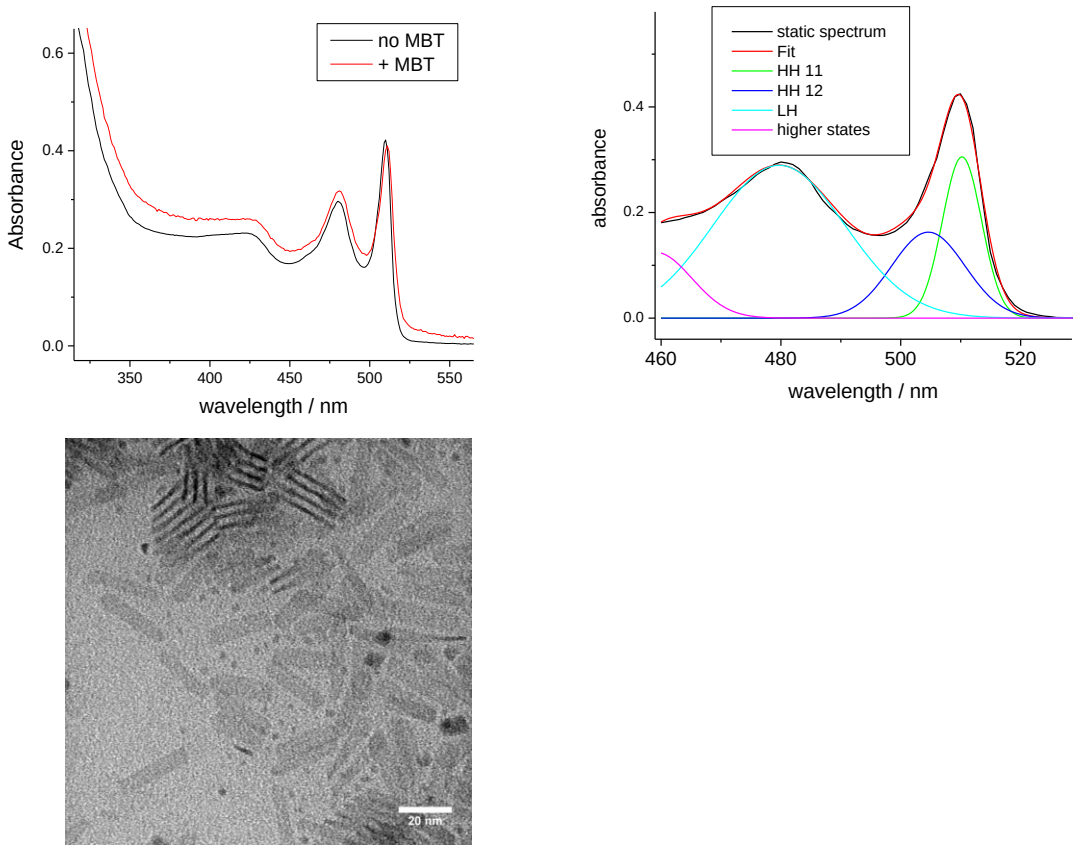

Figure 6.1 Static absorption spectra of 4.5 ML CdSe nanoplatelets before and after addition of 4-methylbenzenethiol (MBT) (top left), peak fitting of the static spectrum without MBT (right), and a TEM image of the untreated sample (bottom left).

Table 6.1. Fitting parameters for the static absorbance spectrum before treatment with MBT shown in Figure 6.1

	Wavelength (nm)	FWHM (nm)	Relative area
Static spectrum			
HH 1,1	509.5	7.7	1.0
HH 1,2	502.7	14.5	1.0
LH	480.4	21.8	2.5
Higher states	458	23.5	1.6

These fit to the static spectrum in Figure 6.1 is derived by approximating the nanoplatelet as simple particle-in-a-box functions. The electron-hole coulombic interaction is sufficiently large that the electron and hole motions are coupled, and one has to consider quantum confinement of the excitonic states rather than independent electron and hole states.[13-16] The lowest energy state corresponds to the exciton having n_x, $n_y = 1$, where x and y refer to the short and long lateral dimensions, respectively. The next state corresponds to $n_x = 1$, $n_y = 2$, a p-like state. We will refer to the lowest energy s-like and the higher energy p-like states by their particle-in-a-box (n_x,n_y) quantum numbers, (1,1) and (1,2), respectively. Recent studies by Achtstein et al.[17] indicate that for comparable size nanoplatelets the (1,2) exciton state is about 30 meV higher in energy than the (1,1) state, which is consistent with particle-in-a-box energy levels for the known electron and hole effective masses.[11]

Because the lateral dimensions of the platelet are greater than the excitonic radii, the spatial extents of the electron and hole will differ depending on their effective masses. The exact spatial dependence of the excitonic wavefunctions is difficult to know precisely, so we make the simplifying assumption that the overlap integral for the first excited lateral state is the same as for the band edge exciton. This gives a physical basis for the constraints placed on the fitting procedure, i.e. that the integrated area of both peaks are equal. These spectral components will be used to analyze the TA spectra in the discussion that follows. Also shown in figure 6.1 is the absorption spectrum of the same NPLs following addition of MBT, which shifts the spectrum approximately 1 nm to the red.

6.2.2 Hole trapping kinetics in NPL vs QD

Photoluminescence (PL) decay and TA (bleach recovery) kinetics for these NPLs are shown in figure 6.2. Both the PL and TA show a significant decay over the first nanosecond. These decays show a fast ~150 ps component previously assigned as hole trapping, and the slower ~ 5 - 6 ns component is assigned to the radiative recombination rate.[10, 18] Normalizing the TA and PL at t = 0 reveals that the hole trapping component has a larger amplitude in the PL than in the TA kinetics, and that the difference in PL and TA fast component amplitudes seen here is consistent with that reported in reference 10.

A sample of NPLs was treated with a hole acceptor in order to determine the role of valence band holes in the TA spectra and kinetics. 4-methylbenzenethiol (MBT) is chosen because it rapidly and efficiently traps holes while not affecting the NPL stability or solubility. The presence of MBT results in essentially complete quenching of the PL within the 55 ps response time of the PL experiment, indicating complete hole transfer on that timescale. The key result from Figure 6.2 is that the addition of MBT reduces the magnitude of the TA bleach to about 73% of its initial value.

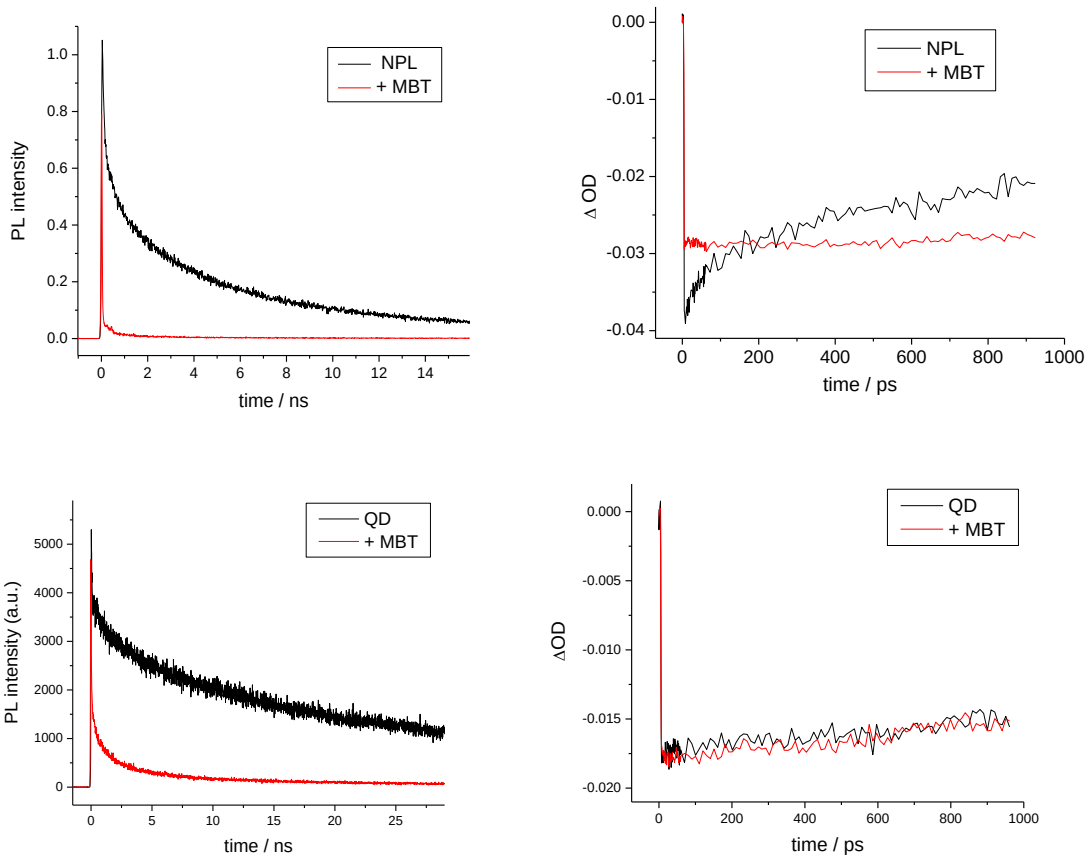

Figure 6.2 PL decay kinetics measured at the peak of the PL band for 4-ML CdSe nanoplatelets (top left) and for 3.2 nm diameter QD (bottom left). Lowest exciton bleach kinetics for NPL (top right) and QD (bottom right) before and after treatment with MBT.

This result conclusively shows that the magnitude of the bleach associated with the NPL exciton depends on both the conduction band electron and the valence band hole. The magnitude of the bleach reduction is in excellent agreement with the ratio of bleach intensities before and after hole trapping reported in reference 10. We also note that the presence of MBT results in TA kinetics that are essentially flat over the first nanosecond. The lack of a significant decay on this timescale reflects the slow radiative and nonradiative charge recombination of conduction band electrons with the holes transferred to the adsorbed MBT.

For comparison, the PL and TA kinetics of 3.2 nm diameter spherical QDs with and without MBT are also shown in Figure 6.2. In this case, carrier trapping processes can be assigned by comparing TA and PL kinetics, making use of the fact that hole dynamics of spherical QDs are not probed by TA measurements.[19] Figure 6.2 shows that the presence of MBT rapidly quenches the PL but has no measurable effect on the amplitude of the bleach or the TA kinetics. This result is consistent with rapid hole transfer from spherical QDs to adsorbed MBT and the magnitude of the TA bleach being independent of the valence band hole.

6.2.3 Modeling of the NPL TA spectra

Further understanding of the spectroscopic differences between NPLs and QDs comes from an analysis of the NPL TA spectra. Figure 6.3 shows the TA spectra for the NPLs obtained for the 3 – 30 ps time window, obtained with and without adsorbed MBT and scaled to the t = 0 amplitude. In addition to the bleach, the TA spectra show a PA feature strongly overlapping, but slightly to the red of the static absorption maximum. Comparison of the spectra with and without MBT shows that the magnitude of the bleach decreases while the amplitude of the positive red absorption feature increases upon hole transfer. In the analysis that follows, we calculate TA spectra based on the model presented in figure 6.4.

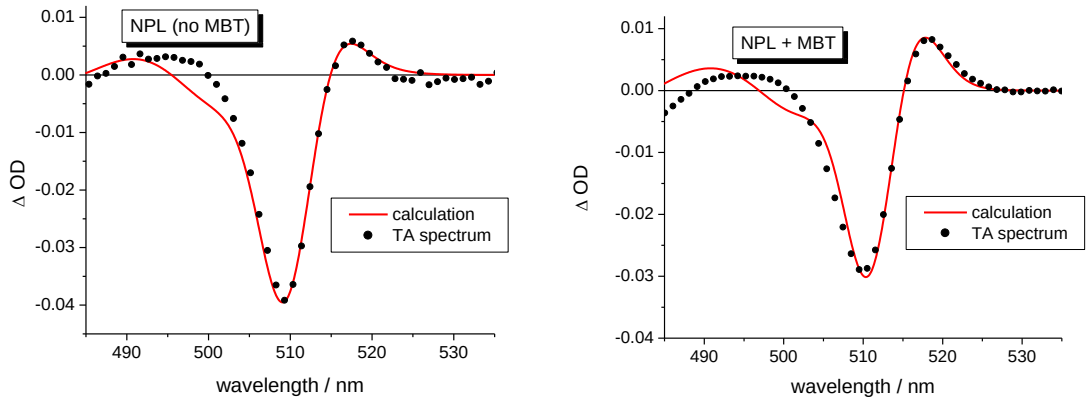

Figure 6.3. Transient absorption spectra of NPLs without (left) and with (right) MBT averaged from 3 to 30 ps, and scaled to the t = 0 intensities. Also shown are fits using the parameters in table 6.2.

The spectral components in Figure 6.1 are used to calculate the ground state depletion, the photo-induced absorption (a shifted absorption spectrum which partially replaces the ground state spectrum) and the stimulated emission contributions to the TA spectra. This is done for the presence and absence of a valence band hole, as follows. The ground state depletion component of the TA spectrum is calculated in E6.1 and is proportional to the static spectrum.

$$B(\lambda) = -const \cdot A_0(\lambda) = -const \cdot \sum_i A_i(\lambda) \qquad \text{E6.1}$$

where $A_i(\lambda)$ is the spectrum of each of the spectral components, the index runs over the four components in the fit of the static spectrum, and the constant is proportional to the fraction of platelets that absorb a photon.

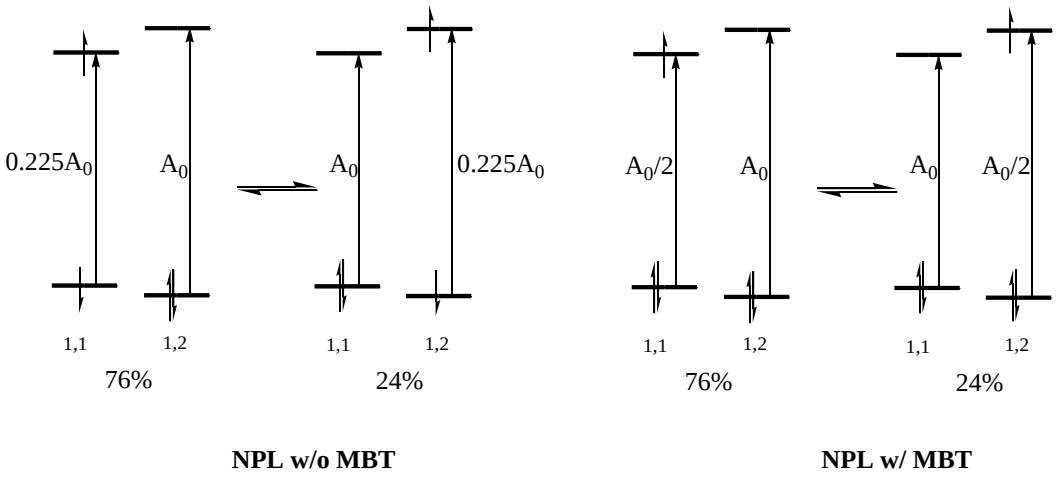

Figure 6.4. Intensities of the (1,1) and (1,2) transition in the PA spectrum without (left) and with (right) the hole acceptor MBT. Intensities are calculated from the 30 meV splitting between the two states, giving 76% population of the (1,1) state and 24% population of the (1,2) state.

Calculation of the intensities of each of the static components in the PA is somewhat more complicated. Due to the relatively strong electron-hole coulombic coupling, the electronic structure of the different laterally excited envelope functions must be considered in terms of the excitonic states, rather than individual electron and hole states.[1, 13-15] The PA spectrum is calculated in terms of the spectral components in Figure 6.1, and in general, is given by E6.2, where the A_i spectral components are the same as in equation 6.1 and Δ is the biexciton spectral shift.

$$PA(\lambda) = \sum_i f_i A_i(\lambda - \Delta) \qquad \text{E6.2}$$

There are two contributions to the intensity factors, f_i corresponding to when the exciton is in either the (1,1) or (1,2) lateral states. These factors are calculated for each of the transitions from several simple considerations, as indicated in figure 6.4. An important consideration in this calculation is the energetic splitting between the (1,1) and (1,2) lateral excited states; the s- and p-state splitting, which determines their Boltzmann populations. Taking the separation of these states to be 30 meV[17] gives fractions of 76% for the (1,1) and 24% in the (1,2). Only these two states are considered because the higher energy lateral states are thermally inaccessible at room temperature. Another important consideration is the role of exciton spin states and the magnitude of the dark-bright splitting. The dark-bright splitting has been measured to be about 5 meV for comparable NPLs.[5] With a Boltzmann distribution at room temperature, about 45% of the population is in the bright state. When the exciton is in the (1,1) state, the X $\rightarrow$ XX PA corresponds to only one valence band electron in this lateral state and its transition to the conduction band is allowed only 45% of the time (corresponding to the fraction of platelets in the singlet state). The net result is that when the exciton is in the (1,1) state (76% of the time) the intensity of the (1,1) component (HH 1,1 in Figure 6.1) in the PA spectrum is (0.45)/2 = $0.225A_{11}$. With the (1,2) state occupied, the contribution of the (1,1) transition to the PA is comparable to

that from the ground state. In terms of equation 6.2, this means that f_1 = (0.76)(0.225) + (0.24)(1.0) = 0.41, as indicated in figure 6.4. The higher energy transitions are also not affected by the exciton and the *f* factors for these spectral features are taken to be unity. Analogous considerations apply when the exciton is in the (1,2) state. Considering the three lowest energy spectral components in Figure 6.1, the net result of the summation in equation 2 is:

$$PA(\lambda) = [(0.45)(0.76)/2 + 0.24]\,A_{11}(\lambda+\Delta) + [(0.45)(0.24)/2 + 0.76]\,A_{12}(\lambda+\Delta) + A_{LH}(\lambda+\Delta) \quad \text{E6.3}$$

The stimulated emission contributions to the transient absorption spectra are calculated from similar considerations. The fraction of the population in the emissive singlet component of the (1,1) exciton state is (0.76)(0.45) = 0.34, and the degeneracy of this transition is 1/2 that of the gs → X transition. The net result is that the magnitude of the (1,1) stimulated emission is $(0.34A_{11})/2 = 0.17\ A_{11}$, and this component is added to the (1,1) bleach component given in equation 1. Similarly, for the (1,2), the magnitude of the stimulated emission is $(0.24A_{12})(0.45)/2 = 0.06\ A_{12}$. Thus, the effect of including stimulated emission is that the net bleach bands for the (1,1) and (1,2) transitions in the NPL TA spectrum have magnitudes of $1.17\ A_{11}$ and $1.06\ A_{12}$, respectively. We note that the PA spectrum calculated from eqn. 6.3 and the SE intensities both depend on the Boltzmann probabilities of (1,1) and (1,2) occupancy. These probabilities depend on the lateral state energies and hence the NPL lateral dimensions. However, there is only a small fraction (24% in this case) of the population in the higher energy (1,2) state and it is only slightly spectrally separated from the (1,1) state. As a result, the total calculated PA and SE components are close to what are calculated for the lowest excited state and the calculated TA spectrum is only weakly dependent on NPL lateral dimensions.

Somewhat different considerations apply to calculating the TA spectrum in the case where MBT is present and the valence band hole has transferred. In this case, there is no stimulated emission and the intensities of the (1,1) and (1,2) transitions in the PA spectrum are determined solely from their Boltzmann populations and conduction band state filling. We make the approximation of taking this energetic separation to be the same as in the case of the exciton, 30 meV. This is a reasonable approximation since most of the exciton quantum confinement is in the electron. As before, this gives 76% of the population in the (1,1) state and 24% in the (1,2) state. The conduction band state filling reduces the intensities of each of these transitions by a factor of two, as depicted in figure 6.4. Thus, the PA contribution for the case of the trapped hole is given by E6.4,

$$PA(\lambda) = const \cdot \sum_i f_{MBT\,i} A_i(\lambda - \Delta_e) \quad \text{E6.4}$$

where Δ_e is the biexciton spectral shift resulting from the electron and transferred hole. Using arguments analogous to those giving equation 6.3, the net photoinduced absorption is given by E6.5. As in the exciton case, the *f* factors for the higher energy spectral features are taken to be unity.

$$PA(\lambda) = [(0.76)/2 + 0.24]\,A_{11}(\lambda+\Delta_e) + [(0.24)/2 + 0.76]\,A_{12}(\lambda+\Delta_e) + A_{LH}(\lambda+\Delta_e) \quad \text{E6.5}$$

The relative magnitudes of the contributions from bleach, PA, and SE to the TA spectra with and without MBT are summarized in Table 6.2. As mentioned above, the only adjustable parameters in this model are the biexciton binding energies, Δ and Δ_e for the cases where the hole is present and where it has been transferred, respectively. Taking the spectral components in Figure 6.1B, the *f* factors calculated above (see table 6.2), and the binding energies $\Delta = 2.0 \pm 0.2$ nm (9.5 ± 1.2 meV) and $\Delta_e = 1.5 \pm 0.2$ nm (7.1 ± 1.2 meV) gives the calculated spectra shown in figure 6.3. The calculated curves show that this very simple model works well for wavelengths > 505 nm but fails to capture the complexity of the spectra at bluer wavelengths. The failure at shorter wavelengths is most likely due the presence of several other transitions buried under the LH transition.

Table 6.2. Fitting parameters for the transient absorption spectra of the platelets with and without MBT shown in Figure 6.3.

	Wavelength (nm)	FWHM (nm)	Relative amplitude
TA spectrum (no MBT)			
1,1 bleach + SE	509.5	7.7	- 1.17
1,2 bleach + SE	502.7	14.5	- 1.06
1,1 PA	511.5	7.7	+ 0.42
1,2 PA	504.7	14.5	+ 0.81
TA spectrum (with MBT)			
1,1 bleach + SE	510.6	7.7	- 1.0
1,2 bleach + SE	504.1	14.5	- 1.0
1,1 PA	512.1	7.7	+ 0.63
1,2 PA	505.6	14.5	+ 0.88

Several aspects of the calculated TA spectra are notable. The larger PA feature and the smaller bleach observed when the hole is transferred are quantitatively reproduced by this model. This is because valence band state filling results from the fact that when the hole is present, the population is divided between states with allowed and forbidden absorption transitions. In contrast, following hole removal the entire population is in the doublet state, and the doublet-doublet transition is fully allowed. Thus, the intensity factors for the PA contributions are greater when MBT is present. We note that this part of the analysis assumes that the transferred holes are decoupled from the conduction band electron, as has been shown in previous studies.[8]

The values of the biexciton binding energies are much smaller than what has previously been reported. We suggest that the difference comes about from the fitting procedure.[20, 21] We model the HH region of the spectrum in terms of two transitions separated by 30 meV, the (1,1) and (1,2) transitions. This spectral region can be modeled in terms of a continuum of lateral transitions.[22] However, given the spacing between the two lowest transitions, modeling in terms of a continuum is a poor approximation for platelets of these lateral dimensions. We note that modeled in this fashion, the width of the lowest energy transition is much smaller than if one were to model in terms of a continuum of lateral states, which leads to a smaller shift being necessary shift in order to fit the TA spectra. The small value of Δ and narrow absorption features cause the bleach and PA bands to overlap significantly at the bleach maximum, which can confuse analysis of the TA kinetics. Since hole trapping eliminates the SE while increasing the PA, one cannot analyze the ground state population recovery based solely on the kinetics of the bleach maximum. Contributions of the different bands to the overall TA spectra change with the relative populations of NPLs having a single exciton or a trapped or transferred carrier, and this can confuse the interpretation of these kinetics.

The above model allows us to consider the spectral and kinetic changes that occur when an electron is trapped or transferred. It is important to recall that the effective mass of the heavy hole is very large, 0.9 of the free electron mass.[11] Due to the large effective mass and the large lateral dimensions, a free hole has many energetically accessible lateral states, which is fundamentally different than the case where a tightly-bound electron-hole pair is forming an exciton. In the absence of any electric fields from the ligands or the transferred electron, the hole particle-in-a-box energy levels give a room temperature partition function of 5.3 for the lateral dimensions of these NPLs. Thus, only about 18% of the holes are in the (1,1) state and there is a minimal contribution to valence band state filling. Alternatively, when the electron is trapped or transferred to an adjacent acceptor, the valence band hole can have a comparatively large coulombic interaction with the electron. Diagonalization of the hole wavefunction under the perturbation of the electric field of the localized electron will result in a superposition of these lateral states that partially localizes the hole. The coefficient of the delocalized hole particle-in-a-box (1,1) state in this expansion will be small if the hole is localized, so the absorption of the (1,1) transition is close to the same as it would be if the NPL is in the uncharged ground state. Both possibilities give the same conclusion – there will be only a very small bleach, as reported in reference 9. Another possibility is that the coulombic interaction with the conduction band electron stabilizes the valence band hole, and in the absence of this stabilization, the valence band hole traps at an edge or surface defect. In any of these cases, the crucial point is that the nature of the hole wave function is different when the electron trapped compared to when it is not. When the hole is localized, it has little effect on the PA spectrum, and when it is delocalized, it contributes to valence band state filling.

6.3 Conclusion

A trapped electron and partially localized hole will still produce an electric field that affects the TA spectrum. In the simplest approximation, there is no SE and the PA will simply be a shifted and perhaps broadened static spectrum. The combination of the bleach and the PA will produce a derivative-like TA spectrum that will have very little intensity at the wavelength static maximum and therefore little or no apparent bleach, as is exhibited in the longer delay time spectra after all the electrons have trapped in reference 9. We have also obtained TA spectra in the presence of different types of adsorbed electron acceptors. We find that accurately modeling the time-dependent spectra with the simple methods described above is rather complicated. Specifically, electron transfer to the adsorbed acceptor occurs on the same timescale as hole trapping to edge defects in some fraction of the NPLs, making it very difficult to determine relative subpopulations of platelets with a single exciton, a transferred electron, or a trapped hole. Studies aimed at simplifying these complexities are currently underway and will be reported in later papers.

Acknowledgements

This material is based upon work supported by the U.S. Department of Energy, Office of Science, Office of Basic Energy Sciences, under award number DE-SC0018307. The authors would also like to thank Dr. Rui Tan and Prof. Son Nguyen for their assistance with obtaining the TEM images.

Ch 6 References

1. Efros, A. L.; Rosen, M.; Kuno, M.; Nirmal, M.; Norris, D. J.; Bawendi, M., Band-Edge Exciton in Quantum Dots of Semiconductors With a Degenerate Valence Band: Dark and Bright Exciton States. *Phys. Rev. B* **1996,** *54*, 4843 - 4856.
2. Nirmal, M.; Dabbousi, B. O.; Bawendi, M. G.; Macklin, J. J.; Trautman, J. K.; Harris, T. D.; Brus, L. E., Fluorescence Intermittency in Single Cadmium Selenide Nanocrystals. *Nature* **1996,** *383*, 802.
3. Gong, K.; Zeng, Y.; Kelley, D. F., Extinction Coefficients, Oscillator Strengths, and Radiative Lifetimes of CdSe, CdTe, and CdTe/CdSe Nanocrystals. *J. Phys. Chem. C* **2013,** *117*, 20268-20279.
4. Klimov, V. I., Spectral and Dynamical Properties of Multiexcitons in Semiconductor Nanocrystals. *Annu. Rev. Phys. Chem.* **2007,** *58*, 635-73.
5. Shornikova, E. V.; Biadala, L.; Yakovlev, D. R.; Sapega, V. F.; Kusrayev, Y. G.; Mitioglu, A. A.; Ballottin, M. V.; Christianen, P. C. M.; Belykh, V. V.; Kochiev, M. V.; Sibeldin, N. N.; Golovatenko, A. A.; Rodina, A. V.; Gippius, N. A.; Kuntzmann, A.; Jiang, Y.; Nasilowski, M.; Dubertret, B.; Bayer, M., Addressing the exciton fine structure in colloidal nanocrystals: the case of CdSe nanoplatelets. *Nanoscale* **2018,** *10*, 646-656.
6. Rodina, A. V.; Efros, A. L., Band-edge Biexciton in Nanocrystals of Semiconductors with a Degenerate Valence Band. *Phys. Rev. B* **2010,** *82*, 125324-125337.
7. Norris, D. J.; Bawendi, M. G., Measurement and assignment of the size-dependent optical spectrum in CdSe quantum dots. *Phys. Rev. B* **1996,** *53*, 16338 - 16346.
8. Grenland, J. J.; Maddux, C. J. A.; Kelley, D. F.; Kelley, A. M., Charge Trapping versus Exciton Delocalization in CdSe Quantum Dots. *J. Phys. Chem. Lett.* **2017,** *8*, 5113-5118.
9. Wu, K.; Li, Q.; Du, Y.; Chen, Z.; Lian, T., Ultrafast exciton quenching by energy and electron transfer in colloidal CdSe nanosheet-Pt heterostructure. *Chem. Sci.* **2015,** *6*, 1049-1054.
10. Kunneman, L. T.; Schins, J. M.; Pedetti, S.; Heuclin, H.; Grozema, F. C.; Houtepen, A. J.; Dubertret, B.; Siebbeles, L. D. A., Nature and Decay Pathways of Photoexcited States in CdSe and CdSe/CdS Nanoplatelets. *Nano Lett.* **2014,** *14*, 7039-7045.
11. Ithurria, S.; Tessier, M. D.; Mahler, B.; Lobo, R. P. S. M.; Dubertret, B.; Efros, A. L., Colloidal Nanoplatelets With Two-Dimensional Electronic Structure. *Nat. Materials* **2011,** *10*, 936-941.
12. Bertrand, G. H. V.; Polovitsyn, A.; Christodoulou, S.; Khana, A. H.; Moreels, I., Shape control of zincblende CdSe nanoplatelets. *Chem. Commun.* **2016,** *52*, 11975-11978.
13. Scott, R.; Achtstein, A. W.; Prudnikau, A. V.; Antanovich, A.; Siebbeles, L. D. A.; Artemyev, M.; Woggon, U., Time-Resolved Stark Spectroscopy in CdSe Nanoplatelets: Exciton Binding Energy, Polarizability, and Field-Dependent Radiative Rates. *Nano Lett.* **2016,** *16*, 6576-6583.

14. Benchamekh, R.; Gippius, N. A.; Even, J.; Nestoklon, M. O.; Jancu, J. M.; Ithurria, S.; Dubertret, B.; Efros, A. L.; Voisin, P., Tight-Binding calculations of Image-Charge Effects in Colloidal Nanoscale Platelets of CdSe. *Phys. Rev. B* **2014,** *89*, 035307.
15. Achtstein, A. W.; Schliwa, A.; Prudnikau, A.; Hardzei, M.; Artemyev, M. V.; Thomsen, C.; Woggon, U., Electronic Structure and Exciton–Phonon Interaction in Two-Dimensional Colloidal CdSe Nanosheets. *Nano Lett.* **2012,** *12*, 3151-3157.
16. Rajadell, F.; Climente, J. I.; Planelles, J., Excitons in Core-Only, Core-Shell and Core-Crown CdSe Nanoplatelets: Interplay Between In-Plane Electron-Hole Correlation, Spatial Confinement, and Dielectric Confinement. *Phys. Rev. B* **2017,** *96*, 35307-35316.
17. Achtstein, A. W.; Scott, R.; Kickhöfel, S.; Jagsch, S. T.; Christodoulou, S.; Bertrand, G. H. V.; Prudnikau, A. V.; Antanovich, A.; Artemyev, M.; Moreels, I.; Schliwa, A.; Woggon, U., p-State Luminescence in CdSe Nanoplatelets: Role of Lateral Confinement and a Longitudinal Optical Phonon Bottleneck. *Phys. Rev. Lett.* **2016,** *116*, 116802.
18. Biadala, L.; Liu, F.; Tessier, M. D.; Yakovlev, D. R.; Dubertret, B.; Bayer, M., Recombination Dynamics of Band Edge Excitons in Quasi-Two-Dimensional CdSe Nanoplatelets. *Nano Lett.* **2014,** *14*, 1134-1139.
19. Morgan, D.; Kelley, D. F., Role of Surface States in Silver-Doped CdSe and CdSe/CdS Quantum Dots. *J. Phys. Chem. C* **2018,** *122*, 10627-10636.
20. Li, Q.; Lian, T., Area- and Thickness-Dependent Biexciton Auger Recombination in Colloidal CdSe Nanoplatelets: Breaking the "Universal Volume Scaling Law". *Nano Lett.* **2017,** *17*, 3152-3158.
21. Grim, J. Q.; Christodoulou, S.; Di Stasio, F.; Krahne, R.; Cingolani, R.; Manna, L.; Moreels, I., Continuous-wave biexciton lasing at room temperature using solution-processed quantum wells. *Nature Nanotechnology* **2014,** *9*, 891.
22. Leosson, K.; Jensen, J. R.; Langbein, W.; Hvam, J. M., Exciton localization and interface roughness in growth-interrupted GaAs/AlAs quantum wells. *Phys. Rev. B* **2000,** *61*, 10322-10329.

Ch 7

Mechanism of Hole Trap Passivation in CdSe QD by Alkylamines

Abstract

The mechanism by which alkylamines brighten CdSe nanoparticles is investigated by transient absorption and time-resolved photoluminescence spectroscopy. The main effect of the amine is to reduce the extent of surface hole trapping, which cannot be rationalized by a model in which the amine directly binds to and thereby passivates a surface trap site. An alternative mechanism is proposed wherein the absolute energies of the valence and conduction band edges shift to more negative redox potentials upon binding of the amine. This decreases the thermodynamic driving force for hole trapping or hole transfer to an adsorbed acceptor, 4-methylbenzenethiol. Amine binding also increases the thermodynamic driving force for electron transfer to an adsorbed acceptor, methyl viologen. The rates of charge transfer to these acceptors have been measured and the differences in the rates before and after treatment with alkylamines are consistent with the proposed mechanism.

7.1 Introduction

One of the most widely used approaches for controlling the properties of II-VI metal-chalcogenide semiconductor nanoparticles is to introduce organic ligands that bind to the surfaces of the particles. Primary alkylamines are ubiquitous in this procedure. They have been used as surface ligands for over two decades, and many studies have been done to determine the nature of the ligand-particle interactions. The alkylamine can be introduced either pre- or post-synthetically and can confer a range of desirable properties such as colloidal stability, enhanced photoluminescence, precursor activation and lower synthesis temperatures, and can be used as the reducing agent in the formation and growth reactions.[1] Because of their widespread use, it is important to understand how these effects come about.

The common model used to describe electronic surface passivation of nanoparticles involves direct binding of a ligand to surface sites that act as carrier traps. States close to the conduction band are associated with surface metal (typically cadmium) atoms.[2] These states are typically above the Fermi level and can act as electron traps. Conversely, mid-gap states close to the valence band edge are associated with under-coordinated surface chalcogenide atoms[2] and can act either as hole traps when filled or electron traps when empty.[3, 4] The extent to which these orbitals are filled is determined by the Fermi level, which depends on synthesis conditions, surface ligands, and particle stoichiometry. In order to passivate surface hole traps, a ligand must act as a Lewis acid, forming a bond involving the surface electrons. Cadmium carboxylates, for example, have been described as a Lewis acid-type ligand that can passivate surface selenium non-bonding orbitals, and removal of cadmium carboxylate therefore gives rise to hole trapping.[5] Lewis bases are similarly thought to be able to passivate electron traps. Several authors suggest that primary alkylamines bind to empty surface 5s orbitals associated with Cd^{2+} ions and raise photoluminescence (PL) quantum yields (QYs) by shutting off electron trapping.[6] Others

suggest a passivation mechanism wherein amines bind to surface cadmium atoms through the N lone pair, positioning the alpha-protons such that they can coordinate with neighboring selenium ions and remove the hole trap states from the gap.[7] Organophosphines are commonly thought to interact with surface selenium atoms having empty surface orbitals,[8] and these empty chalcogenide orbitals can also act as electron traps. In a recent publication we showed that the absence of tributylphosphine (TBP) from CdSe/CdS particles results in conduction band electron trapping as well as thermal population of mid-gap states by valence band electrons, giving rise to surface p-doping of the particle.[4] These results imply that TBP primarily interacts with empty surface chalcogenide orbitals rather than filled ones. Clearly, there are many overlapping and conflicting interpretations of how different ligands interact with different types of surface states, and no single model can be used to describe all of the observed results. It is likely that the densities and oxidation states of the surface atoms are highly sensitive to synthesis conditions, purification procedures, and post-synthetic modification procedures, so the observed ligand-particle interactions will vary based on the exact methods used.

A few important studies have provided some insights into how surface and adsorbed chalcogenides result in hole traps and how amines interact with the nanocrystal surfaces. Reference [9] shows that octylamine activates elemental sulfur to form polyalkylammonium sulfides which then decompose mainly into H_2S, thioamides, and amides. The H_2S generated by the reaction is a much more reactive precursor than elemental sulfur and therefore facilitates more rapid nanoparticle growth kinetics and lower reaction temperatures. Furthermore, although H_2S is a gas and should easily leave the reaction mixture upon venting, it has been shown that amines increase its solubility by conversion to the alkylammonium sulfide, thereby retaining the sulfur species in solution, where it can act as a hole trap.[10] Interestingly, the hole trapping efficiency of H_2S directly added to a solution containing CdSe/CdS quantum dot (QDs) was reduced from 100% to ~ 30% upon adding oleylamine. The authors suggest that this may occur by a mechanism wherein amines binding to the surface block the approach of H_2S or that they outcompete adsorbed H_2S, HS^-, and S^- for binding sites.[10]

The work presented here suggests an additional, completely different mechanism for understanding the changes in hole trapping and interfacial charge transfer dynamics that arise upon introducing an alkylamine to a solution of CdSe QDs. This mechanism is based on the consideration that carrier trapping or transfer rates depend critically on the thermodynamic driving force, i.e., the energy difference between the mid-gap trap or acceptor state and either the valence or conduction band edges. We suggest that the dynamical differences are due to changes in the conduction and valence band energetics that occur upon alkylamine binding. The suggestion of ligand-induced band shifts is well precedented. A number of experimental and computational studies report significant changes in the redox potentials of CdSe nanocrystals based on the surface stoichiometry and ligands present, with typical measured differences on the order of a few hundred meV.[6, 11-16] Analogous results are obtained for other types of nanocrystals.[12, 15, 17-19] Bloom et al. measure absolute valence band energies of CdSe QDs treated with aniline, thiophenol, and phenylphosphonic acid and report that the aniline-ligated particles are 270 meV closer to the vacuum level than the phosphonic acid-ligated particles.[11] Jasieniak et al. corroborate this result by measuring ionization energies of CdSe ligated with TOPO, alkylamines,

alkanethiols, and oleic acid, with the alkylamine-ligated particles ionizing at 5.4 eV compared with 5.6 eV for oleic acid and 5.65 eV for alkanethiols.[12] The authors note the correlation between ionization energies and hole trapping efficiencies, with ligands that increase the ionization energy showing a greater propensity for hole trapping. A later theoretical study on CdSe quantum dots predicts that the absolute energies of the conduction and valence bands shift to higher energies upon ligation by L-type electron donating ligands by more than an electron-volt.[6] This behavior is attributed to a surface dipole effect brought about by electron donation from the ligand to the particle. The electronic states associated with under-coordinated surface atoms are close in energy to the conduction or valence band edges,[2] and a change in the band edge positions of a few hundred meV is expected to greatly affect carrier trapping (or charge transfer) behavior.

Here we examine the effects of alkylamine ligation of CdSe QDs on hole trapping and electron and hole transfer rates. In contrast to reports of alkylamines passivating surface electron traps,[8, 20-23] the main effect of adding amine to the system studied here is the elimination of surface hole traps. This is inconsistent with the typical molecular orbital theory explanation of electronic passivation, wherein Lewis acids necessarily passivate hole traps while Lewis bases passivate electron traps. Although the possibility of direct coordination of a small fraction of the bound amines to surface Se^{2-} ions through the amine protons can also occur, the evidence presented here suggests a mechanism wherein the valence and conduction band edges are shifted to higher energies relative to the surface states, which either decreases the thermodynamic driving force for hole trapping or makes trapping altogether energetically unfavorable. We suggest that these effects can be understood in terms of alkylamine-ligation raising the energies of both the conduction and valence bands while not significantly changing the energies of charge acceptors on the surface, as shown in Scheme 1. This mechanism explains how a Lewis base (L-type ligand) can eliminate hole trapping states from the band gap without directly binding to the surface chalcogenide ions. The central idea of this mechanism is that since a surface trap or charge acceptor state is not completely within the surface dipole layer associated with the ligand shell, its energy is less affected by ligand dipole effects. It follows that electron (hole) transfer rates to externally adsorbed acceptors should increase (decrease) upon ligation by an amine, which is also illustrated in Scheme 1. The data presented below show that this is the case, which strongly supports the assertion that the energetic shift of the valence band is the dominant mechanism by which alkylamines passivate II-VI quantum dot surfaces with respect to hole trapping.

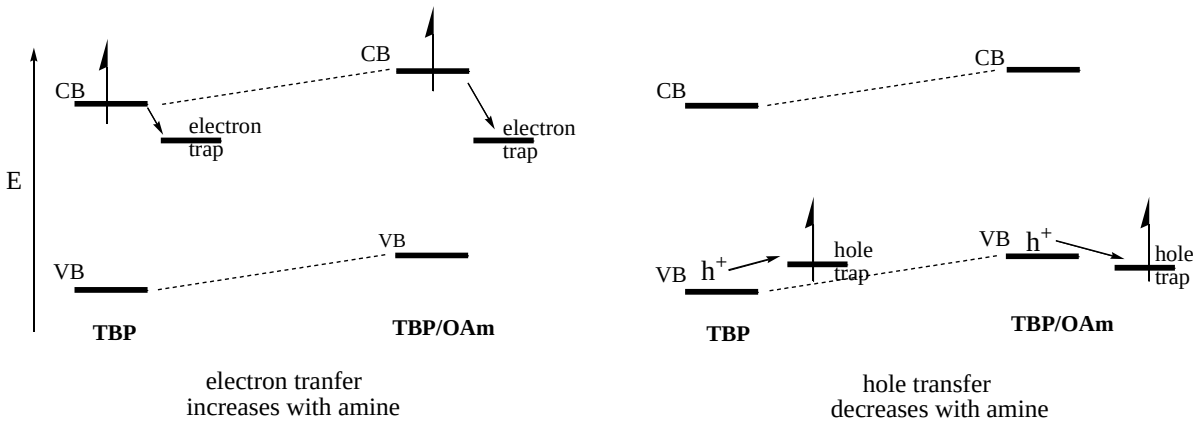

Figure 7.1. Changes in the thermodynamic driving force for electron (left) and hole transfer (right) to adsorbed acceptors upon ligation with amines. The effect on hole trapping is the same for hole transfer to an adsorbed acceptor.

7.2 Results and Discussion

7.2.1 QDs ligated with TBP vs TBP/OAm.

Analysis of kinetic data for single-material nanoparticles is often complicated by low quantum yields and the possibility of multiple nonradiative processes. The approach taken here is to eliminate most of these effects by starting out with well-passivated, high QY particles treated with both tributylphosphine (TBP) and oleylamine (OAm) then compare with the same particles ligated with only TBP. UV-vis and photoluminescence (PL) spectra for these particles are shown in Figure 7.1. The QDs have diameters of 2.9 nm, based on well-established sizing curves.[26] We note that the CdSe heavy hole effective mass is quite large,[28, 29] so the valence band energetics are only weakly size dependent. Thus, we expect that the hole trapping and hole transfer results presented below will be only weakly size dependent. Addition of the amine blue shifts the static absorption and PL spectra by ~ 5 nm, raises the PL QY from 6% to 37%, and eliminates the further red trap emission centered around 700 nm. The blue shift is commonly seen and has been attributed to etching surface Cd atoms from the particle, and under particle growth[30, 31] or lower temperature, harsh conditions, this certainly does occur.[32] However, we note that the conduction and valence bands are composed primarily from cadmium 5s and selenium 4p orbitals, respectively,[2] and to the extent to which the amine lone pair forms a bond with the cadmium 5s orbital, covalent interactions associated with adsorption of an electron donor can affect the conduction and valence bands slightly differently and may contribute to the observed blue shift.[11] Consistent with the shift being an electronic effect, one study observes that addition of allylamine results in a 5 - 6 nm blue shift that partially reverses upon pumping the amine off, which argues for the blue shift resulting primarily from an electronic effect.[33] Similar effects have been seen in small CdS clusters.[34] Under the mild

(60 °C) conditions used here for ligand exchange, it is likely that much of the blue shift seen in figure 7.2A can be assigned to electronic effects. The carrier trapping process responsible for the low quantum yields without amine can be assigned by comparison of the transient absorption (TA) and PL kinetics shown in Figure 7.2.

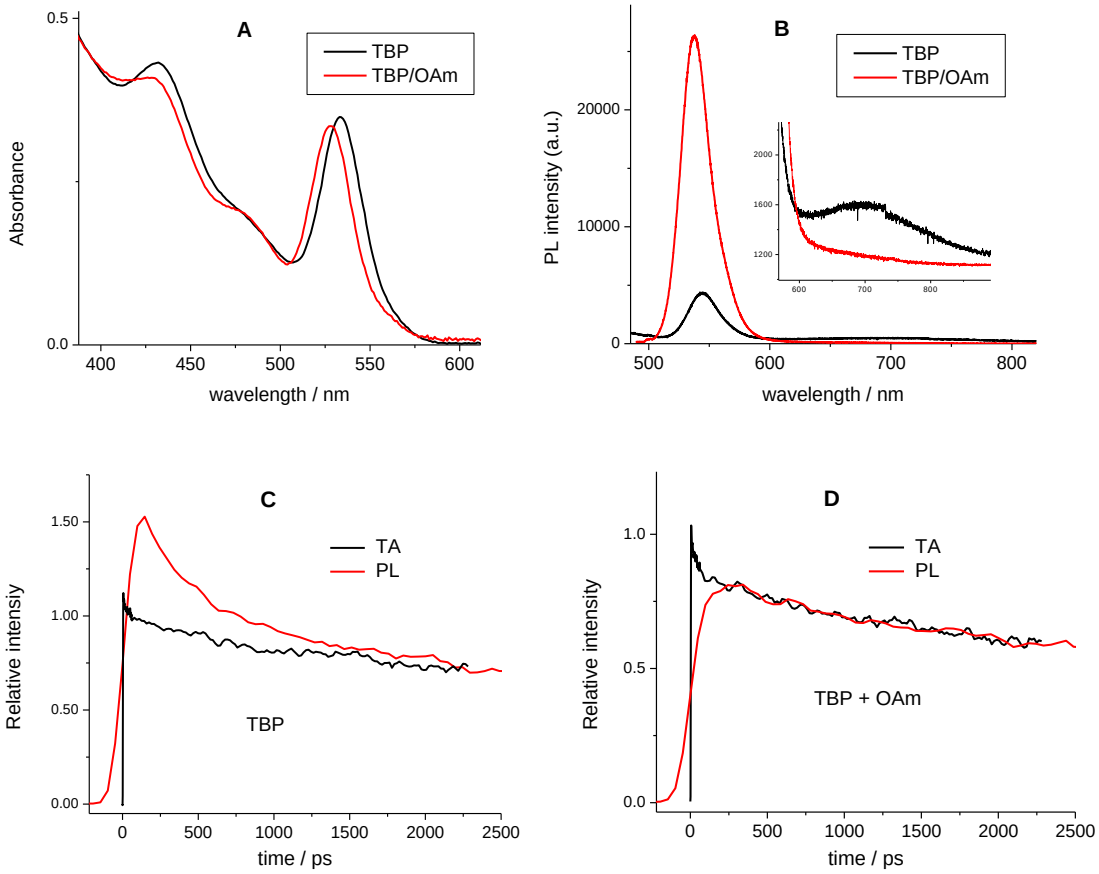

Figure 7.2. Absorption (A) and photoluminescence (B) spectra of 2.9 nm CdSe QDs ligated with either TBP or TBP and OAm. The inset in (B) zooms in on the region between 600 - 900 nm. Panels (C) and (D) compare TA and PL kinetics measured at the bleach and PL maxima for the same particles ligated with either TBP or TBP and OAm, respectively.

We take advantage of the fact that the TA and PL measurements probe different aspects of the excited state, with the PL measuring the loss of excitonic population (loss of the electron, hole, or both) while the TA bleach kinetics are sensitive only to the presence of the conduction band electron, i.e., conduction band state filling.[35] This comes about because the exciton to biexciton transition occurs at close to the same energy and has close to the same oscillator strength as the negative particle to negative trion transition.[36, 37] Since hole trapping transfers population from the excitonic state to negatively charged particles, there is no signature of this process in the excited state absorption spectrum. The kinetics in Figure 7.1 (C) and (D) show that without the alkylamine, there is a ~ 500 ps component

present in the PL decay that is absent in the TA kinetics, indicating that valence band depopulation (i.e., hole trapping) is occurring on this timescale. Addition of OAm eliminates this component, definitively assigning the dominant nonradiative process to hole trapping and establishing that the amine shuts off this process. The convolved fits to the PL decays using the temporal instrument response function of the TCSPC apparatus are shown in Figure 7.3.

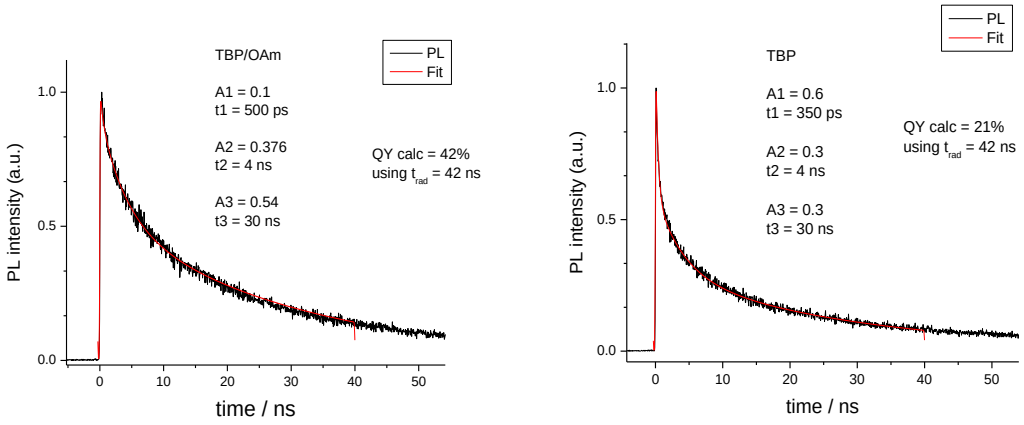

Figure 7.3 PL decays and triexponential fits to 2.9 nm diameter CdSe QD ligated with TBP/OAm (left) and TBP (right).

Calculating the PLQY using the fitting parameters and a radiative lifetime of 42 ns[38] gives values of 42% and 21% for the TBP/OAm- and TBP-ligated particles, whereas the measured QY are 37% and 6%, respectively. For the well-passivated particles, the difference between the measured QY and that calculated from the PL decay can be attributed to the fast electron trapping component seen in the TA kinetics (figure 1D), which makes up ~ 15% of the total decay. We conclude that in this case, all of the electron and hole trapping processes are observed with the combination of the PL and TA measurements. Without the amine, the measured QY is a factor of 3.5 lower than that calculated from the PL decay curve, indicating that ~ 70% of the population traps on a timescale faster than can be resolved. Since there is no corresponding fast component seen in the TA kinetics, the process is assigned to hole trapping. We conclude that addition of the amine eliminates both the sub-100 ps hole trapping as well as the ~ 500 ps hole trapping component. The same qualitative result is seen when using octylamine or triethylamine, confirming that the phenomenon is general and not just restricted to oleylamine. The triethylamine results are pertinent assigning the binding passivation mechanism and will be discussed further below.

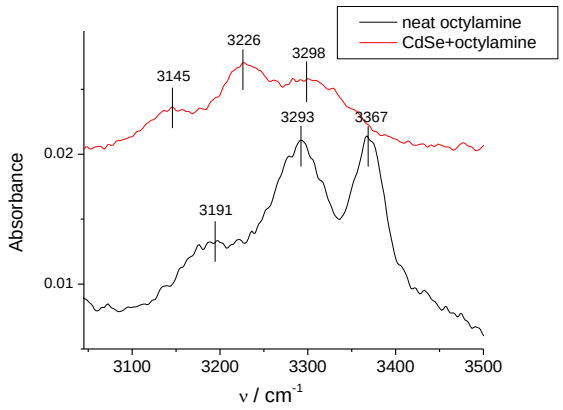

Figure 7.4. FTIR spectra of neat octylamine and 2.9 nm diameter CdSe ligated with octylamine. The latter spectrum is translated upwards for clarity.

It is commonly accepted that amines bind to CdSe through coordination of the nitrogen lone pair with surface cadmium ions, and this is directly confirmed by a recent NMR study.[39] The FTIR spectra of the N-H stretching region of octylamine-ligated CdSe are reported in reference [40] and the comparison with neat octylamine is shown below in Figure 7.4. Consistent with what is calculated for CdSe-methylamine complexes, the N-H stretching modes broaden and shift ~ 60 cm^{-1} toward lower frequencies upon binding.[41] One can consider the possibility that the amine either binds to selenium ions via a positive moiety like the amine protons or by participating in acid/base chemistry that changes the protonation state of the surface species. Either process would significantly change the structure of the N-H stretching region, but the spectra shown in Figure 7.4 show that the number of modes, their relative intensities and splittings remain largely unchanged upon binding, indicating that this chemistry doesn't occur in a significant fraction of the ligands. Furthermore, the reduction of hole trapping upon treatment with triethylamine, as shown below in Figure 7.5 confirms confirming that binding via an amine proton is not the likely source of surface passivation.

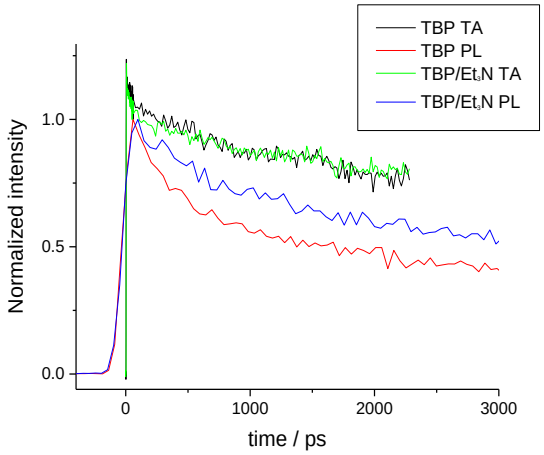

Figure 7.5. TA and PL decays with and without treatment with excess triethylamine normalized at t = 0..

7.2.2 QDs with an adsorbed hole acceptor

The static and dynamic spectra of the same CdSe QDs described above were measured before and after addition of the hole acceptor, 4-methylbenzenethiol (MBT).[42] Figure 7.6A shows that the addition of MBT to QD ligated with both TBP and OAm results in only a small drop in the QY. In contrast, figure 7.6B shows that in the absence of an alkylamine, MBT addition causes the QY to drop by about 50%. Despite this drop, the TA kinetics are unchanged and only a small amplitude fast component making up 11% of the total decay is introduced in the PL kinetics. As in the above analysis, this is the signature of hole trapping that occurs faster than can be resolved by the 55 ps instrument response function of the PL measurement. With OAm present, the thiol drops the QY from 42 to 39%, and the PL decays are unchanged within the signal to noise, representing a dramatic reduction in the hole transfer efficiency to the thiol. We note that this behavior could also be explained if the amine were to outcompete the thiol for binding sites. The lack of a strong MBT concentration dependence in the PL quenching, however, suggests that this is not the case.

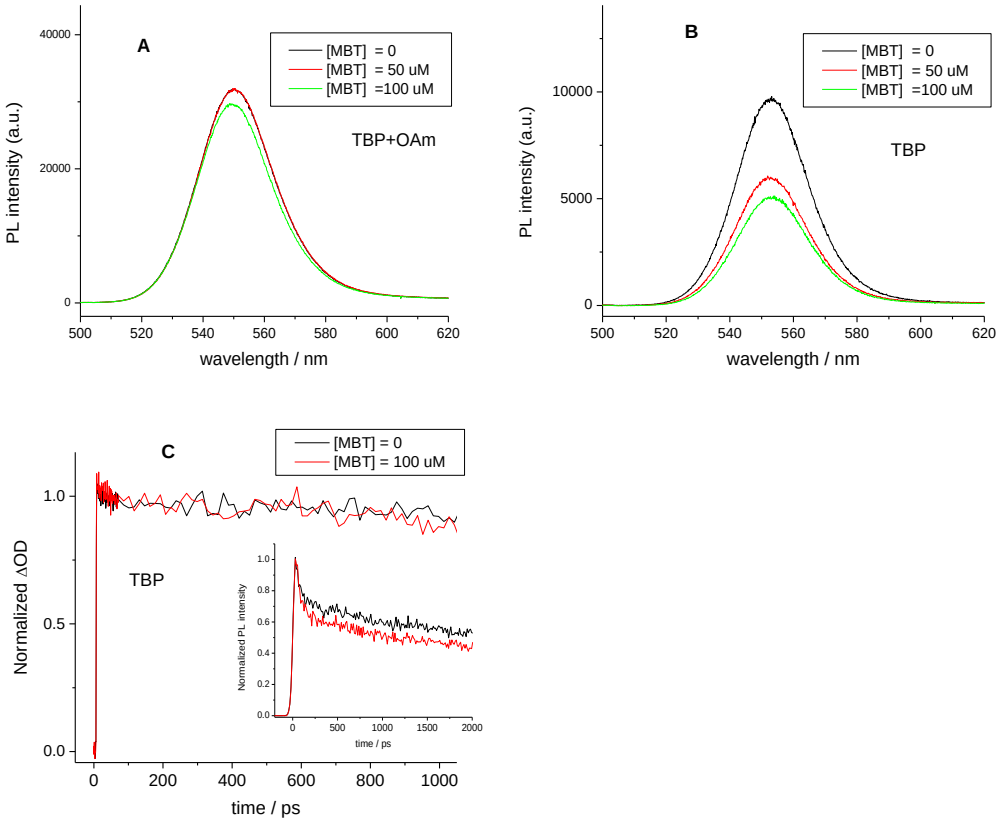

Figure 7.6 2.9 nm diameter CdSe before and after addition of 4-methylbenzenethiol. (A) Static PL spectrum with TBP/OAm. (B) Static PL spectrum with TBP. (C) TA (and PL, inset) decay with TBP.

7.2.3 QDs with an adsorbed electron acceptor, methylviologen.

Electron transfer to methyl viologen (MV) takes place on a timescale that is easily measured in a TA experiment. In these studies, a small amount of MV is added to the same QDs as above ligated with either TBP or TBP and OAm. The concentration of MV is chosen such that about one-third of the particles have an attached acceptor. Since MV is a 2+ ion, it is expected to near-quantitatively bind to the particles when added to a hexane solution. The decays of the QDs with MV are scaled to match those without MV at long times, so the difference between the decay curves gives the electron transfer kinetics. These results are shown in Figure 7.7 along with the difference kinetics shown in the insets.

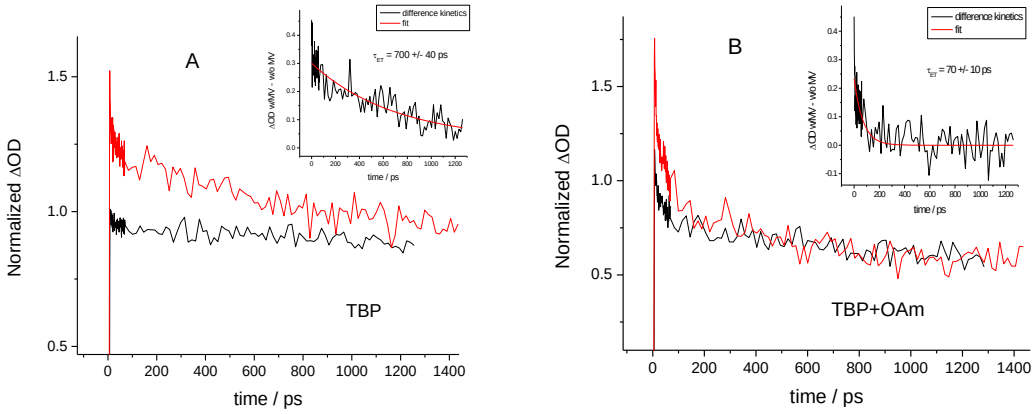

Figure 7.7. TA kinetics of 2.9 nm diameter CdSe QDs having TBP ligands (A) and TBP and OAm ligands (B) before and after addition of the electron acceptor methylviologen. The insets show scaled difference kinetics: QDs without MV subtracted from QDs with MV. Black: [MV] = 0, red: [MV] = 6 * 10^{-7} M.

The difference kinetics show that the electron transfer time decreases from 700 to 70 ps upon addition of OAm. We note that the possibility that the charge transfer kinetics are affected by the unavailability of binding sites occupied by the amine does not apply here. Competitive binding would affect only the magnitude of the fast transient and not the rates in the difference kinetics. These results show that the addition of alkylamines increases the QD to MV electron transfer rate. This increase is consistent with the energetic shifts in Scheme 1 and Marcus theory, which predicts that when the driving force for a nonadiabatic charge transfer reaction is small compared to the reorganization energy, the reaction rate increases with energetic driving force.[43] The Marcus inverted regime is rarely observed in QD charge transfer reactions, so these considerations also apply to electron transfer reactions when the energetic driving forces is relatively large. This is because excess electron energy can be conserved during charge transfer through an Auger-assisted mechanism, where excitation of the hole into the manifold of densely spaced hole states serves as the receiving mode.[44] Although we conclude that these charge transfer rates are significantly enhanced as predicted by the model shown in Figure 7.1, due to uncertainties in the absolute energetics, a quantitative analysis of the changes in these rates is not feasible. We do note, however, that reference [44] calculates that when the electron transfer driving force is comparable to the reorganization energy, a 0.2 eV increase in driving results in an increase in the electron transfer rates of just under an order of magnitude, which is in good agreement with our results and the model proposed here.

Conclusions

The PLQYs of the CdSe QDs studied here increase upon post-synthetic treatment with alkylamines, and the effect is assigned to the removal of surface hole trapping states from the band gap. The surface dipole effect associated with binding of the L-type electron donating ligand shifts the conduction and valence band edges upward by > 200 meV, decreasing the thermodynamic driving force for surface hole trapping. Treatment with alkylamines greatly decreases the rate of hole transfer to externally adsorbed hole traps while increasing the rate of electron transfer to external electron traps. Both trends are consistent with simple Marcus theory considerations. The model proposed here provides an altogether new approach to understanding electronic passivation of surface states on semiconductor nanoparticles and should inform future endeavors to achieve high quantum yield optical materials. Aside from the greater understanding of PL quenching and brightening mechanisms this provides, the effect also holds promise for engineering QD band offsets for photocatalysis, solar energy and display applications.

Acknowledgement

This material is based upon work supported by the U.S. Department of Energy, Office of Science, Office of Basic Energy Sciences, under award number DE-SC0018307.

Ch 7 References

1. Mourdikoudis, S.; Liz-Marzán, L. M., Oleylamine in Nanoparticle Synthesis. *Chem. Materials* **2013,** *25*, 1465-1476.
2. Norris, D. J., Electronic Structure in Semiconductor Nanocrystals: Optical Experiment. In *Nanocrystal Quantum Dots*, 2'd ed.; Klimov, V. I., Ed. CRC Press: 2010.
3. Morgan, D.; Kelley, D. F., Role of Surface States in Silver-Doped CdSe and CdSe/CdS Quantum Dots. *J. Phys. Chem. C* **2018,** *122*, 10627-10636.
4. Morgan, D.; Kelley, D. F., Spectroscopy of Surface-State p-Doped CdSe/CdS Quantum Dots. *J. Phys. Chem. Lett.* **2018,** *9*, 4160-4165.
5. Anderson, N. C.; Hendricks, M. P.; Choi, J. J.; Owen, J. S., Ligand Exchange and the Stoichiometry of Metal Chalcogenide Nanocrystals: Spectroscopic Observation of Facile Metal-Carboxylate Displacement and Binding. *J. Am. Chem. Soc.* **2013,** *135*, 18536−18548.
6. Houtepen, A. J.; Hens, Z.; Owen, J. S.; Infante, I., On the Origin of Surface Traps in Colloidal II–VI Semiconductor Nanocrystals. *Chem. Materials* **2017,** *29*, 752-761.
7. Kippeny, T. C.; II, M. J. B.; III, A. D. D.; McBride, J. R.; Orndorff, R. L.; Garrett, M. D.; Rosenthal, S. J., Effects of Surface Passivation on the Exciton Dynamics of CdSe Nanocrystals as Observed by Ultrafast Fluorescence Upconversion Spectroscopy. *J. Chem. Phys.* **2008,** *128*, 84713-84720.
8. Kim, W.; Lim, S. J.; Jung, S.; Shin, S. K., Binary Amine-Phosphine Passivation of Surface Traps on CdSe Nanocrystals. *J. Phys. Chem. C* **2010,** *114*, 1539-1546.
9. Thomson, J. W.; Nagashima, K.; Macdonald, P. M.; Ozin, G. A., From Sulfur−Amine Solutions to Metal Sulfide Nanocrystals: Peering into the Oleylamine−Sulfur Black Box. *J. Am. Chem. Soc.* **2011,** *133*, 5036-5041.
10. Pu, C.; Peng, X., To Battle Surface Traps on CdSe/CdS Core/Shell Nanocrystals: Shell Isolation versus Surface Treatment. *J. Am. Chem. Soc.* **2016,** *138*, 8134-8142.
11. Bloom, B. P.; Zhao, L.-B.; Wang, Y.; Waldeck, D. H.; Liu, R.; Zhang, P.; Beratan, D. N., Ligand-Induced Changes in the Characteristic Size-Dependent Electronic Energies of CdSe Nanocrystals. *J. Phys. Chem. C* **2013,** *117*, 22401-22411.
12. Jasieniak, J.; Califano, M.; Watkins, S. E., Size-Dependent Valence and Conduction Band-Edge Energies of Semiconductor Nanocrystals. *ACS Nano* **2011,** *5*, 5888–5902.
13. Munro, A. M.; Zacher, B.; Graham, A.; Armstrong, N. R., Photoemission Spectroscopy of Tethered CdSe Nanocrystals: Shifts in Ionization Potential and Local Vacuum Level As a Function of Nanocrystal Capping Ligand. *ACS App. Mat. & Int.* **2010,** *2*, 863-869.
14. Wang, C.; Shim, M.; Guyot-Sionnest, P., Electrochromic Nanocrystal Quantum Dots. *Science* **2001,** *291*, 2390-2393.
15. Soreni-Harari, M.; Yaacobi-Gross, N.; Steiner, D.; Aharoni, A.; Banin, U.; Millo, O.; Tessler, N., Tuning Energetic Levels in Nanocrystal Quantum Dots through Surface Manipulations. *Nano Lett.* **2008,** *8*, 678-684.
16. Carroll, G. M.; Tsui, E. Y.; Brozek, C. K.; Gamelin, D. R., Spectroelectrochemical Measurement of Surface Electrostatic Contributions to Colloidal CdSe Nanocrystal Redox Potentials. *Chem. Mater.* **2016,** *28*, 7912-7918.

17. Kroupa, D. M.; Vörös, M.; Brawand, N. P.; McNichols, B. W.; Miller, E. M.; Gu, J.; Nozik, A. J.; Sellinger, A.; Galli, G.; Beard, M. C., Tuning Colloidal Quantum Dot Band Edge Positions Through Solution-Phase Surface Chemistry Modification. *Nature Com.* **2017,** *8*, 15257.
18. Santra, P. K.; Palmstrom, A. F.; Tanskanen, J. T.; Yang, N.; Bent, S. F., Improving Performance in Colloidal Quantum Dot Solar Cells by Tuning Band Alignment through Surface Dipole Moments. *J. Phys. Chem. C* **2015,** *119*, 2996-3005.
19. Nguyen, E. P.; Carey, B. J.; Ou, J. Z.; van Embden, J.; Gaspera, E. D.; Chrimes, A. F.; Spencer, M. J. S.; Zhuiykov, S.; Kalantar-zadeh, K.; Daeneke, T., Electronic Tuning of 2D MoS2 Through Surface Functionalization. *Adv. Mat.* **2015,** *27*, 6225-6229.
20. Ji, X.; Copenhaver, D.; Sichmeller, C.; Peng, X., Ligand Bonding and Dynamics on Colloidal Nanocrystals at Room Temperature: The Case of Alkylamines on CdSe Nanocrystals. *J. Am. Chem. Soc.* **2008,** *130*, 5726-5735.
21. Bullen, C.; Mulvaney, P., The Effects of Chemisorption on the Luminescence of CdSe Quantum Dots. *Langmuir* **2006,** *22*, 3007.
22. Krause, M. M.; Kambhampati, P., Linking Surface Chemistry to Optical Properties of Semiconductor Nanocrystals. *Phys. Chem. Chem. Phys.* **2015,** *17*, 18882-18894.
23. Zhou, J.; Zhu, M.; Meng, R.; Qin, H.; Peng, X., Ideal CdSe/CdS Core/Shell Nanocrystals Enabled by Entropic Ligands and Their Core Size-, Shell Thickness-, and Ligand-Dependent Photoluminescence Properties. *J. Am. Chem. Soc.* **2017,** *139*, 16556-16567.
24. Pu, C.; Zhou, J.; Lai, R.; Niu, Y.; Nan, W.; Peng, X., Highly Reactive, Flexible Yet Green Se Precursor for Metal Selenide Nanocrystals: Se-Octadecene Suspension (Se-SUS). *Nano Res.* **2013,** *6*, 652-670.
25. Yang, Y.; Li, J.; Lin, L.; Peng, X., An Efficient and Surface-Benign Purification Scheme for Colloidal Nanocrystals Based on Quantitative Assessment. *Nano Research* **2015,** *8*, 3353-3364.
26. Jasieniak, J.; Smith, L.; van Embden, J.; Mulvaney, P.; Califano, M., Re-examination of the Size-Dependent Absorption Properties of CdSe Quantum Dots. *J. Phys. Chem. C* **2009,** *113*, 19468 - 19474.
27. Gong, K.; Kelley, D. F., Surface Charging and Trion Dynamics in CdSe-Based Core/Shell Quantum Dots. *J. Phys. Chem. C* **2015,** *119*, 9637-9645.
28. Lin, C.; Kelley, D. F.; Rico, M.; Kelley, A. M., The "Surface Optical" Phonon in CdSe Nanocrystals. *ACS Nano* **2014,** *9*, 3928-3938.
29. Ithurria, S.; Tessier, M. D.; Mahler, B.; Lobo, R. P. S. M.; Dubertret, B.; Efros, A. L., Colloidal Nanoplatelets With Two-Dimensional Electronic Structure. *Nat. Materials* **2011,** *10*, 936-941.
30. Tan, R.; Shen, Y.; Roberts, S. K.; Gee, M. Y.; Blom, D. A.; Greytak, A. B., Reducing Competition by Coordinating Solvent Promotes Morphological Control in Alternating Layer Growth of CdSe/CdS Core/Shell Quantum Dots. *Chem. Materials* **2015,** *27*, 7468-7480.
31. Guo, Y.; Marchuk, K.; Sampat, S.; Abraham, R.; Fang, N.; Malko, A. V.; Vela, J., Unique Challenges Accompany Thick-Shell CdSe/nCdS (n > 10) Nanocrystal Synthesis. *J. Phys. Chem. C* **2012,** *116*, 2791-2800.

32. Li, R.; Lee, J.; Yang, B.; Horspool, D. N.; Aindow, M.; Papadimitrakopoulos, F., Amine-Assisted Facetted Etching of CdSe Nanocrystals. *J. Am. Chem. Soc.* **2005,** *127*, 2524-2532.
33. Talapin, D. V.; Rogach, A. L.; Kornowski, A.; Haase, M.; Weller, H., Highly Luminescent Monodisperse CdSe and CdSe/ZnS Nanocrystals Synthesized in a Hexadecylanine-Trioctylphosphine Oxide-Trioctylphosphine Mixture. *Nano Lett.* **2001,** *1*, 207.
34. Nevers, D. R.; Williamson, C. B.; Hanrath, T.; Robinson, R. D., Surface Chemistry of Cadmium Sulfide Magic-Sized Clusters: A Window into Ligand-Nanoparticle Interactions. *Chem. Com.* **2017,** *53*, 2866-2869.
35. Klimov, V. I., Spectral and Dynamical Properties of Multiexcitons in Semiconductor Nanocrystals. *Annu. Rev. Phys. Chem.* **2007,** *58*, 635-73.
36. Shabaev, A.; Rodina, A. V.; Efros, A. L., Fine Structure of the Band-Edge Excitons and Trions in CdSe/CdS Core/Shell Nanocrystals. *Phys. Rev. B* **2012,** *86*, 205311-205325.
37. Rodina, A. V.; Efros, A. L., Band-edge Biexciton in Nanocrystals of Semiconductors with a Degenerate Valence Band. *Phys. Rev. B* **2010,** *82*, 125324-125337.
38. Gong, K.; Zeng, Y.; Kelley, D. F., Extinction Coefficients, Oscillator Strengths, and Radiative Lifetimes of CdSe, CdTe, and CdTe/CdSe Nanocrystals. *J. Phys. Chem. C* **2013,** *117*, 20268-20279.
39. Kurihara, T.; Noda, Y.; Takegoshi, K., Quantitative Solid-State NMR Study on Ligand–Surface Interaction in Cysteine-Capped CdSe Magic-Sized Clusters. *J. Phys. Chem. Lett.* **2017,** *8*, 2555-2559.
40. Zhou, Y.; Wang, F.; Buhro, W. E., Large Exciton Energy Shifts by Reversible Surface Exchange in 2D II–VI Nanocrystals. *J. Am. Chem. Soc.* **2015,** *137*, 15198-15208.
41. Yarwwod, J., *Spectroscopy and Structure of Molecular Complexes*. Plenum: London, 1973.
42. Grenland, J. J.; Maddux, C. J. A.; Kelley, D. F.; Kelley, A. M., Charge Trapping versus Exciton Delocalization in CdSe Quantum Dots. *J. Phys. Chem. Lett.* **2017,** *8*, 5113-5118.
43. Marcus, R. A., Chemical and Electrochemical Electron-Transfer Theory. *Ann. Rev. Phys. Chem.* **1964,** *15*, 155–196.
44. Zhu, H.; Yang, Y.; Hyeon-Deuk, K.; Califano, M.; Song, N.; Wang, Y.; Zhang, W.; Prezhdo, O. V.; Lian, T., Auger-Assisted Electron Transfer from Photoexcited Semiconductor Quantum Dots. *Nano Lett.* **2014,** *14*, 1263-1269.

Ch 8

Exciton Localization and Radiative Lifetimes in CdSe Nanoplatelets

Abstract

The spatial extents of CdSe nanoplatelet (NPL) excitons are investigated using transient absorption (TA) spectroscopy. The relative bleach magnitudes of a series of NPLs with varying lateral dimensions are compared with a quantum dot (QD) standard, allowing the relative magnitude of the heavy hole (HH) bleach to be determined as a function of size. The bleach of the HH absorbance decreases with increasing NPL area, while the excitonic sizes calculated from the bleach magnitudes are found to be independent of the lateral dimensions. This result is consistent with a model that considers the relative intensities of photoinduced absorption (PA) and stimulated emission (SE) contributed by distinct regions of the platelet occupied by either the electron, the electron and hole, or neither. Using this model gives an estimated average excitonic area of 21.2 ± 2.5 nm^2. Considering the small spatial extent of the relaxed NPL exciton compared with the number of oscillators participating in ground state absorption partially accounts for the discrepancy between the HH extinction coefficients and the slow radiative rates, which deviate from the values calculated from the Einstein relations by a factor between ~ 30 – 80. The electron-hole overlap integral is estimated from the ratio of HH bleach magnitudes before and after trapping the hole by 4-methylbenzenethiol (MBT), a hole acceptor, and is then factored into calculations of the radiative lifetimes. Together with the measured singlet-triplet splitting and e-h overlap, these considerations allow the NPL radiative kinetics to be semiquantitatively reproduced.

8.1 Introduction

II-VI semiconductor nanoparticles are desirable optical materials because of their large absorption cross-sections, narrow emission linewidths, color tunability, and high photoluminescence quantum yields (PLQYs). Controlling these properties requires developing an understanding of the photophysics and quantum mechanics governing the materials' behavior. Of particular importance is the fundamental description of the excitonic state. Excitonic wavefunctions in semiconductors are typically expressed in terms of Bloch functions, which consist of a unit cell-localized function multiplied by the envelope function, a term that describes the extent to which the wavefunction is delocalized over the lattice.[1] Many of the unique and useful optical properties of nanomaterials come about due to quantum confinement, which occurs when the physical dimensions of the nanostructures are smaller than the exciton Bohr radius. Quantum confinement results in large electron and hole zero-point energies, effectively increasing the band gap as well as increasing the electron-hole Coulombic and exchange interactions.

In II-VI semiconductors, the valence and conduction bands are composed of mostly chalcogenide p and metal s orbitals, respectively.[2] Thus, the electron has only spin

angular momentum while the hole has both spin and orbital angular momenta. The resulting excitonic states are split by spin-orbit coupling, particle shape and crystal field anisotropies and the electron-hole exchange interaction. For spherical zincblende (cubic) CdSe quantum dots (QD), the x-, y-, and z-polarized transitions to the excitonic states are indistinguishable. In terms of the angular momentum fine structure, this manifests as the J = 3/2 (heavy hole, HH) and J = 1/2 (light hole, LH) hole states being nearly degenerate. The electron-hole exchange interaction leads to a relatively large (~25 meV in 3 nm diameter particles) splitting between the two lowest HH excitonic states, the optically forbidden J = ± 2 and the higher-lying optically allowed J = ± 1 states.[3] Several other allowed and dark states are at slightly higher energies and overlap the lowest energy state, increasing the valence band degeneracy and making the spectroscopy of the group of states quite complicated.

CdSe nanoplatelets (NPLs) are atomically flat two-dimensional sheets, having lateral dimensions of typically 5 – 40 nm. The NPL thicknesses are controllable, with 4.5 and 5.5 CdSe monolayers being the most extensively studied. The large lateral nanoplatelet sizes and strong out-of-plane confinement have significant effects on the electronic structure and spectroscopy. The cubic symmetry characteristic of the zincblende lattice is broken by the strong confinement along z, which pushes z-polarized transitions toward higher energy. A natural consequence is that the band-edge exciton is entirely plane-polarized.[5, 6] In terms of the fine structure levels, the anisotropy manifests in the large HH/LH splitting (~170 meV) exceeding the small inhomogeneous linewidths (~ 40 meV) characteristic of NPL samples.[4] Lifting the HH/LH degeneracy simplifies the NPL spectroscopy compared with spherical QDs, as the NPL band-edge exciton ($1S_{HH}$,$1S_e$) has only two states: a lower energy optically forbidden state and an optically allowed state about 5 meV higher in energy.[7, 8] The small exchange splitting is much less than the value of 20-25 meV measured for mid-sized QDs[3] and is due to the increased lateral size of the electron and hole wavefunctions. Due to their large lateral dimensions, NPLs have large extinction coefficients, typically greater than 10^7 L mol^{-1} cm^{-1}, that scale linearly with NPL area.[9]

The above considerations have significant implications in the observed NPL photophysics. Fundamental to understanding these photophysics is a quantitative understanding of the radiative lifetimes. Low temperature studies indicate that the lowest energy dark and bright states have radiative lifetimes of 12.5 ns and 180 ps,[7] and calculations of the radiative lifetime that ignore angular momentum states also predict very short lifetimes.[10] The value for a simple oscillator can be calculated from the absorption spectrum, using the Einstein relations. In this case, the radiative rate is given by[11, 12]

$$\frac{1}{\tau_{rad}} = \frac{8\pi\ 0.2303 n_f^3 \nu^3}{N_a c^2 n_a} \int \frac{\varepsilon(\nu)}{\nu} d\nu \cong 2.88x10^{-9} n^2 \tilde{\nu}^2 \int \varepsilon(\tilde{\nu})\, d\tilde{\nu} \qquad \text{E8.1}$$

For example, mid-sized (29 x 7.7 nm) 4.5 monolayer NPLs have a HH exciton maximum at 509.5 nm. The extinction coefficient at the HH maximum is 1.75 x 10^7 L mol^{-1} cm^{-1}, and the HH spectral linewidth is about 8 nm. Putting these values into equation 8.1 gives a radiative lifetime of 53 ps. At room temperature with a 5 meV dark/bright splitting,

about 45% are in the dipole allowed state, making the calculated radiative lifetime 110 ps. The above "giant oscillator strength" considerations suggest that the radiative lifetimes should be on the order of, or less than a few hundred picoseconds, which is consistent with measured low temperature radiative lifetimes.[4, 13, 14] However, the "coherence volume" of excitons in two-dimensional quantum wells decreases as the temperature increases. Thus, at higher temperatures the giant oscillator strength of the lowest transitions is lost and the radiative lifetime increases.[15] This is also seen to be the case in CdSe NPLs where room temperature photoluminescence (PL) decay measurements give radiative lifetimes between 4 and 6 ns.[4, 7, 16] This is much slower than can be accounted for based on the extinction coefficients and relative bright state populations, indicating exciton localization. If the exciton is localized over a much smaller region of the NPL, then the appropriate extinction coefficient to be used in equation 8.1 is that of the smaller region of the NPL.

The NPL spectroscopy may have complications due to the thermal accessibility of higher-lying excitonic states, specifically, an excitonic state observed ~ 25 meV higher than the HH maximum. The 25 meV splitting is found by fitting the band edge region of the absorbance spectra to a sum of Gaussians,[13] while (presumably) the same band is seen in time-resolved PL decays at 25 meV above the lowest energy HH emission and only at early times, < 40 ps. This feature has been assigned both to excimer emission[17] and to p-state emission.[18] Although the apparent lack of concentration dependence casts doubt on the mechanism involving excimer formation, the p state would be expected to have a non-negligible Boltzmann population at long times and therefore should give relatively weak emission for much longer than 40 ps. Such emission is not observed and we conclude that the assignment of this feature is still somewhat uncertain. Due to its relatively small population, any effect that it could have on the bleach magnitude is expected to be small and will be ignored in the analysis of the transient absorption spectra presented here.

Another consideration that enters into calculation of the radiative lifetime is the electron-hole overlap. In any Wannier-Mott exciton, the electron moves in the electric field of the hole and vice-versa.[1] If the electron and hole have different effective masses, then their spatial extents will be different. In the case of the II-VI semiconductors, the electron effective masses are much less than hole effective masses,[4] and holes will therefore be more localized than electrons. The result is that the electron-hole overlap integral (S) will be less than unity, and the radiative rate will be decreased by a factor of S^2. We note that this is different from the case of small QDs, where the overlap integral is always close to unity due to both the electron and hole wavefunctions being strongly confined along every dimension of the particle. Values of S can be obtained from transient absorption (TA) measurements on NPLs with and without adsorbed hole acceptors, as described below. This method of determining the overlap integral is based on the previous observation that the TA bleach has contributions from both valence and conduction band state filling.[16, 19] With this consideration, comparison of the bleach magnitudes of 4.5 monolayer CdSe NPLs with and without adsorbed methylbenzenethiol (MBT, a hole acceptor) allows values of the overlap integral to be determined.

The study presented here analyzes HH bleach magnitudes to obtain absolute excited state absorption cross sections for a series of 4.5 ML CdSe NPL as a function of the

lateral dimensions. Absolute magnitudes of the excited state absorption cross-sections following absorption of a single photon are very difficult to measure. We solve this problem by comparing the NPL bleach magnitude with that of a well-understood standard, specifically a sample of spherical CdSe QDs, and conclude that the fraction of the total absorbance that is bleached by absorption of a single photon is related to the fraction of the total NPL area that the exciton occupies. NPL radiative lifetimes are also measured and compared to the values calculated from the integrated extinction coefficients of the lowest excitonic state using a simple model that considers electron and hole localization, the Boltzmann population of the bright state, and the extent of electron-hole overlap. Through this comparison, we show that the measured room temperature radiative lifetimes can be understood in terms of exciton localization. Finally, the spatial sizes of the excitons are compared to those inferred by TA bleach saturation measurements.[20]

8.2 Results and Discussion

8.2.1 Standardization of QD 1S-1S bleach magnitudes

Due to spatial inhomogeneities in the pump and probe beams in a TA experiment, accurate determination of the absolute bleach magnitudes of NPLs following one photon excitation is experimentally nontrivial. It is facilitated by comparing the NPL TA spectrum with that of a standard, measured under identical experimental conditions. Specifically, the use of a standard allows the calculation of the fraction of NPLs that absorb a photon from the excitation pulse. Spherical CdSe QDs have known extinction coefficients and absorb at about the same wavelengths as the NPLs. As such, they provide a reliable and well-understood TA standard. To characterize the QD standard, the relative bleach magnitudes of a series of CdSe QD of different diameters were measured, and the static spectra and bleach magnitudes are presented in Figure 1. The concentrations were adjusted such that the absorbances at the excitation wavelength were the same. Furthermore, the spectrometer alignment and the excitation fluence were unchanged between measurements, ensuring that the total number of absorbed photons was held constant. The extinction coefficients at the excitation wavelength (ε_{387}) are determined from the absorption spectra using literature values for the extinction coefficients at the peak of the lowest exciton.[24]

The bleach is defined in terms of the absorbance change at the peak of the lowest exciton, $\Delta A/A_0 = (A_x - A_0)/A_0$, where A_0 and A_x are the absorbances before and several picoseconds after sample excitation. Taking the $\Delta A/A_0$ ratio also accounts for small differences in the extent of inhomogeneous broadening associated with changes in the size distributions from one sample to the next. Figure 8.1 shows that the $-\Delta A/A_0$ values increase with particle size, closely tracking the 387 nm extinction coefficients. The linear

dependence of $-\Delta A/A_0$ on extinction coefficient establishes that no additional significant concentration or other nonlinear effects are introduced upon changing the QD size and concentration.

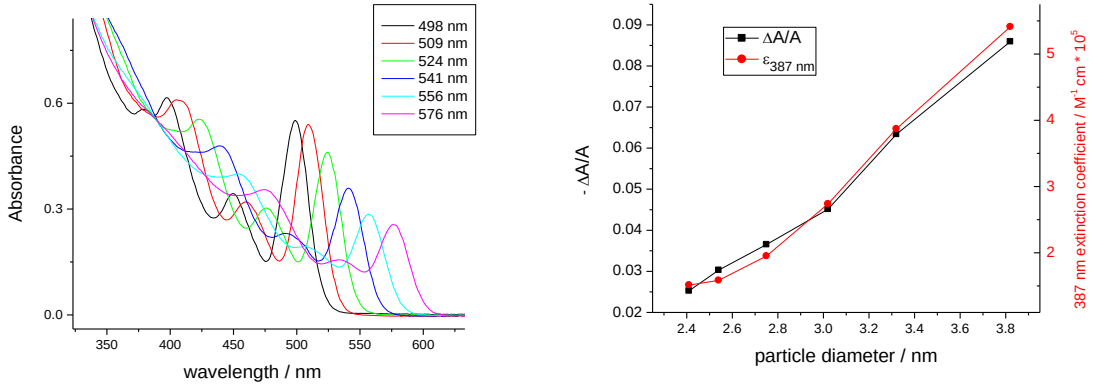

Figure 8.1. Static absorbance spectra of CdSe QDs (left) and a coplot of the relative bleach magnitudes and extinction coefficients at 387 nm as a function of particle diameter (right).

The magnitude of the bleach depends on the magnitudes of ground state absorption loss, stimulated emission, and excited state absorption. In general, the ground state absorbance is given by $A_0 = \varepsilon\, c\, l$, where ε is the extinction coefficient, c is the concentration and l is the pathlength. The absorbance following pulsed excitation includes contributions from excited state absorption and stimulated emission. This absorption is given by $A_x = [\varepsilon\,(1 - f) + f(\varepsilon_x - \varepsilon_{SE})]\, c\, l$, where ε_x is the excited state extinction coefficient, ε_{SE} is the excited state stimulated emission cross section, expressed as an extinction coefficient and f is the fraction of the population that absorbs a photon. It follows that $\Delta A = f\, c\, l\ (\varepsilon_x - \varepsilon - \varepsilon_{SE})$, and that

$$-\Delta A/A \;=\; f\,(\varepsilon_x - \varepsilon - \varepsilon_{SE})/\varepsilon \;=\; f\,(1- \varepsilon'/\varepsilon) \qquad \text{E8.2}$$

where ε' is the effective excited state extinction coefficient, $\varepsilon' = \varepsilon_x - \varepsilon_{SE}$. The presence of an electron in the conduction band reduces the lowest exciton excited state absorption by a factor of two, compared to the ground state,[25] so $\varepsilon_x = \varepsilon/2$. To the best of our knowledge, this assertion has not yet been experimentally corroborated, however, any uncertainty in ε_x will affect all of the NPL analysis in exactly the same way. The value of ε_{SE} can be derived from the consideration that the emission lifetime is about a factor of 20 longer than the radiative lifetime calculated from the absorption spectrum.[26] This is because most of the excited state population is in dark states that do not contribute to either spontaneous or stimulated emission, the so-called dark exciton.[3] Taking this ratio to be the ratio between absorption and stimulated emission cross sections, we get that $\varepsilon_{SE} = \varepsilon/20$. This value has a weak size dependence,[26] but we note that stimulated emission is a small contribution to the overall absorbance change and its size dependence can

reasonably be ignored. For the QD standard in the low power regime, we get that (1-ε'/ε) = 0.55.

Although the fraction of particles that absorb a photon is difficult to calculate from the spectrometer characteristics, in the low power regime, the fraction of particles (QDs or NPLs) that absorb a photon is proportional to the 387 nm extinction coefficient. The proportionality constant determined by the characteristics of the experiment (excitation pulse intensity, focal volume, etc.), and the same value can be used for both QDs and NPLs. Taking (1- ε'/ε) = 0.55 for QDs, equation 8.2 is evaluated for both NPL and QD then the ratio is taken to factor out the proportionality constant. It follows that the fraction of NPLs (*f)* that absorb a photon is given by E8.3, and the values of *f* are then substituted into E8.4 to calculate the excited state extinction coefficient ε'.

$$f = 1.82\left(\frac{\Delta A}{A_0}\right)_{QD}\left(\frac{\varepsilon_{NPL387}}{\varepsilon_{QD387}}\right) \qquad \text{E8.3}$$

$$\left(\frac{\Delta A}{A_0}\right)_{NPL} = 1.82\left(\frac{\Delta A}{A_0}\right)_{QD}\left(\frac{\varepsilon_{NPL387}}{\varepsilon_{QD387}}\right)\left(1-\varepsilon'/\varepsilon\right)_{NPL} \qquad \text{E8.4}$$

Finally, the platelet bleach magnitudes are multiplied by a factor of 1.1 before evaluating E8.4 to account the relative polarizations of the pump and probe beams used in the TA experiment. A detailed derivation of the polarization correction can be found in Appendix B.

8.2.2 Relative bleach magnitudes of CdSe NPL

Static and transient absorption spectra of several NPL samples of varying lateral dimensions were measured along with a QD standard, keeping the excitation conditions unchanged between measurements as described above. Examples of these spectra are shown in Figure 8.2.

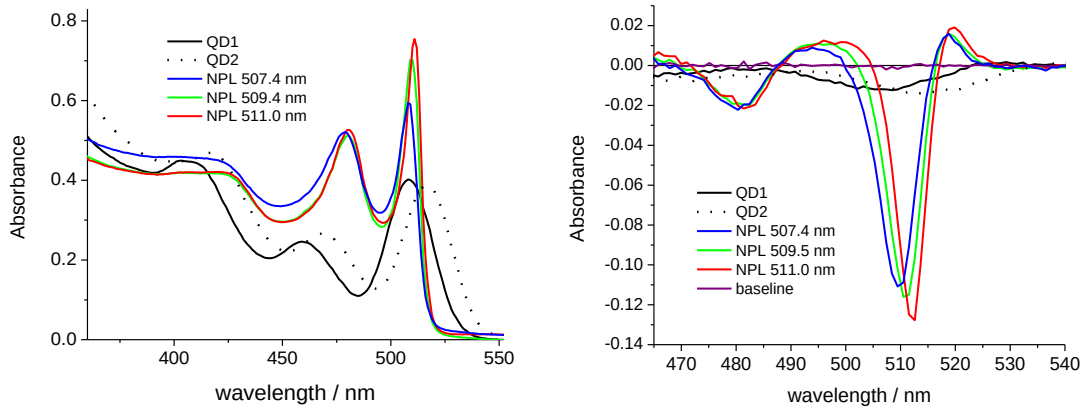

Figure 8.2. Static absorbance (left) and TA spectra (right) of a series of platelets of different lateral dimensions and two different QD standards. The 509.5 and 511 nm NPLs are matched with the QD1 standard and the 507.4 nm NPLs are matched with the QD2 standard.

This experiment was repeated with different sizes of NPLs having areas between 85.5 and 327 nm^2 along with absorbance-matched QD samples, with the results collected in Table 8.1. The smaller NPLs have a significant amount of inhomogeneous broadening in their static absorption and TA spectra, which is likely due to the greater quantum confinement along the in-plane dimensions. This leads to a larger spread of band gap energies compared to a sample of larger platelets with the same size distribution. In this case, the HH bleach band overlaps the positive TA feature at approximately 495 nm, making quantitative interpretation of the bleach magnitudes problematic. We therefore restrict our analysis to platelets with areas greater than 85 nm^2.

With the very large QD and especially NPL extinction coefficients, there is necessarily concern about saturation affecting the measured $\Delta A/A_0$ ratio. Meaningful comparison of QD and NPL values of $\Delta A/A_0$ requires that neither be saturated. Figure 8.1 shows that there is no evidence of saturation effects in the QD TA results at the pulse intensities used herein. However, NPL extinction coefficients are one to two orders of magnitude larger, and this issue need to be carefully considered. The question of linearity is addressed in three ways. First, we examine changes in NPL TA spectra with excitation power. Second, we measure the power dependence of $\Delta A/A_0$ ratio for NPLs versus QDs. Finally, we perform experiments where the excitation intensity for the NPLs, but not QDs, is attenuated by a known amount. These results are then compared to those in which the NPL excitation intensity is not attenuated.

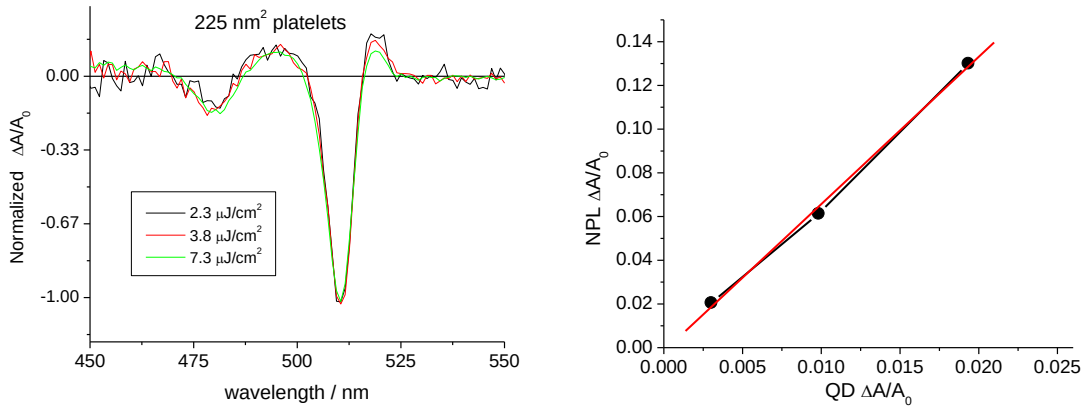

Figure 8.3. (left) Normalized transient absorption spectra as a function of excitation fluence. (right) Plots of NPL bleach magnitudes as a function of QD bleach magnitude. The slope of the linear fit is 6.7, which is much less than the ratio of 387 nm extinction coefficients (61.1).

The normalized TA spectra of the 7.7 x 29 nm NPLs taken at several different excitation intensities are shown in Figure 8.3. The normalized spectra are nearly identical except for the magnitude of the photoinduced absorption in the 520 nm region. The normalized spectra do show that the ratio of the 520 nm absorption to the 510 nm bleach decreases with excitation fluence, but the bleach is linear with excitation fluence, so the analysis is based entirely on the bleach amplitudes. We suspect that the decrease in the 520 nm absorption with increasing power is characteristic of the size of biexcitons relative to the single exciton, and this idea will be explored further in a later paper.

We have also obtained results with the NPL excitation intensity attenuated by a factor between 5 and ~10 compared to the QDs. We find that if the NPL $\Delta A/A_0$ values are multiplied by this factor and compared to those of the QD bleach, the results are consistent with measurements where the same power is used for both the QDs and NPLs. Three such runs are shown in Figure 8.4, which shows results from trials using a solution of quenched CdS QDs as an excitation filter as well as one trial using a longpass filter to attenuate the excitation. The bleach magnitudes are highly reproducible, showing that the ratio of NPL bleach magnitudes are within 3% of the ratio of pump fluences with and without the excitation filter in place. From the beam characteristics and NPL extinction coefficients, it is possible to make a rough estimate of the number of photons absorbed by the NPL at each power. It is important to note that under the highest powers, the NPLs are calculated to absorb a few (typically 1 – 3) photons upon excitation. The conclusion that follows from this result is fairly remarkable; even if the excitation intensity is such that some of the NPLs absorb more than a single photon, the magnitude of the lowest exciton bleach is linear with the number of photons absorbed. This indicates that the lowest exciton level can absorb at least a few photons into states that bleach the transition in the same way.

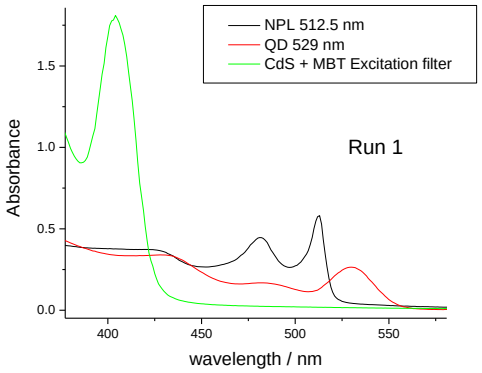
NPL 512.5 nm
QD 529 nm
CdS + MBT Excitation filter
Run 1
Absorbance
wavelength / nm

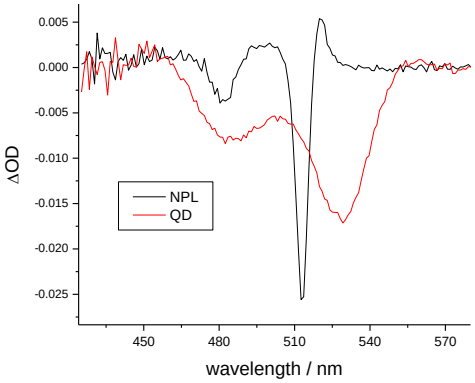
NPL
QD
ΔOD
wavelength / nm

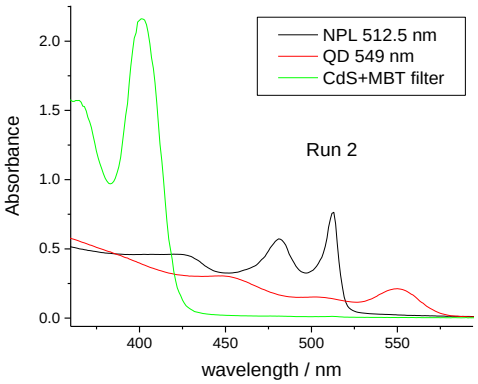
NPL 512.5 nm
QD 549 nm
CdS+MBT filter
Run 2
Absorbance
wavelength / nm

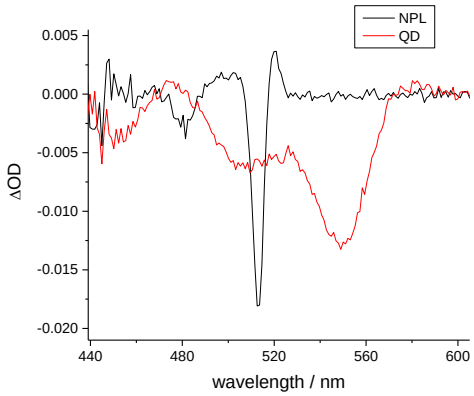
NPL
QD
ΔOD
wavelength / nm

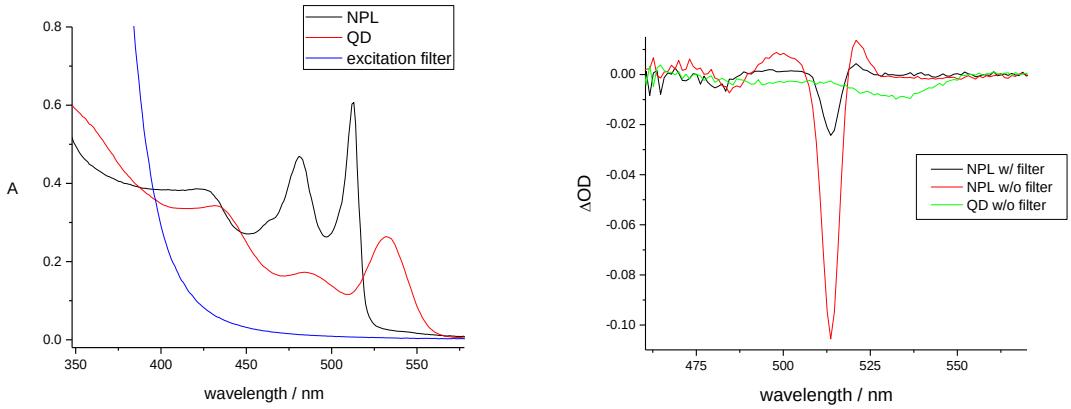

Figure 8.4. Top left: Static absorbance spectra of the 327 nm^2 platelets, QD standard, and excitation filter from Run 1 of Table 1. Top right: TA spectrum of the platelets using the CdS/MBT filter to attenuate the excitation beam coplotted with the QD standard using just hexane as the filter. Middle: Experiment was repeated using a different QD standard, excitation filter, concentrations, and spectrometer alignment, labeled Run 2 of Table 1. Bottom: Experiment was repeated using a longpass filter to attenuate the excitation instead of the CdS solution.

As an example, the analysis of the bleach magnitudes of the third run shown in Figure 8.4 is as follows: The absorbance of the filter at 387 nm is 0.67, indicating that 78% of the excitation is absorbed. The nanoplatelet bleach magnitudes at the peak of the HH bleach band with and without the excitation filter are 0.024 and 0.103, constituting a 77% decrease in the bleach magnitude. We therefore conclude that the spectrometer alignment is retained over the ~ 1 hour timescale of the experiment and that the NPL bleach magnitudes scale linearly with excitation power in this power regime.

Table 1 shows that the NPL ratio of the ground and excited state extinction coefficients at the bleach maximum (ε'/ε) ratio is much greater than ½, which is what one would expect based on simple state filling and stimulated emission considerations that apply to QDs (see equation 8.4). Absorption of a photon bleaches anywhere from about 4 to 20% of the HH absorption band, and the relative bleach magnitude decreases with increasing lateral area. The qualitative interpretation of this observation is that the exciton is localized in a small region of the NPL and therefore bleaches only a fraction of the absorption.

8.2.3 Excitonic areas derived from a model of the nanoplatelet excited state absorption

The partial bleaching of the NPL absorption can be more quantitatively interpreted through a simple model of the NPL spectroscopy. In this model, we make the following assumptions and approximations. First, the spatial extents of the quasi-two-dimensional electron and hole wavefunctions are characterized only by their areas, i.e., the details of the spatial dependence of both electron and hole wavefunctions are ignored. Second, the

spectral shifts of the photoinduced absorption bands are ignored. Finally, population of the p-states is ignored. We previously showed that incorporation of the spectral shifts and lateral state populations is necessary to accurately fit the TA spectra.[19] Although these approximations are obviously not quantitatively correct, it can be considered to be a limiting case model and provides a conceptual framework to understand the spatial extents of the electron and hole and ε'/ε ratio.

In the limiting case of a NPL having no lateral quantum confinement, the electron in-plane motion is in the potential of the hole and vice-versa. However, the electron effective mass is much less than that of the hole, so the spatial extent of the electron will be greater than that of the hole. The photoexcited region of the NPL can therefore be further divided into regions containing the electron or the electron and the hole. We denote the extent of the hole as having area V_h and the extent of the region having the electron only as having area V_e. It follows that the total area of the electron (alone and with the hole) is $V_x = V_e + V_h$. The total nanoplatelet area is denoted as V_{NPL}. The extent of absorbance change and stimulated emission in each of these regions is depicted in Figure 8.5.

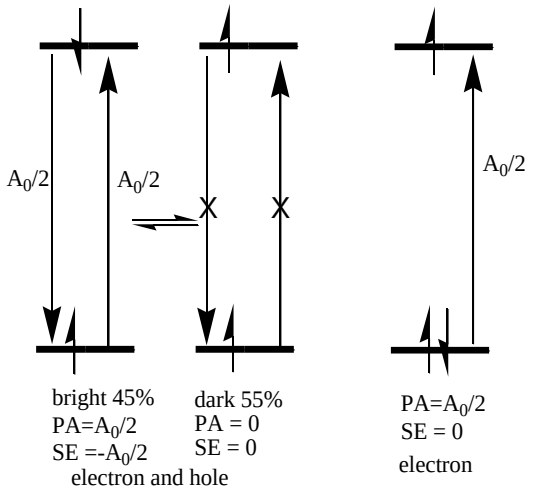

Figure 8.5. Model of the relative intensities of absorption and stimulated emission from regions of the NPL occupied by the electron or both the electron and the hole.

From this model it follows that the electron-hole overlap integral is given by

$$S = (V_h/V_x)^{1/2} \qquad \text{E8.5}$$

And the bleach magnitude is given by

$$-\Delta A/A_0 = f\, f_x(1 - \tfrac{1}{2}(V_e/V_x)) \qquad \text{E8.6}$$

where f is the fraction of the NPLs that absorb a photon (see equation 8.3), and f_x is the fraction of the NPL occupied by the exciton, $f_x = V_x/V_{NPL}$.

Evaluation of f_x and S requires determination of the V_e/V_x and V_h/V_x ratios. This is facilitated by comparing the bleach magnitudes with and without MBT. Specifically, trapping the hole decreases the magnitude of the bleach, and the extent of this decrease is related to the relative spatial extents of the electron and hole. Upon trapping the hole, $V_h = 0$, $V_e/V_x = 1$ and $-\Delta A(MBT)/A_0 = f f_x/2$. We previously reported that hole trapping reduces the magnitude of the bleach, i.e., $\Delta A(MBT)/A_0 = R_{MBT}\, \Delta A/A_0$, where R_{MBT} is the bleach ratio for the NPLs with and without MBT.[19] Specifically, for 4.5 monolayer 7.7 x 29 nm NPLs, we reported that $R_{MBT} = 0.73$. For the NPLs used in this study, we find that the bleach ratios vary within about 10% from one sample to the next with no obvious dependence on NPL size. The values of f and f_x are independent of the adsorbed MBT, so from equations 5 and 6, it follows that $0.50 = R_{MBT}\,(1 - \tfrac{1}{2}(V_e/V_x))$, or that $-\Delta A/A_0 = 0.685\, f\, f_x$ and $S^2 = 1/R_{MBT} - 1$. The observed value of $R_{MBT} = 0.73$ gives $S^2 = 0.37$.

The values of f are evaluated from equation 8.3, and comparing equation 8.4 with equation 8.6 gives the fraction of the NPL area occupied by the exciton, f_x.

$$f_x = \left(1 - \varepsilon'/\varepsilon\right) \Big/ \left(1 - V_e/2V_x\right) = \left(\left(\frac{\Delta A}{A_0}\right)_{NPL} \Big/ \left(\frac{\Delta A}{A_0}\right)_{QD} \right) \left(\frac{\varepsilon_{QD387}}{\varepsilon_{NPL387}}\right) \left(0.55 \Big/ \left(1 - \frac{V_e}{2V_x}\right)\right) \qquad \text{E8.7}$$

These values and the corresponding exciton areas are collected in Table 8.1 and Figure 8.6. The resulting f_x values depend on the measured bleach ratios with and without MBT, which exhibit some sample to sample variability. Multiple measurements give hole trap absorbance ratios in the range of 0.70 to 0.80. Putting the limiting values of V_e/V_x into equation 7, we conclude that this uncertainty introduces an error in the calculated values of f_x of less than about 10%.

Figure 8.6 shows that the exciton sizes vary between 18 – 24 nm^2, corresponding to an average Bohr radius of 2.7 nm, and are independent of NPL area. This is considerably less than the 3-dimensional bulk CdSe Bohr radius of 5.6 nm. The difference can be qualitatively understood in terms of the CdSe and surrounding material dielectric constants. The high frequency dielectric constant of CdSe is about 8.2,[27] while the surrounding hydrocarbon environment has a much lower value of about 2.0. Because the Bohr radius increases linearly with dielectric constant, an effective dielectric constant of 2.0 would result in a Bohr radius of 1.36 nm. To the extent that the exciton feels both the interior and exterior dielectric constants, the Bohr radius is expected to be between these values, and these measurements indicate that this is the case.

Table 8.1. Spectroscopic parameters and TA spectral intensities for a series of NPL and QD standards of varying physical dimensions

sample	dimensions/ nm	area / nm^2	ε_{387} / 10^5 M^{-1} cm^{-1}	$\Delta A/A_0$	f_x area fraction	exciton area / nm^2	τ_{rad} / ns calc	τ_{rad} / ns exp
QD 508.2	D = 2.53		1.70	0.0303				
NPL 509.5	7.7 x 29	225	104	0.1797	0.0778	17.5	5.9	5.6
NPL 509.5	7.7 x 29	225	104	0.216	0.0935	21.0	4.9	5.6
NPL 511.0	8.9 x 32	288	133	0.1838	0.0622	17.9	5.8	6.6
QD 518.5	D = 2.67		1.94	0.0243				
NPL 507.4	5.8 x 15.5	89.5	41.3	0.1640	0.254	22.8	4.5	5.8
QD 516.5	D = 2.64		1.93	0.0354				
NPL 508.4	6.2 x 13.9	85.5	39.4	0.2035	0.227	19.4	5.3	7.4
QD 531	D = 2.85		2.20	0.0625				
NPL 512	35.3 x 9.3	330	152	0.392	0.0777	23.8	4.25	5.4
QD 549	D = 3.17		3.16	.0631				
NPL 512	35.3 x 9.3	330	152	0.0255 x 10.9	0.074	24.0	4.26	5.4
QD 549	D = 3.17		3.16	0.0616				
NPL 512	35.3 x 9.3	330	152	0.0239 x 10.9	0.071	23.1	4.43	5.4

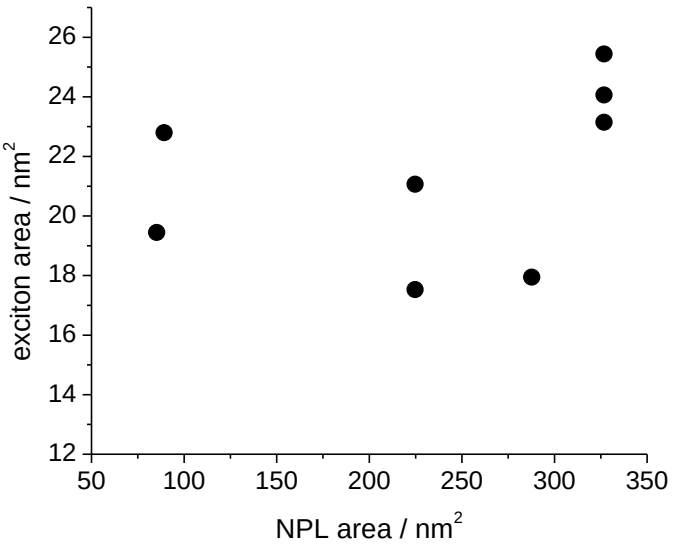

Figure 8.6. Exciton areas as a function of NPL area. The data are taken from Table 1.

8.2.4 Comparison of calculated and experimental radiative rates

The f_x values give the fraction of the NPL occupied by the exciton, and this is also the fraction of the total lowest exciton extinction coefficient appropriate to use in the radiative lifetime calculation, equation E8.1. Two other considerations also enter into the radiative lifetime calculation. First, the 5 meV splitting between the lowest dark state and the higher lying allowed state gives a 45% room temperature Boltzmann probability of being in the allowed state. Second, the square of the electron-hole overlap integral is calculated to be 0.37, and this factor also needs to be included into the rate calculation. Including these factors, E8.1 can be approximated as

$$1/\tau_{rad} = \left(0.45 f_x S^2\right) 2.88x10^{-9} n^2 \tilde{\nu}^2 1.064 \varepsilon_{\max} \Delta\tilde{\nu} \qquad \text{E8.8}$$

where ε_{max} is the extinction coefficient at the heavy hole exciton, $\Delta\tilde{\nu}$ is the full width half maximum of the peak, and the factor of 1.064 relates the integral of an assumed Gaussian peak to its full width at half maximum. Values of the radiative lifetimes calculated from E8.8 are also given in Table 8.1. Uncertainties in the value of the overlap integral squared, E8.5, are on the order of 30%, and the same uncertainties will be present in the calculated radiative lifetimes.

The PL spectra, decay kinetics and quantum yields (QYs) of several different sizes of NPLs are shown in Figure 8.7. These PL decays and QY values are very similar to those previously reported for similar sizes of 4.5 monolayer NPLs.[28]

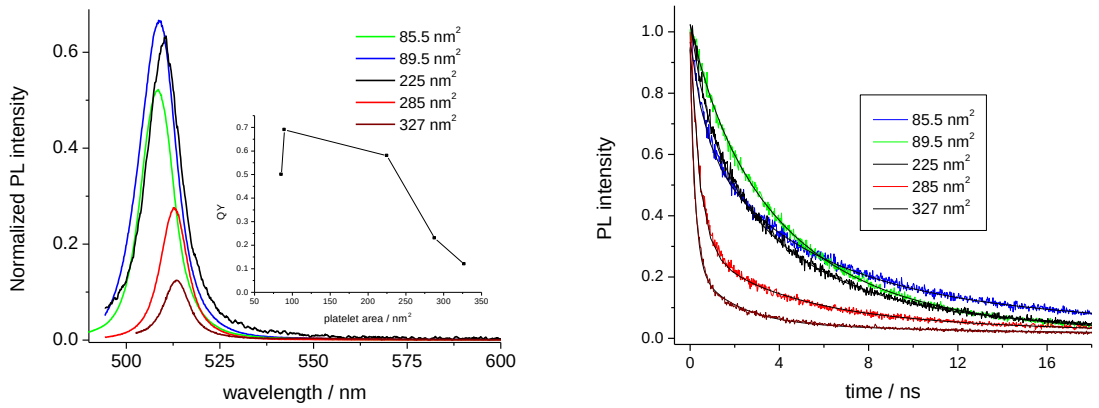

Figure 8.7. (left) PL spectra normalized to the relative quantum yield of several different sizes of NPLs. The inset shows the PLQYs. (right) Normalized decay kinetics and their fits to a triexponential corresponding to the PL spectra shown in the left panel.

In all cases, the PL kinetics can be fit to three decay components: a fast component (τ_1 < 1 ns), a slower component (τ_2 = 2 – 5 ns) and a small, much slower component (τ_3 > 20 ns). Specifically,

$$I(t) = A_1 \exp(-t/\tau_1) + A_2 \exp(-t/\tau_2) + A_3 \exp(-t/\tau_3) \qquad \text{E8.9}$$

The relative amplitudes of these components depend on the size of the NPL. We find that the PL QY values generally decrease while the amplitudes of the fastest component increase with increasing NPL area, consistent with what has been previously reported.[28] This is expected since the likelihood of any given platelet containing a defect site increases proportionally to the area. However, if the excitons localize to a small site and do not explore the entire area of the platelet, then this explanation does not hold. The explanation for this trend is therefore still lacking. Fits to the experimental PL decays are shown in figure 8.7 and the fitting parameters are given in Table 2.

Table 8.2. Fitting parameters, measured PLQYs, and the extracted radiative lifetimes for a series of NPL with varying lateral dimensions.

Sample	A_1	τ_1	A_2	τ_2	A_3	τ_3	QY	τ_{rad}
85.5 nm^2	0.34	800 ps	0.50	5.7 ns	0.10	31.4 ns	0.50	7.4 ns
89.5 nm^2	0.35	770 ps	0.50	5.7 ns	0.15	30.9 ns	0.69	5.8 ns
225 nm^2	0.30	820 ps	0.62	4.3 ns	0.08	23.7 ns	0.58	5.6 ns
288 nm^2	0.68	410 ps	0.26	3.9 ns	0.06	29.4 ns	0.23	6.6 ns
327 nm^2	0.75	220 ps	0.20	1.9 ns	0.05	20.3 ns	0.12	5.4 ns

The complicated kinetics and less then unity PL QYs indicate the presence of sample inhomogeneity and nonradiative processes. In the analysis of these decays, we assume that at room temperature, equilibration among the excited state angular momentum levels

is fast compared to the decay processes. This is known to be the case for QDs, and is surely a good approximation for NPL as well.[26, 29] The simplest (and incorrect) assignment is that the longest decay time corresponds to the radiative lifetime and the shorter components are due to subensembles having different rates of nonradiative processes. However, the amplitude of the slowest component is very small and the vast majority of the PL decays on a much faster timescale. Thus, such an assignment would predict a very small overall PL QY (less than 10%), which is inconsistent with the much larger observed PL QYs. We conclude that the only assignment of the long component that is consistent with the high overall QYs is that it is a "delayed fluorescence"; fluorescence that is obtained when the emitting state is in a rapid equilibrium with a slightly lower energy optically dark state. Such emission is well documented in many types of organic dyes[30] (particularly those used in organic light-emitting diodes[31]) and has been previously observed in CdTe QDs.[26] With this assignment, the radiative lifetime τ_{rad} ($= 1/k_{rad}$) can be extracted from the observed rates (k_1, k_2 and k_3, which are the reciprocals of the decay times, τ_1, τ_2 and τ_3 in table 2), amplitudes (A_1, A_2 and A_3) and overall PL QY through the simple, idealized mechanism depicted below in Figure 8.8.

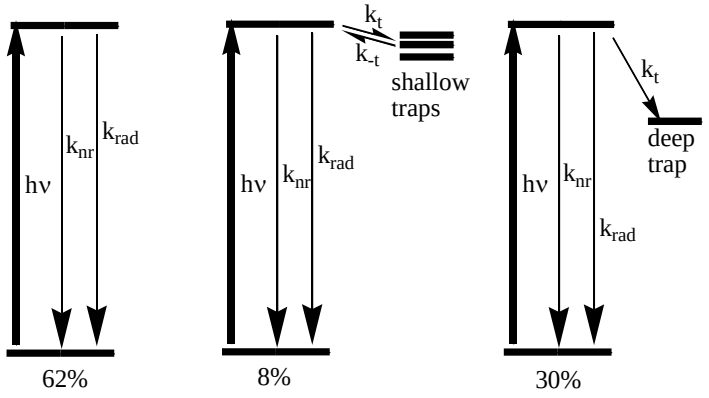

Figure 8.8. Dynamics of each subensemble in the NPL sample. The percentages indicate the relative abundances of each sub-ensemble in the 7.7 x 29 nm (225 nm^2) NPLs. The PL QY for these NPLs is 0.58 and the mechanism gives a calculated radiative lifetime of 5.5 ns.

In this mechanism, the NPLs consist primarily of two subensembles, those having deep traps and those which do not undergo any trapping on a timescale faster than the radiative rate. For the purpose of this analysis, it doesn't matter whether the trapping involves electrons or holes. The deep traps are more than a few k_BT deep, and this trapping is essentially irreversible. The fast decay rate associated with deep trapping is the sum of rates depleting the exciton state, $k_t + k_{rad} + k_{nr}$, where k_{nr} and k_t are the nonradiative and trapping rates in Figure 8.8, respectively. A deep-trapped carrier will eventually undergo nonradiative recombination on a timescale much longer than that of radiation. There is also a small sub-ensemble having shallow traps. Trapping into shallow traps establishes a thermal equilibrium between the trapped carrier and band edge

states. Once the equilibrium is established, only the equilibrium fraction in the band edge state can luminesce, giving rise to the long-lived delayed emission component. Prior to establishing this equilibrium, these NPLs also contribute to the fast decay component. This mechanism therefore assigns the fast decay primarily to the NPLs having deep traps and the mid-timescale component (the 67% component in Scheme 2) to the NPLs lacking these traps. Some of the fast component and the slow decay is assigned to NPLs having shallow traps.

The fitting parameters used in E8.9 along with the overall PL QY can be used to establish the values of the rates in the above scheme. Of particular interest are the values of the nonradiative rate, k_{nr} and especially the radiative rate, k_{rad}. These rates are taken to be the same for all of the particles, independent of the trapping rates. The NPLs having deep traps exhibit a fast decay, having a rate $k_1 = k_t + k_{rad} + k_{nr}$. The fraction of NPLs having shallow traps exhibits more complicated PL kinetics. The initial decay rate is taken to be the sum of all the rates, $k_t + k_{-t} + k_{rad} + k_{nr}$, which is experimentally indistinguishable from the deep trapping rate. Of the NPLS having shallow traps, the equilibrium population in the band edge state is given by $K_{eq} = k_{-t}/k_t$, and this population exhibits luminescence that decays with a rate of K_{eq} ($k_{rad} + k_{nr}$). It is important to note that in the case where the shallow traps exhibit minimal nonradiative decay, the presence of these shallow traps does not affect the overall QY. The parts of the ensemble lacking deep traps exhibit a quantum yield that is determined only by the radiative and nonradiative rates, $k_{rad}/(k_{nr} + k_r)$. The relative magnitude of the slowest component is given by $A_3/(A_2 + A_3) = k_t/(k_t + k_{nr} + k_{rad})$. We note that the magnitude of this component is somewhat uncertain because it is always small and any impurity QDs will also give PL on this timescale. We therefore do not attempt to assess the contribution of shallow trap NPLs to the fast component. With this model and these approximations, the radiative, nonradiative and trapping rates can be related to the experimental rates in E8.9. In this model, to a good approximation, $k_1 = k_t + k_r + k_{nr}$, $k_2 = k_{rad} + k_{nr}$ and $k_3 = K_{eq}$ ($k_{rad} + k_{nr}$). The overall QY is given in terms of these parameters and the radiative rate, $QY = A_1/(A_1 + A_2 + A_3)\ k_{rad}/k_1 + (A_2 + A_3)/(A_1 + A_2 + A_3)\ k_{rad}/k_2$. When normalized such that $A_1 + A_2 + A_3 = 1.0$, this is solved to give the radiative lifetime in terms of the measured decay curves and overall quantum yield, $\tau_{rad} = (A_1\ \tau_1 + (A_2 + A_3)\ \tau_2)/QY$. This assumes that all of the shallow-trapped population decays through the band edge state, so the long decay time does not enter into the calculation of τ_{rad}. Values of the radiative lifetime determined this way are essentially measured values. These radiative lifetimes along with those calculated from equation 8.8 are given in Table 1 and plotted versus NPL size in Figure 8.9. The trapping rate is very fast (< 1.2 ns), and the QY ($= k_{rad}/(k_t + k_{rad} + k_{nr})$) for the fraction of the NPLs having deep traps is quite low. As the size of the NPL increases, the fraction of particles having such a trap also increases, see table 8.2. Figure 8.9 shows that although there is some scatter and uncertainties in the results, reasonably good agreement between the measured and calculated values is obtained. It also shows little or no systematic variation of the radiative lifetime with NPL size throughout the size range studied here.

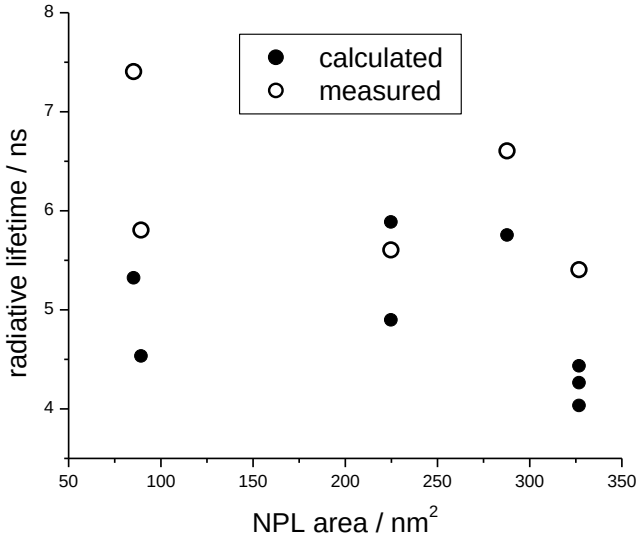

Figure 8.9. Calculated (from equation E8.8) and measured (from Table 8.1) values of the NPL radiative lifetime as a function of NPL area.

The agreement with the calculated values in Figure 8.9 rationalizes the experimental result seen here and in reference 28 that although the extinction coefficient varies with NPL size, the radiative lifetime does not. Figure 8.6 shows that the size of the exciton is much less than, and independent of the size of the NPL. The constant exciton size means that, at room temperature, the emission oscillator strength is also essentially NPL size-independent. Figure 8.9 shows that the measured radiative lifetimes are generally 10 – 20% longer than the calculated values. Although we do not have a definitive explanation for this difference, we speculate that it is due to thermal population of slightly higher energy excited lateral states. Specifically, we speculate that some equilibrium fraction of the electron and especially the hole occupy excited lateral states. When the electron and hole are in different lateral states their wavefunctions are orthogonal and such electron-hole states are dark. Having some fraction of the exciton population in these dark states may explain the small discrepancy between the calculated and measured values in 8.9.

It is also of interest to compare these results to the bleach saturation results recently reported in references 13 and 20. These studies compare the magnitude of the NPL bleach a few picoseconds and 1 ns following multiphoton excitation. The excitation power is sufficiently high that it initially saturates the bleach. The central idea behind this comparison is that following Auger recombination (which is complete within 1 ns) there remains exactly one exciton. The magnitude of this bleach can be corrected for any decay that occurs in the 1 ns interval. Thus, the corrected long versus short time bleach ratio is taken to be the number of lowest energy excitons that can fit in the NPL. This ratio is evaluated in reference 20, and by comparison to the geometric area of the NPL, an exciton area of about 96 nm^2 is obtained. This value is independent of the NPL size, with similar values obtained for NPLs varying in size from 90 to 250 nm^2. A similar analysis of the results presented in the Supporting Information of reference 13 gives a similar, but

somewhat smaller value of about 60 nm^2. Although the experimental method used to determine exciton sizes in reference 20 is completely different than the approach taken here, the results presented here also have the exciton areas being close to size-independent. However, the values reported in references 13 and 20 are significantly greater than the values reported in table 1. We speculate that the difference in the final results is due to consideration of hole trapping processes. Specifically, the analysis of reference 20 assumes that at long time the NPL has one remaining exciton, which in general will not be the case. A potential problem is that some of the excitons may undergo hole trapping prior to Auger recombination. In this case, there will be excess electrons in the NPL that contribute to the long-time bleach. The long-time bleach would therefore be greater than if there were a single exciton in the NPL, resulting in a smaller ratio of long:short time bleach magnitudes.

8.3 Conclusions

The relative bleach magnitudes of a series of 4.5 ML CdSe nanoplatelets are measured and compared to a quantum dot standard with a known excited state extinction coefficient. The ratio of NPL and QD bleach magnitudes are related to the fractional area occupied by a NPL exciton through a simple model that considers the absorption oscillator strength of individual regions of the platelet depending on their occupation by an electron, or both the electron and the hole. The model accounts for the differing spatial extents of the electron and hole and the resulting reduced e/h overlap integral, which are calculated from the bleach magnitudes before and after trapping a hole with MBT. It is found that the excitonic areas are independent of the platelet lateral dimensions over the range of sizes investigated here, and that the exciton sizes range between 18 – 24 nm^2. Localization of the exciton restricts the number of oscillators that can participate in emission, while absorption oscillator strengths scale with the NPL areas. Accounting for the reduced exciton size, together with the electron-hole overlap and Boltzmann population of the emissive HH fine structure level allows for nearly quantitative reproduction of the experimental radiative lifetimes. This resolves the apparent discrepancy between the quite large absorption extinction coefficients that scale linearly with area and the corresponding slow radiative lifetimes that are independent of platelet dimensions.

Ch 8 References

1. Yu, P. Y.; Cardona, M., *Fundamentals of Semiconductors*. third ed.; Springer: Berlin, 2001.
2. Norris, D. J., Electronic Structure in Semiconductor Nanocrystals: Optical Experiment. In *Nanocrystal Quantum Dots*, 2'd ed.; Klimov, V. I., Ed. CRC Press: 2010.
3. Efros, A. L.; Rosen, M.; Kuno, M.; Nirmal, M.; Norris, D. J.; Bawendi, M., Band-Edge Exciton in Quantum Dots of Semiconductors With a Degenerate Valence Band: Dark and Bright Exciton States. *Phys. Rev. B* **1996,** *54*, 4843 - 4856.
4. Ithurria, S.; Tessier, M. D.; Mahler, B.; Lobo, R. P. S. M.; Dubertret, B.; Efros, A. L., Colloidal Nanoplatelets With Two-Dimensional Electronic Structure. *Nat. Materials* **2011,** *10*, 936-941.
5. Scott, R.; Heckmann, J.; Prudnikau, A. V.; Antanovich, A.; Mikhailov, A.; Owschimikow, N.; Artemyev, M.; Climente, J. I.; Woggon, U.; Grosse, N. B.; Achtstein, A. W., Directed emission of CdSe nanoplatelets originating from strongly anisotropic 2D electronic structure. *Nature Nanotechnology* **2017,** *12*, 1155.
6. Ma, X.; Diroll, B. T.; Cho, W.; Fedin, I.; Schaller, R. D.; Talapin, D. V.; Wiederrecht, G. P., Anisotropic Photoluminescence from Isotropic Optical Transition Dipoles in Semiconductor Nanoplatelets. *Nano Lett.* **2018,** *18*, (8), 4647-4652.
7. Biadala, L.; Liu, F.; Tessier, M. D.; Yakovlev, D. R.; Dubertret, B.; Bayer, M., Recombination Dynamics of Band Edge Excitons in Quasi-Two-Dimensional CdSe Nanoplatelets. *Nano Lett.* **2014,** *14*, (3), 1134-1139.
8. Shornikova, E. V.; Biadala, L.; Yakovlev, D. R.; Sapega, V. F.; Kusrayev, Y. G.; Mitioglu, A. A.; Ballottin, M. V.; Christianen, P. C. M.; Belykh, V. V.; Kochiev, M. V.; Sibeldin, N. N.; Golovatenko, A. A.; Rodina, A. V.; Gippius, N. A.; Kuntzmann, A.; Jiang, Y.; Nasilowski, M.; Dubertret, B.; Bayer, M., Addressing the exciton fine structure in colloidal nanocrystals: the case of CdSe nanoplatelets. *Nanoscale* **2018,** *10*, (2), 646-656.
9. Achtstein, A. W.; Antanovich, A.; Prudnikau, A.; Scott, R.; Woggon, U.; Artemyev, M., Linear Absorption in CdSe Nanoplates: Thickness and Lateral Size Dependency of the Intrinsic Absorption. *J. Phys. Chem. C* **2015,** *119*, (34), 20156-20161.
10. Rajadell, F.; Climente, J. I.; Planelles, J., Excitons in Core-Only, Core-Shell and Core-Crown CdSe Nanoplatelets: Interplay Between In-Plane Electron-Hole Correlation, Spatial Confinement, and Dielectric Confinement. *Phys. Rev. B* **2017,** *96*, 35307-35316.
11. Strickler, S. J.; Berg, R. A., Relationship between Absorption Intensity and Fluorescence Lifetime of Molecules. *J. Chem. Phys.* **1962,** *37*, 814 - 822.
12. Kelley, A. M., *Condensed-Phase Molecular Spectroscopy and Photophysics*. Wiley: Hoboken, NJ, 2013.
13. Li, Q.; Liu, Q.; Schaller, R. D.; Lian, T., Reducing the Optical Gain Threshold in Two-Dimensional CdSe Nanoplatelets by the Giant Oscillator Strength Transition Effect. *J. Phys. Chem. Lett.* **2019,** *10*, (7), 1624-1632.

14. Griffin, G. B.; Ithurria, S.; Dolzhnikov, D. S.; Linkin, A.; Talapin, D. V.; Engel, G. S., Two-dimensional electronic spectroscopy of CdSe nanoparticles at very low pulse power. *J. Chem. Phys.* **2013,** *138*, (1), 014705.
15. Feldmann, J.; Peter, G.; Göbel, E. O.; Dawson, P.; Moore, K.; Foxon, C.; Elliott, R. J., Linewidth dependence of radiative exciton lifetimes in quantum wells. *Phys. Rev. Lett.* **1987,** *59*, (20), 2337-2340.
16. Kunneman, L. T.; Schins, J. M.; Pedetti, S.; Heuclin, H.; Grozema, F. C.; Houtepen, A. J.; Dubertret, B.; Siebbeles, L. D. A., Nature and Decay Pathways of Photoexcited States in CdSe and CdSe/CdS Nanoplatelets. *Nano Lett.* **2014,** *14*, (12), 7039-7045.
17. Diroll, B. T.; Cho, W.; Coropceanu, I.; Harvey, S. M.; Brumberg, A.; Holtgrewe, N.; Crooker, S. A.; Wasielewski, M. R.; Prakapenka, V. B.; Talapin, D. V.; Schaller, R. D., Semiconductor Nanoplatelet Excimers. *Nano Lett.* **2018,** *18*, (11), 6948-6953.
18. Achtstein, A. W.; Scott, R.; Kickhöfel, S.; Jagsch, S. T.; Christodoulou, S.; Bertrand, G. H. V.; Prudnikau, A. V.; Antanovich, A.; Artemyev, M.; Moreels, I.; Schliwa, A.; Woggon, U., p-State Luminescence in CdSe Nanoplatelets: Role of Lateral Confinement and a Longitudinal Optical Phonon Bottleneck. *Phys. Rev. Lett.* **2016,** *116*, (11), 116802.
19. Morgan, D. P.; Maddux, C. J. A.; Kelley, D. F., Transient Absorption Spectroscopy of CdSe Nanoplatelets. *J. Phys. Chem. C* **2018,** *122*, 23772-23779.
20. Li, Q.; Lian, T., Area- and Thickness-Dependent Biexciton Auger Recombination in Colloidal CdSe Nanoplatelets: Breaking the "Universal Volume Scaling Law". *Nano Lett.* **2017,** *17*, (5), 3152-3158.
21. Pu, C.; Zhou, J.; Lai, R.; Niu, Y.; Nan, W.; Peng, X., Highly Reactive, Flexible Yet Green Se Precursor for Metal Selenide Nanocrystals: Se-Octadecene Suspension (Se-SUS). *Nano Res.* **2013,** *6*, 652-670.
22. Yang, Y.; Li, J.; Lin, L.; Peng, X., An Efficient and Surface-Benign Purification Scheme for Colloidal Nanocrystals Based on Quantitative Assessment. *Nano Research* **2015,** *8*, 3353-3364.
23. Bertrand, G. H. V.; Polovitsyn, A.; Christodoulou, S.; Khana, A. H.; Moreels, I., Shape control of zincblende CdSe nanoplatelets. *Chem. Commun.* **2016,** *52*, 11975-11978.
24. Jasieniak, J.; Smith, L.; van Embden, J.; Mulvaney, P.; Califano, M., Re-examination of the Size-Dependent Absorption Properties of CdSe Quantum Dots. *J. Phys. Chem. C* **2009,** *113*, 19468 - 19474.
25. Klimov, V. I., Spectral and Dynamical Properties of Multiexcitons in Semiconductor Nanocrystals. *Annu. Rev. Phys. Chem.* **2007,** *58*, 635-73.
26. Gong, K.; Zeng, Y.; Kelley, D. F., Extinction Coefficients, Oscillator Strengths, and Radiative Lifetimes of CdSe, CdTe, and CdTe/CdSe Nanocrystals. *J. Phys. Chem. C* **2013,** *117*, 20268-20279.
27. Palik, E. D., *Handbook of Optical Constants of Solids*. Academic Press: 1998; Vol. II.
28. Olutas, M.; Guzelturk, B.; Kelestemur, Y.; Yeltik, A.; Delikanli, S.; Demir, H. V., Lateral Size-Dependent Spontaneous and Stimulated Emission Properties in Colloidal CdSe Nanoplatelets. *ACS Nano* **2015,** *9*, (5), 5041-5050.

29. Sercel, P. C.; Efros, A. L., Band-Edge Exciton in CdSe and Other II–VI and III–V Compound Semiconductor Nanocrystals − Revisited. *Nano Lett.* **2018,** *18*, (7), 4061-4068.
30. Grzywacz, J., Difference between Prompt and Delayed Fluorescence Spectra. *Nature* **1967,** *213*, 385-386.
31. Penfold, T. J.; Dias, F. B.; Monkman, A. P., The theory of thermally activated delayed fluorescence for organic light emitting diodes. *Chemical Comm.* **2018,** *54*, (32), 3926-3935.

Appendices

Appendix A: Solution to the exchange Hamiltonian for spherical particles with cubic symmetry

The effects of e-h exchange on the band edge exciton fine structure are calculated by diagonalizing the exchange Hamiltonian in E2.11 in the basis of the uncoupled electron and hole spin states. Since spin-orbit coupling splits off the J = 1/2 hole states, the band edge exciton is composed of states having a total hole angular momentum J = 3/2 with projections $m_J = \pm 3/2, \pm 1/2$, and a J = 1/2 electron with projections ± 1/2. The basis functions $|m_{Jh}, m_{Je}\rangle$ are listed according to the projection of the total hole angular momentum J = L + S onto the z-axis together with the projection of the electron spin angular momentum, with α = 1/2 and β = -1/2. To simplify, coupling with the envelope function angular momentum (S-D mixing) will be ignored along with crystalline asymmetry. $\sigma \otimes J$ in E2.11 is calculated in matrix form by taking the direct product (or Kroenecker product) of the electron and hole Pauli spin matrices σ and J. The direct product is taken individually over the x, y, and z components given in E.A1 then summed, yielding the exchange Hamiltonian matrix H_{exch} in A2. Diagonalization of E.A2 then gives the set of eigenvectors and their corresponding eigenvalues shown in Table A1.

$$\sigma_x = \begin{bmatrix} 0 & 1 \\ 1 & 0 \end{bmatrix} \qquad \sigma_y = \begin{bmatrix} 0 & -i \\ i & o \end{bmatrix} \qquad \sigma_z = \begin{bmatrix} 1 & 0 \\ 0 & -1 \end{bmatrix}$$

$$J_x = \begin{bmatrix} 0 & 3^{1/2} & 0 & 0 \\ 3^{1/2} & 0 & 2 & 0 \\ 0 & 2 & 0 & 3^{1/2} \\ 0 & 0 & 3^{1/2} & 0 \end{bmatrix} \qquad J_y = i \begin{bmatrix} 0 & -3^{1/2} & 0 & 0 \\ 3^{1/2} & 0 & -2 & 0 \\ 0 & 2 & 0 & -3^{1/2} \\ 0 & 0 & 3^{1/2} & 0 \end{bmatrix}$$

$$J_z \begin{bmatrix} = \begin{matrix} 3 & 0 & 0 & 0 \\ 0 & 1 & 0 & 0 \\ 0 & 0 & -1 & 0 \\ 0 & 0 & 0 & -3 \end{matrix} \end{bmatrix}$$

$$\sigma \otimes J = \sigma_x J_x + \sigma_y J_y + \sigma_z J_z \qquad \text{E.A1}$$

$$H_{exch} = \sigma \otimes J = \begin{bmatrix} 3 & 0 & 0 & 0 & 0 & 0 & 0 & 0 \\ 0 & 1 & 0 & 0 & 2\sqrt{3} & 0 & 0 & 0 \\ 0 & 0 & -1 & 0 & 0 & 4 & 0 & 0 \\ 0 & 0 & 0 & -3 & 0 & 0 & 2\sqrt{3} & 0 \\ 0 & 2\sqrt{3} & 0 & 0 & -3 & 0 & 0 & 0 \\ 0 & 0 & 4 & 0 & 0 & -1 & 0 & 0 \\ 0 & 0 & 0 & 2\sqrt{3} & 0 & 0 & 1 & 0 \\ 0 & 0 & 0 & 0 & 0 & 0 & 0 & 3 \end{bmatrix} \qquad \text{E.A2}$$

Table A1. Eigenvectors and eigenvalues of the e-h exchange operator $\sigma.J$

Basis	Eigenvectors							
	v1	v2	v3	v4	v5	v6	v7	v8
|3/2, α >	0	0	0	0	0	0	0	1
|1/2, α >	0	0	$-1/\sqrt{3}$	0	0	0	$\sqrt{3}$	0
|-1/2, α >	0	-1	0	0	0	1	0	0
|-3/2, α >	$-\sqrt{3}$	0	0	0	$1/\sqrt{3}$	0	0	0
|3/2, β >	0	0	1	0	0	0	1	0
|1/2, β >	0	1	0	0	0	1	0	0
|-1/2, β >	1	0	0	0	1	0	0	0
|-3/2, β >	0	0	0	1	0	0	0	0
Eigenvalues	-5	-5	-5	3	3	3	3	3

The 8 states are split into two levels, with the lower level having g(E) = 3 and the higher level g(E) = 5. Note that the eigenvectors v4 and v8 form the $J_{tot} = \pm 2$ pure triplet level that is supposed to be stabilized with respect to the lower angular momentum states, but the eigenvalue puts them in the higher energy band. Care must be taken when considering values of spin or energy of quasiparticles like the exciton. The triplet state appears at higher energy because the actual coupling of spins is between electrons, not between an electron and hole. The triplet exciton should therefore be considered to have anti-aligned electron and hole spins, corresponding to a greater total electron angular momentum. Except for the J = 2 states, the resulting eigenvectors are admixtures of the various uncoupled spin states, and the composition of each state is the same as one reads off a table of Clebsch-Gordon coefficients. This is to be expected since the Clebsch-Gordon treatment is a change of basis between vector spaces $|m_{Jh}, m_{Je}\rangle$ in the coupled vs uncoupled angular momentum representations. It follows that the transformation matrix T has the same form as the exchange Hamiltonian derived in E.A2. The derivation from the Pauli spin matrices is more intuitive since it begins with a physical picture and an explicit form of the interaction potential, whereas deriving the Clebsch-Gordon coefficients is purely operator algebra.

Comparison of H_{exch} in E2.11 with the Heisenberg Hamiltonian suggests that QD e-h exchange follows a different distance dependence than does exchange between electrons in neighboring atomic orbitals. The latter is treated in most introductory quantum mechanics texts and leads to the well-known exponential decay of the exchange integral with increasing internuclear separation. This comes about from the normalization condition. If the interacting electrons orbitals aren't completely orthogonal, then nonzero off-diagonal terms appear in the calculation of the normalization constant, yielding the symmetric and anti-symmetric wavefunctions Ψ_+ and Ψ_-. The energies are calculated in E.A3, and singlet/triplet splitting Δ_{ST} in E.A4.

$$\Psi_+ = \frac{1}{\sqrt{2(1+S)}}(\varphi_a + \varphi_b)$$
$$\Psi_- = \frac{1}{\sqrt{2(1-S)}}(\varphi_a - \varphi_b) \qquad \text{E.A3}$$

$$E_{\pm} = \langle \Psi_{\pm} | H | \Psi_{\pm} \rangle = \frac{1}{2(1 \pm S)} (H_{aa} + H_{bb} \pm 2H_{ab})$$

$$\Delta_{ST} = \frac{S\,\varepsilon - H_{ab}}{1 - S^2} \qquad \text{E.A4}$$

The singlet/triplet splitting goes as $\frac{1}{1-S^2}$, where S is the overlap integral between the two single-electron wavefunctions. Atomic 1S orbitals decay exponentially from the nucleus, so we'll the take the form of the 1-electron wavefunctions as

$$\varphi_a = e^{-r/r0} \quad \text{and} \quad \varphi_b = e^{(r-R)/r0} \qquad \text{E.A5}$$

The overlap integral S then depends on the internuclear separation R according to

$$S = \langle \varphi_a | \varphi_b \rangle = \int e^{-r/r0} * e^{\frac{r-R}{r0}}\, dr = e^{-R/r0} \qquad \text{E.A6}$$

The splitting, and in turn the magnitude of the exchange interaction, fall off exponentially, so exchange is accordingly referred to as the short-range force.

Electron-hole exchange in delocalized excitonic states also arises from the interaction between Cd- and Se-localized spins at the unit cell level, but the interaction is typically parameterized by an empirical value of the exchange interaction. The distance dependence in treatments of exchange in nanomaterials is typically given as the dependence on the particle radius. In this case, the trend in radius is simple to understand; the 'amount' of electron or hole in any given unit cell decreases with the volume of the particle, while the sum over each over all unit cells remains 1 and is independent of volume. The interaction therefore decreases with the volume.

Appendix B: Derivation of polarization correction to TA spectral intensities

The experimental coordinate frame is defined such that the excitation propagates along the y axis and is polarized along the z axis. The probe also propagates along the y axis and is polarized in the x-z plane. Photoselection occurs because the probability of absorbing a probe photon depends on the orientation of the pump electric field relative to the NPL transition dipole moment. The NPL absorption at 387 nm and the lowest exciton are taken to be in-plane polarized. This is a reasonable approximation, although at 387 nm, there may be some out-of-plane component. This analysis below treats the QDs as spheres and ignores the differences in local field factors along the nanoplatelet axes, which should be minor approximations.

The distribution of out-of-plane vectors following photon absorption by a planar oscillator is proportional to $\sin^2\theta$, where θ is the angle of the unique axis with respect to laboratory fixed z axis. Inclusion of the volume element and normalization gives the distribution over θ as

$$P(\theta) = \frac{3}{8\pi}\sin^3(\theta) \qquad \text{E.B1}$$

The magnitude of the interaction with a probe photon polarized along x and z axes are defined as I_x and I_z, respectively. These intensities are calculated by taking the projection of the initial distributions of the in-plane oscillators along each respective axis, as done in E.S4 and E.S5. To calculate I_x, the integrated projections of the platelet x and y axis onto the laboratory frame x axis are summed. Because x and y are equivalent, the sum over all space is 2, reflecting the two degenerate oscillators. We note that this give the well-known result that the anisotropy is 0.1.

$$I_z = \int_0^{2\pi} d\varphi \int_0^{\pi} P(\theta)\sin^2\theta \; d\theta = 2\pi\frac{3}{8\pi}\int_0^{\pi}\sin^5\theta \, d\theta = 4/5 \qquad \text{E.B2}$$

$$I_x = \int_0^{2\pi}\int_0^{\pi} P(\theta)(\sin^2\varphi\cos^2\theta + \cos^2\varphi) \; d\varphi \, d\theta = 3/8\int_0^{\pi}\sin^3\theta \; d\theta + 3/8\int_0^{\pi}\sin^3\theta\cos^2\theta \, d\theta = 3/5 \qquad \text{E.B3}$$

Probe photons oriented at an angle θ between z and x interact with the distribution of platelet transition dipole moments according to E.S6

$$I(\theta) = N(I_z\cos^2\theta + I_x\sin^2\theta) \qquad \text{E.B4}$$

Restricting θ to the interval between 0 and π/2 and normalizing gives

$$I_{NPL}(\theta) = \frac{4}{7\pi}(4\cos^2\theta + 3\sin^2\theta) \qquad \text{E.B4}$$

QDs are isotropic absorbers, so I(θ) is independent of θ. Normalizing this distribution over the same interval gives

$$I_{QD}(\theta) = \frac{2}{\pi} \qquad \text{E.B5}$$

Setting the QD and NPL excited state absorbances equal gives $\theta = \pi/4$, and this is the angle at which the polarization effect vanishes. However, the experimental geometry uses nearly perpendicular pump and probe orientations, so the nanoplatelet TA spectral intensities are scaled by a factor of $I_{NPL}(\pi/2) / I_{NPL}(\pi/4) = (7/2) / 3 = 1.17$. We find that the bleach ratio at nearly perpendicular 45° polarization angles is 1.10. The difference between this value and the calculated value of 1.17 is attributed to the pump being not entirely orthogonal to the probe pulses and/or some out-of-plane NPL absorption component at the pump wavelength. No further correction due to rotational diffusion is needed because the diffusion times are long compared to the delay times used here.